LOW CARBON LIVING CRC

Project RP1020

Field Performance of Geopolymer Concrete Structures

Authors	Professor Stephen Foster, UNSW Sydney Professor Jay Sanjayan, Swinburne University of Technology A/Professor Arnaud Castel, UNSW Sydney Dr James Aldred, AECOM, and Adjunct Associate Professor, UNSW Sydney Dr Johnson X. Shen, Lecturer, UNSW Sydney Professor Marita L. Berndt, Swinburne University of Technology Dr Pathmanathan Rajeev, Senior Lecturer, Swinburne University of Technology Craig Heidrich, Ash Development Association of Australia, and Australasian (iron & steel) Slag Association Marc Smith, Australasian (iron & steel) Slag Association Dr Daksh Baweja, Ash Development Association of Australia Dr Mohammad Khan, Research associate UNSW Sydney Hammad Khan, Ph.D. Candidate, UNSW Sydney Jerry J. Dang, Master by Research Candidate, UNSW Sydney Kirubajiny Pasupathy, Ph.D. Candidate, Swinburne University of Technology
Title	Field Performance of Geopolymer Concrete Structures
ISBN	
Format	
Keywords	Geopolymer, alkali-activated, binder, concrete, field trails
Editor	
Publisher	CRC for Low Carbon Living
Series	
ISSN	
Preferred citation	

UNSW SYDNEY

SWINBURNE UNIVERSITY OF TECHNOLOGY

Australian Government
Department of Industry, Innovation and Science

Business Cooperative Research Centres Programme

Acknowledgements

This research work reported here was funded by the Cooperative Research Centre (CRC) for Low Carbon Living Ltd., supported by the Cooperative Research Centres, an Australian Government initiative. The support of the CRC is gratefully acknowledged.

This study was undertaken by The University of New South Wales, Sydney, Centre for Infrastructure Engineering and Swinburne University of Technology Centre for Sustainable Infrastructure, the Australasian (iron & steel) Slag Association and the Ash Development Association of Australia.

The assistance provided for the field studies by Wagners Pty Ltd, Zeobond Pty Ltd, Antonello Precast Concrete Pty Ltd, Rocla Pty Ltd, Sydney Water, Milliken Pty Ltd, Dr. Didar Cheema (Main Roads Western Australia) and Dr. David Law (RMIT University) are gratefully acknowledged.

Disclaimer

Any opinions expressed in this document are those of the authors. They do not purport to reflect the opinions or views of the CRCLCL or its partners, agents or employees.

The CRCLCL gives no warranty or assurance, and makes no representation as to the accuracy or reliability of any information or advice contained in this document, or that it is suitable for any intended use. The CRCLCL, its partners, agents and employees, disclaim any and all liability for any errors or omissions or in respect of anything or the consequences of anything done or omitted to be done in reliance upon the whole or any part of this document.

Executive Summary

A major barrier to the adoption of Geopolymer concrete in construction is the lack of long-term performance data. Field testing has been undertaken to determine the behaviour of geopolymers in different service environments and address the gaps in knowledge. The University of New South Wales (UNSW Sydney) and Swinburne University of Technology (SUT) undertook field testing at sites to examine durability aspects including carbonation, chloride ingress, reinforcement corrosion and acid attack. This report describes: (1) In-situ testing and core sampling of Geopolymer concrete at four sites across Australia; (2) Long-term performance monitoring of two Geopolymer concrete structures; and (3) In-situ test procedure to investigate the biogenic corrosion of mortar specimens.

The sites studied include and their exposure classifications were:

- Campbellfield, Perth and Toowoomba are located away from severe exposure. AS3600 exposure environment is 3(a) “Surfaces of members in above-ground exterior environments”. The Campbellfield and Perth sites are near costal and have exposure classification B1. Toowoomba is more than 50 km inland, temperate, non-industrial, and is exposure classification A2.
- Portland, Westport Boat Ramp Project at Port Macquarie NSW and Rocky Point boat ramp QLD are examples of structures in a marine environment exposed to chloride contamination. AS3600 exposure environment is 5c, in tidal/splash zone, and exposure classification is C2.
- Lake King is a severe environment combining chloride, acid and sulphate attacks. AS3600 exposure classification is U.
- North Head Wastewater Treatment Plant in Manly, NSW, is a severe environment involving biogenic corrosion of Geopolymer mortar Specimens. AS3600 exposure classification is U.

In regards to testing on the Wellcamp Business Park Bridge, the response of the bridge to mechanical loading as well as daily and seasonal temperature variations was investigated. Overall, the Geopolymer concrete slab performs well under the daily and seasonal temperature variations without any significant change in its structural integrity. The response of the bridge to truck loading in terms of deflection was correctly predicted by finite element modelling and is in agreement with serviceability requirements.

Concrete carbonation was the main potential deterioration for Campbellfield site, Perth site, Toowoomba tanks site located in AS3600 3(a) exposure classification. Overall results are showing that the performance of Geopolymer concrete is dependent on the mix design parameters. Campbellfield site results showed that two Geopolymer concretes of similar specifications (70-75% fly ash/25-30% GGBFS) but with different activator compositions performed quite differently. Toowoomba tanks site results showed that carbonation front penetration in high GGBFS based Geopolymer was faster than the reference OPC concrete. Therefore a prescriptive approach based on compressive strength and mix design parameters appears not to be appropriate to control the risk of carbonation induced steel reinforcement corrosion in Geopolymer concrete. Rather, performance based approaches are needed.

On marine exposure, the results obtained at Portland site were in contradiction with results obtained at Rocky Point. For both Portland and Rocky Point, GGBFS based Geopolymer concrete were used. The performance of the Geopolymer concrete at Portland site was moderate. The performance of the Geopolymer EFC concrete at Rocky Point boat ramp was outstanding with a low chloride diffusion coefficient being measured.

At Lake King site, fly ash based Geopolymer was used. The performance of the Geopolymer concrete was poor in terms of chloride penetration resistance. With regards to carbonation, the performance of Geopolymer concrete in a chloride environment is very variable, and is dependent on mix design parameters, including the activator used.

Both Lake King site and North Head Wastewater Treatment Plant investigation showed that fly ash based Geopolymer concrete does not perform well against in aggressive environments high in chlorides and/or sulphates. Whereas GGBFS based Geopolymer concrete seems to perform well, although longer term investigations are needed to draw any reliable conclusion. Experiments are still in progress at North Head Wastewater Treatment Plant.

Importantly, the Toowoomba tank site showed that geopolymers after cracking experience efficient self-healing similarly to OPC concrete. Self-healing capability of concrete is an important aspect of structure durability.

Overall, the field testing campaign confirms the necessity of developing performance based specifications for Geopolymer concretes. Suitable testing methods are required to assess the performance of concrete in order to assist engineers to specify Geopolymer concrete conservatively and in confidence, particularly in more aggressive environments.

Contents

Introduction

The concentration of greenhouse gases has been increasing for the past two decades. CO_2 is the major contributor, among all the gases, with a contribution of 55% towards global warming. Since ordinary Portland cement (OPC) clinker is manufactured by burning limestone (calcium carbonate) and siliceous materials resulting in a heavy production of CO_2, OPC concrete has a very high carbon footprint [1]. To minimize the emissions of CO_2, the researchers are focusing on using alternative concretes which have a lower carbon footprint and better performance in terms of strength and durability. Geopolymer concrete (GPC) is a synthetic material having a carbon footprint 80% lesser as compared to conventional OPC concrete. Geopolymer cement is synthesize with the application of alkaline solution such as sodium hydroxide (NaOH), potassium hydroxide (KOH), sodium silicate (Na_2SiO_3) and potassium silicate (K_2SiO_3) to activate aluminosilicate materials [2]. Aluminosilicate materials commonly include fly ash, metakaolin and ground granulated blast furnace slag (GGBFS).

The RP1020 project was sponsored by the CRC for Low Carbon Living addresses overcoming barriers to use of Geopolymer concrete in construction.

This report covers the progress to date on in-situ testing and long-term field monitoring of Geopolymer concrete in a wide variety of service environments throughout Australia.

In-Situ Testing and Core Sampling

Campbellfield, Victoria (SUT)

Introduction

Field testing of Geopolymer concrete was performed on two slabs at Campbellfield, Victoria. The site is 18 km north of the Melbourne CBD and the AS 3600 exposure classification is B1. The slabs were constructed by Zeobond in 2007. The main slab originally supported a batching plant and was built using concrete based on a 75% fly ash 25% slag blend activated with sodium hydroxide, potassium hydroxide and sodium silicate (Type 1 GPC). Adjacent to the main slab was an apron slab constructed with sodium hydroxide activated 70% fly ash 30% slag concrete (Type 2 GPC). Figure 1 shows the original slabs.

Figure 1. Main slab (M) and apron slab (A) at Campbellfield Site, VIC (source: www.zeobond.com).

The opportunity arose to test the slabs as the site was for being prepared for sale. The batching plant had been dismantled. Field testing and extraction of core samples were performed in March and April 2015. Figure 2 shows the main slab before testing.

The following in-situ field tests were performed on the slabs:

- Visual condition assessment
- Measurement of crack widths
- Depth of cover to reinforcement
- In conjunction with the in-situ tests, core samples were extracted from the slabs. The core samples were initially tested for the following:
- Visual appearance (i.e., uniformity, presence of voids, condition of any embedded reinforcement)
- Depth of carbonation by phenolphthalein testing

Figure 2. Main slab at Campbellfield site, VIC in March 2015.

Figure 3 shows the coring in progress and Figure 4 is a typical core sample.

The core samples were then subjected to laboratory testing for the properties listed below:

- pH profile
- Density
- Sorptivity
- Volume of permeable voids
- Microstructure and phase analysis using SEM, XRD, FTIR and TGA methods
- Total pore volume and pore size distribution analysis by liquid N2 adsorption method
- Elastic modulus
- Compressive strength

Figure 3. Extraction of cores from main slab at Campbellfield site, VIC in April 2015.

Figure 4. Typical core sample from main slab at Campbellfield site, VIC in April 2015.

Test results

Mechanical properties

Table 1 shows the compressive strength and elastic modulus including the Standard Deviation (SD) of both type of core specimens. The values were derived with average of three specimens from Type 1 GPC and two specimens from Type 2 concrete. The average compressive strength of Type 1 and Type 2 GPC core specimens were 44.2 MPa and 53.3 MPa and the elastic modulus values were 22.1 GPa and 25.3 GPa, respectively. For this mix of GPC the elastic modulus is lower than for similar strength OPC concrete, which also confirms by previous research results based on laboratory tests [3].

Table 1. Compressive strength and elastic modulus values.

Specimens No	Compressive strength (Mpa)	Modulus of Elasticity(GPa)
Type 1	44.2 (|2.1|)	22.1 (|1.7|)
Type 2	53.3 (|2.75|)	25.3 (|2.2|)

Carbonation resistance of field exposed GPC

Figure 5 displays the carbonation depth measurement for both types of concrete core specimens by using the phenolphthalein indicator. The carbonation depth values of Type 1 and Type 2 specimens after eight years of exposure in real field environment were 23.5-27.5 mm and 8-14 mm respectively. The carbonation depth values of Type 1 GPC were much higher than the ones obtained for Type 2 GPC specimens. This can be due to either the different Geopolymer concrete mix design or the location of the coring in the slabs. Indeed, since the core specimens were extracted from the vertical surface of the Type 1 GPC slab and the horizontal top surface of Type 2 concrete slab, the moisture content of the concrete could be different affecting the CO_2 diffusion.

To compare the performance of Geopolymer and OPC concrete in outdoor field conditions, experimental results obtained on two thirteen years old beams exposed to an outdoor environment in the South-West of France are considered [4] and the work of Ho and Lewis [5] in which concrete samples were exposed to outdoor conditions in Melbourne. The compressive strength of the OPC concrete in the French beams was 45MPa at 28 days and then around 56 MPa after 13 years (measured by coring the beams). Thus, the OPC concrete strength was similar to the one of the Type 2 Geopolymer concrete. The beams were subjected to sustained loading and cracked. Only results obtained in the concrete zones where the stress level in either compression or tension (far from the cracks) was low are considered here. The carbonation depth values measured were ranging from 7 to 13 mm. The concrete samples tested in outdoor conditions by Ho and Lewis [5] were cured for one day and had 20% fly ash and a 28 day compressive strength 46 MPa. The carbonation coefficients after one year were 4.5 mm/yr$^{0.5}$ for north oriented vertical exposure and 3.0 mm/yr$^{0.5}$ for south inclined exposure. The differences were due to lower rainfall on the vertical surfaces.

Considering that concrete carbonation depth is proportional to the square roots of time (i.e., $x = K \times \sqrt{year}$ year (in mm), where K = carbonation coefficient). Ta-

ble 2 shows the *K* values obtained for the OPC concrete and the two Geopolymer concretes.

Table 2. *K* values obtained for the OPC concrete and the two Geopolymer concretes (in mm/yr$^{0.5}$).

OPC Concrete	Geopolymer Type 1	Geopolymer Type 2
2.0 – 3.6	8.3 – 9.8	2.8 – 5.0

The results are indicative that the carbonation rate of Type 1 Geopolymer concrete in ambient environment is higher than the OPC concrete. Similar conclusions maybe drawn for similar strength with partial replacement of cement with fly ash and exposed to outdoor conditions (e.g. [5]). However, it appears that the performance of Type 2 Geopolymer concrete is similar to the performance of the OPC and 20% fly ash concrete for a similar compressive strength. This will be further discussed in the section on water absorption and apparent volume of permeable voids results.

In OPC concrete, CO_2 ingress into the concrete decreases with duration of exposed period in CO_2 environment due to the formation of dense $CaCO_3$ layer as a product of carbonation reaction. Here, the fly ash is the major constituent in both types of concrete and the primary carbonation reaction products will be sodium carbonate (Na_2CO_3) and potassium carbonate (K_2CO_3) [6], that are highly soluble and which can increase the porosity of the concrete surface. Although $CaCO_3$ is produced from carbonation of slag component [7], the amount of slag used in both types of concrete is low compared to fly ash content. Therefore, this could be the reason for the higher carbonation rate of Geopolymer concrete structures which induces the penetration of CO_2 into the concrete.

Furthermore, phenolphthalein indicator did not always provide a clear carbonation front and in some cases it shows a light pink colour after the application of the phenolphthalein solution (Figure 6), this was also reported by other researchers [8-10]. In alkali activated slag concrete, phenolphthalein provided clear identification of carbonation front due to the formation of calcium carbonate product from the carbonation of $Ca(OH)_2$ and C-S-H gels. However, in fly ash based Geopolymer concrete, formation of Na_2CO_3 do not provide the clear carbonation front with phenolphthalein indicator [8]. In this study, a fly ash and slag combination was used to make the Geopolymer binder. Therefore, the formation of both types of carbonation products (fly ash and slag reaction products) could be the reason for the clear carbonation front obtained in some cases and no visible carbonation front in others.

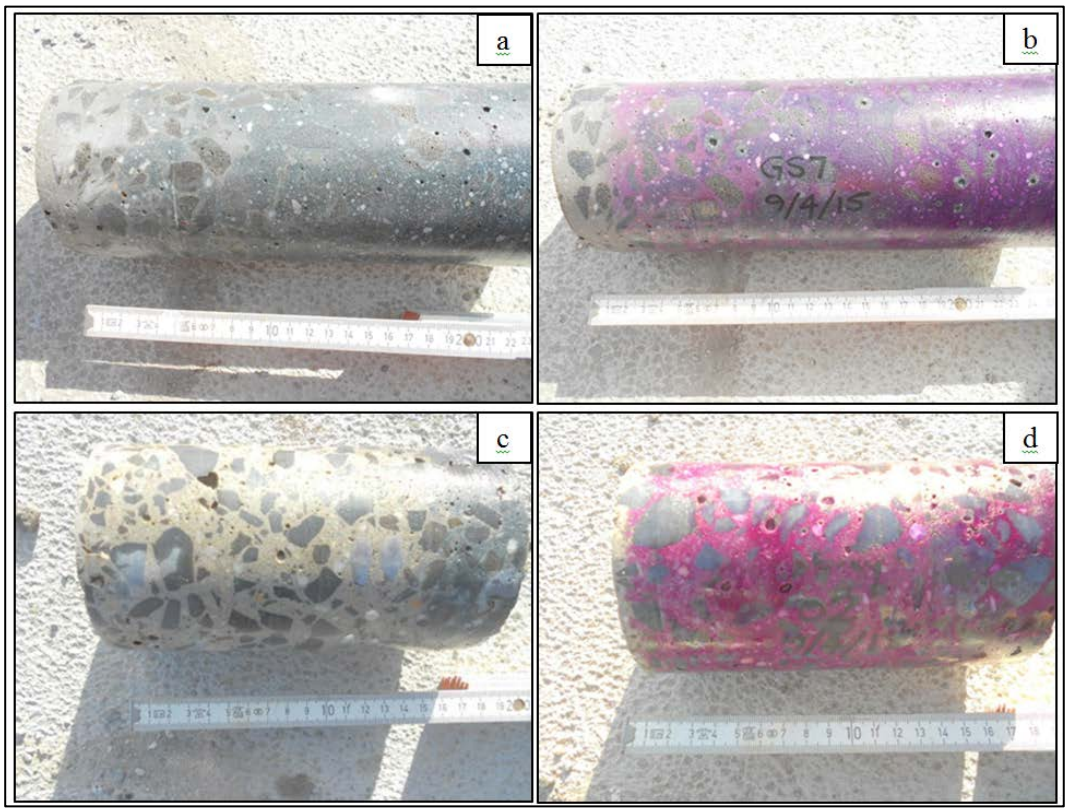

Figure 5. Carbonation depth measurements of core specimens using by phenolphthalein indicator (a) Type 1 specimen before applying phenolphthalein, (b) Type 1 specimen after applying phenolphthalein, (c) Type 2 specimen before applying phenolphthalein, (d) Type 2 specimen after applying phenolphthalein.

Figure 6. No clear carbonation front by phenolphthalein indicator for Type 1 and Type 2 specimens

pH measurements on concrete core samples

The pH variation against the depth in the concrete is shown in Figure 7. Both uncalibrated and calibrated pH profiles are plotted in Figure 7. Only the calibrated pH profiles are considered for the discussion. The pH of the Type 1 GPC ranges from about 10.07 at the surface to 11.25 at 50 mm depth. For Type 2 concrete, the pH ranges from 9.68 to 11.38. According to Khan et al [11], in Geopolymer concrete mix with high amount of low calcium fly ash, the phenolphthalein indicator starts to show uncoloured zones when pH is inferior to 10.5. Considering 10.5 as the carbonation front, Fig. 5 shows a good agreement between the pH profiles results and the carbonation front obtained using the phenolphthalein indicator (23.5-27.5 mm for Type 1 GPC and 8-14 mm for Type 2 concrete).

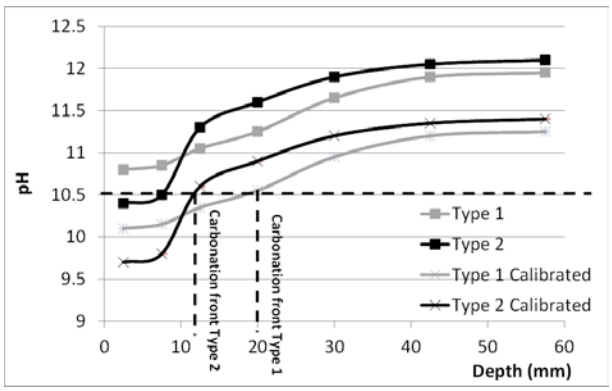

Figure 7. pH value versus depth in Geopolymer concrete from the surface.

Water absorption properties

The water absorption and apparent volume of permeable voids (AVPV) values of the core specimens are given in Table 3. The values of Type 1 specimens were calculated from average of four pieces and the value for Type 2 concrete determined with average of three pieces of the core specimen.

According to VicRoads Specification Section 610, Durability of the concrete can be classified using AVPV value of concrete core samples. From that, Type 1 Geopolymer concrete is under marginal category and Type 2 concrete is in normal classification. Results are in good agreement with the carbonation tests since the carbonation front measured in Type 1 GPC was much larger than the one obtained for Type 2 concrete. Moreover, the AVPV measured on the 13 years old OPC concrete [4] was around 15.2% which is close to the one obtained for Type 2 Geopolymer concrete. As a result, the OPC and Type 2 Geopolymer concretes have a similar AVPV values and show a similar performance to resist against carbonation in outdoor field conditions. It can be concluded, therefore, AVPV test is an appropriate test to assess Geopolymer concrete performance for carbonation.

Table 3 water absorption and AVPV values

Specimens No	Immersed absorption(Ai)%	AVPV%
Type 1	7.27	17.04
Type 2	6.39	14.35

Figure 8 presents the variation of water absorption with square root of time for both Types of Geopolymer concrete specimens. As similar to volume of permeable void test results, the sorptivity parameters of Type 1 GPC was higher than the Type 2 concrete. Therefore, this indicates, the Type 2 concrete contains less porosity with denser structure. This was confirmed by pore size distribution analysis, which will be presented further. Initial and final sorptivity rate calculated from water absorption plot are provided in Table 4.

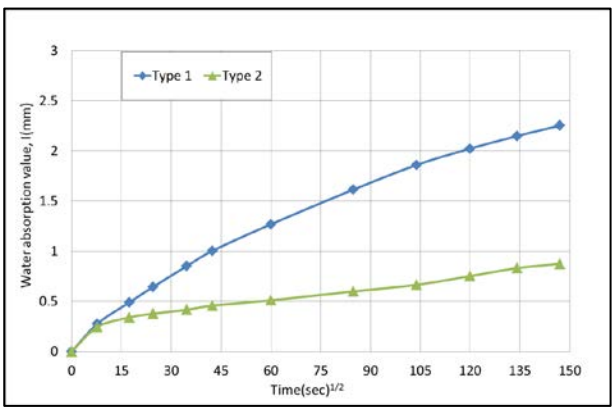

Figure 8. Test results from sorptivity analysis.

Table 4. Coefficients of sorptivity.

Specimens No	Initial absorption rate(mm/s$^{1/2}$)	Secondary absorption rate(mm/s$^{1/2}$)
Type 1	0.01405	0.0023
Type 2	0.0042	0.0010

Thermogravimetric analysis (TGA/DTG)

Figure 9 shows the differential thermogravimetry (DTG) and thermogravimetric analysis (TGA) curves of the Type 1 GPC samples at top 50 mm depth and 50-100 mm depth levels. The peak at 59.5^{0}C and 66.8^{0}C in DTG curves, related to dehydration of free water, C-S-H and N-A-S-H gel [12-17] respectively. The small peaks between 200^{0}C to 400 ^{0}C correspond to dehydration of C-A-S-H and C-A-H matrix [13, 16, 18]. In addition, DTG curves for top layer shows peak values at 700^{0}C due to the decomposition of calcium carbonate components [13, 16, 17, 19] and the peak at 897^{0}C relates to crystalized calcium carbonate (CaCO3) decomposition [13, 17]. In contrast, no endothermic peaks obtained for the temperature values in DTG curve for middle layer concrete. This indicates Type 1 Geopolymer concrete structure was carbonated within 50 mm depth levels and there was no carbonation reaction occurred beyond 50 mm depth.

The DTG and TGA curves of the Type 2 concrete (up to 50 mm depth from the surface) are shown in Figure 10. The endothermic peak at 75^{0}C derived due to dehydration of water and C-S-H gel and the peak at 448^0 C due to C-A-S-H and C-A-H matrix loss. It should be noted that the two minor peaks at 650^{0}C and 885^{0}C, corresponding to decomposition of calcium carbonate components and crystalized $CaCO_3$. Therefore DTG and TGA analysis confirmed that the both types of Geopolymer concrete structures were carbonated after exposed eight years in atmospheric environment. Moreover, the higher variation in the weight loss is due to the decomposition of the carbonate components and this indicates that the amounts of carbonation products are higher in Type1 concrete than in Type 2 Geopolymer concrete. This in agreement with carbonation depth values obtained using the phenolphthalein indicator or the calibrated pH profiles.

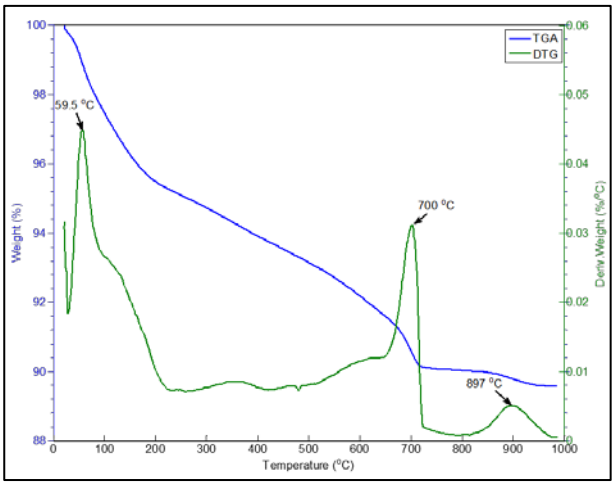

(a)

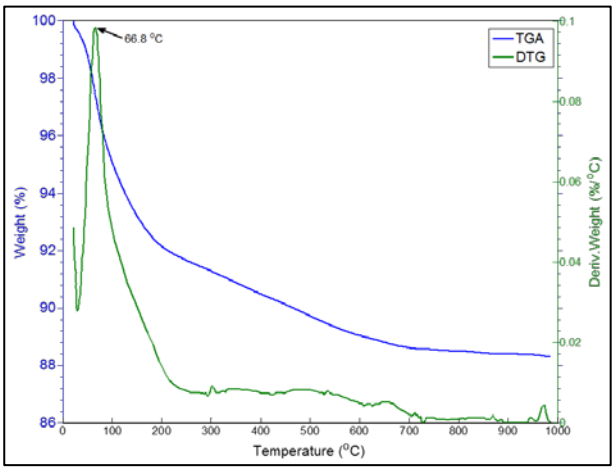

(b)

Figure 9. TGA/DTG graph of Type 1 GPC specimens a: Top layer, b: mid layer

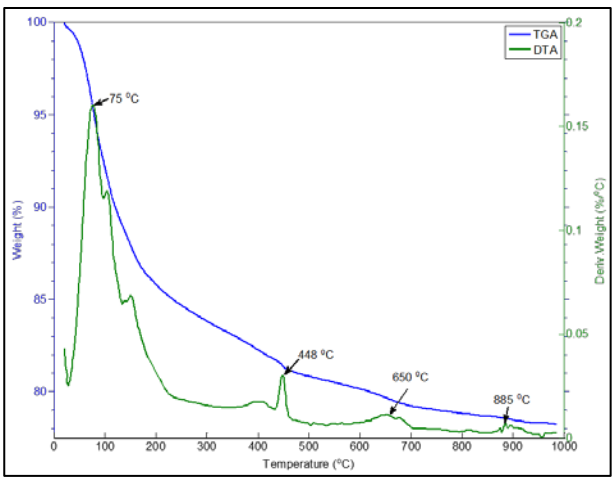

Figure 10. TGA/DTG graph of Type 2 concrete specimen: top layer

Fourier transforms infrared (FTIR) analysis

The infrared spectroscopic results for Type 1 GPC and Type 2 concrete up to top 50 mm depth levels of core specimens are shown in Figure 11. The IR spectrum shows the main intensity bands of Type 1 GPC as follows: 772, 871, 1000, 1410, 1630, and 3420 cm-1. The Type 2 concrete contains main adsorption bands at 641, 856, 953, 1460, 1630 and 3360 cm-1. The peak at 1000 cm-1 and 953 cm-1 are attributed to stretching vibrations mode of Si-O-T bond (T is Si or Al) in Type 1 and Type 2 concrete respectively. It should be noted that the main band wave number shifted to lower value in Type 2 concrete compared to Type 1. This is because of the high fly ash content in Type 1 GPC, which increased the formation of alumina silica Geopolymer gel and the presence of high level of unreacted fly ash particles [20] or the contribution of silicate activator in Type1 concrete.

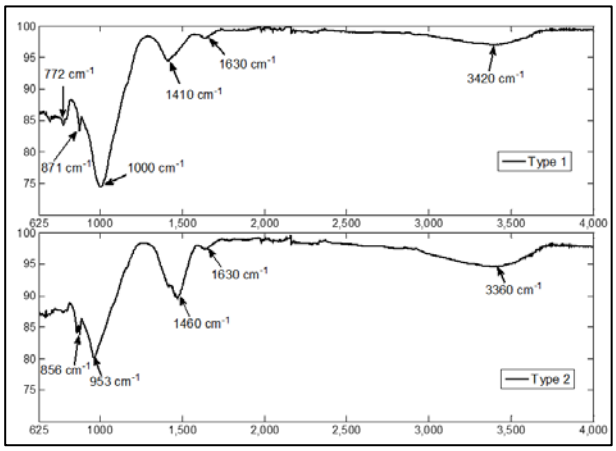

Figure 11. FTIR spectra for both type specimens (top layer).

The broad band between 3,000 and 3,600 cm^{-1} in Type 1 GPC and 3,000 to 3,800 cm^{-1} in Type 2 concrete is associated with stretching vibration of OH and H-O-H groups from hydration reaction product of Geopolymer. The peak at 1,630 cm^{-1} in both types of concrete can be attributed to the bending vibration of OH groups. The peaks at 871 and 1,410 cm^{-1} in Type 1 and and 856 and 1,460 cm^{-1} in Type 2 may be due to the stretching vibration band of O-C-O in carbonate (CO_3^{2-}) components [21]. Furthermore, the peaks at 698 and 772 cm^{-1} in Type 1 GPC and the peaks at 641 cm^{-1} in Type 2 concrete is attributed to the bending vibration mode of Si–O–Si or Si–O–Al gel.

Pore size distribution analysis

The differential pore size distributions of both types of Geopolymer concrete specimens derived from mercury intrusion porosimetry (MIP) analysis are shown in Figure 12. It can be seen from Figure 12 that the top and mid layers of the same type of concrete demonstrate similar pore size distribution characteristics. The overall pore characteristic details are provided in Table 5. According to Figure 12 and Table 5, top and mid layers of the Type 1 specimen contain higher porosity compared to Type 2 specimens. The top and mid layer of the Type 1 GPC specimens have a total porosity of 17.6% and 17.2% and the total porosity of Type 2 concrete specimens for the relevant layers are 11.8% and 11.2%, respectively. Therefore, the porosity of the concrete specimens is correlated with carbonation results; i.e., the lower porosity concrete shows the higher resistance to carbonation in field environment.

Although the porosity of top layer in Type 1 GPC is high, it possesses lower total pore area and higher average pore diameter values compared to Type 2 concrete top layer. This suggests that the Type 1 GPC consist high amount of larger size pores compared to Type 2 concrete. It is also noted that the Type 2 concrete contain fine pores and the maximum amount of pores occur at the pore diameters of 4.7 nm and 5.3 nm for top and mid layers, respectively. On the other hand, the maximum amounts of pores at the top and mid layers of Type 1 GPC specimens are occur at the pore diameter of 15.7 nm. Therefore, Fig. 10 and Table 6 confirms that the most of the pores in ambient exposed Geopolymer concrete are of the harmless and less harmful type, because noticeable amount of pores occur at the diameter less than 50 nm [22].

However, the Type 1 GPC still shows noticeable amount of pores with the diameter between 50 nm to 150 nm (Figure 12), which are harmful pores. Therefore, it can be concluded that the Type 1 GPC contain high amount of harmful pores which can promotes the penetration of CO_2. This was also confirmed with the carbonation test results, where the penetration of CO_2 was high in Type 1 Geopolymer concrete surface in ambient environment.

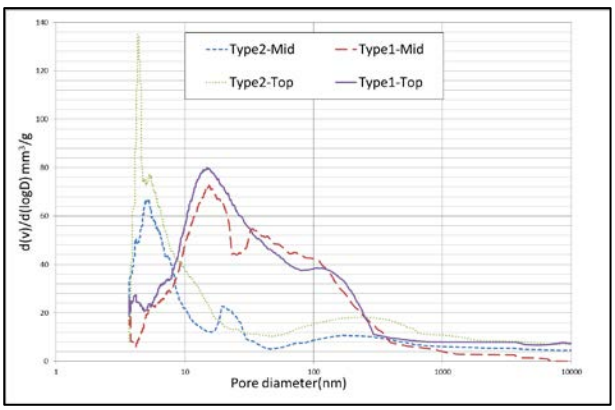

Figure 12. Differential pore size distribution obtained for both types of Geopolymer concrete.

Table 5. Pore characteristics of both types of Geopolymer concrete specimens.

	Porosity (%)	Total pore area(m^2/g)	Avg.Pore diameter(nm)
Type1-Top layer	17.6	15.3	23.6
Type 1-Mid layer	17.2	19.0	22.9
Type 2-Top layer	14.9	22.8	13.5
Type 2-Mid layer	11.8	16.6	12.5

Conclusions

The carbonation resistance of Geopolymer concrete structures exposed to an atmospheric environment was investigated. Available test results in the literature were used to compare the performance of Geopolymer concretes to that of OPC concrete, in similar exposure conditions. The following conclusions can be drawn from this study.

1 Carbonation rate of Geopolymer concrete highly depends on the mix design of materials. Type 1 Geopolymer concrete, with 75% fly ash/25% GGBFS and additional Na_2SiO_3 activator, showed a poor resistance against carbonation compared to OPC concrete. In contrast, the performance of Type 2 Geopolymer, with 70% fly ash/30% GGBFS and no additional Na_2SiO_3 activator, was similar to OPC concrete.

2 Thermogravimetric (TGA/DTG) and Fourier transforms infrared (FT-IR) analyses revealed the presence of carbonation reaction products such as calcium carbonate components and crystallised $CaCO_3$.

3 The volume of permeable voids test and sorptivity analysis showed that the permeation properties are strongly related to the carbonation rate of Geopolymer concrete. The test results show that the higher carbonation Geopolymer (Type 1) contains high permeation whereas less permeation characteristics were identified in lower carbonated concrete (Type 2).

4 The MIP analysis illustrates the relationship between carbonation and the porosity of the concrete. Specifically, the test results revealed that the Type 1 GPC contains higher porosity and larger average pore diameter than Type 2 concrete.

5 Finally, this study shows that the performance of two Geopolymer concretes, which differed only slightly in both mix design and compressive strength, had different resistance to carbonation. Therefore, a performance based approach is an appropriate strategy to develop standard specifications for Geopolymer concrete.

Toowoomba, Queensland (UNSW)

Introduction

Geopolymer and OPC concrete water tanks located at Toowoomba site, Queensland were investigated in December 2015, as shown in Figure 13. The water tanks experienced cracks that extended to the outer surface of the concrete tank. In both cases, the cracks were partially healed. Figure 14 shows the surface crack in one Geopolymer concrete water tank.

A study was carried out to investigate the healing mechanism of Geopolymer concrete. To this end, two concrete cores were obtained from Geopolymer concrete tank: one specimen along the crack and another one having where no cracking was evident. Figure 15 illustrates coring of the Geopolymer concrete water tank in progress. The core samples for Geopolymer (EFC) and OPC concrete are given in Figures 16 and 17, respectively.

Carbonation behaviour of both concretes was assessed through pH profile and phenolphthalein test using cores with no cracks. Scanning electron microscopy (SEM), energy dispersive spectroscopy (EDS) and Raman spectroscopy were carried out to identify the crystalline products that may have formed in the self-healed zone.

Figure 13. Geopolymer and OPC concrete water tanks at Toowoomba site, QLD ,in December 2015.

Figure 14. Surface crack of Geopolymer concrete water tank at Toowoomba site, QLD, in December 2015.

Figure 15. Coring of OPC concrete water tank at Toowoomba site, QLD, in December 2015.

Figure 16. Geopolymer concrete core taken from water tanks at Toowoomba Site, QLD, in December 2015.

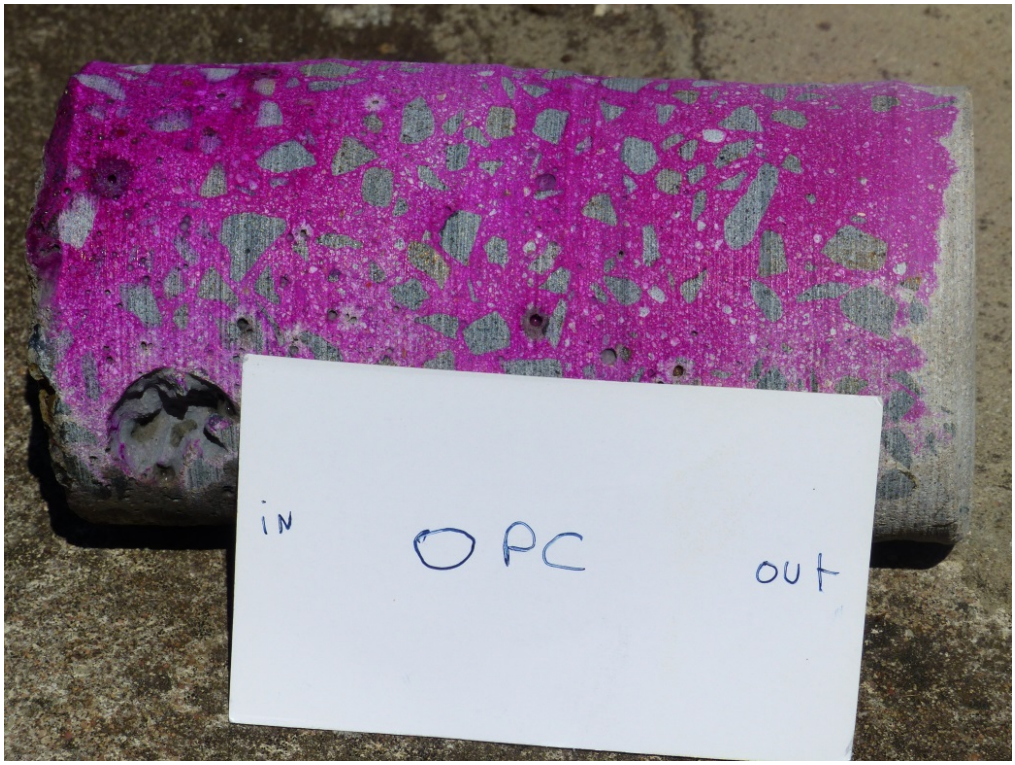

Figure 17. OPC Concrete core from water tanks at Toowoomba site, QLD, in December 2015.

Table 6. pH value and ion contents of water in the tanks.

Water type	pH	Ca (mg/L)	Al (mg/L)	Si (mg/L)	Fe (mg/L)	Mg (mg/L)	K (mg/L)
Water from EFC tank	7.60	32.3	0.01	12.7	0.02	26.5	1.57
Water OPC concrete tank	7.47	22.7	0.02	7.83	0.04	15.4	1.18

Test results

pH and ion content of water inside of the tanks

Table 6 presents the pH values and the ion contents of water in both tanks. It can be seen that the pH of the water in each tank is well within World health Organisation guidelines for potable water[1].

Phenolphthalein test

Figure 16 and Figure 17 show the core specimens after spraying of phenolphthalein indicator. It can be seen that in Geopolymer specimen, the carbonation depths were about 13 mm on the side exposed to the atmospheric CO_2 (outer side) and only about 3 mm on the side exposed to leaching (inner side). For OPC, the carbonation depth was about 4 mm on the outer side and there was no clear uncoloured zone in the inner side of the specimen.

pH profile in the concrete

Figure 18 illustrates the pH profiles of the Geopolymer concrete specimen both in outer and inner sides. The figure shows that on the outer side (carbonation side), the minimum pH value is 9.1. This increases up pH 11 at a depth of about 12 mm; beyond this depth the pH increases gradually to the uncarbonated region where pH is around 12.2.

Previous work has shown that phenolphthalein indicator becomes uncoloured when pH is lower than 10.5. Thus the pH profile confirms the carbonation depth of about

[1] WHO guidelines recommend pH of between 6.5 and 8.5 for potable water and pH of between 7 and 8 for water supply, where disinfection is needed and corrosive environments are to be avoided: http://www.who.int/water_sanitation_health/water-quality/guidelines/en/

12 mm. On the inner side (leaching side), the value is less than pH 10 for first 3 mm and then gradually converges towards the uncarbonated region. The effect of leaching is seems marginal compared to carbonation.

Figure 19 shows the pH profiles of OPC concrete specimen. It can be seen that on the outer side, pH is about 10 at 1 mm depth, and reaches about 12 at depth of 3.5 mm. On the inner side, the pH value is close to 12 at just 1 mm. Both profiles in OPC specimen also correlate well with the observations from the phenolphthalein test.

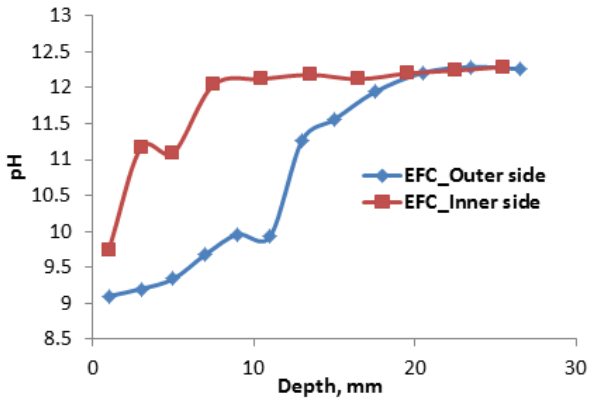

Figure 18. pH profiles of EFC specimen.

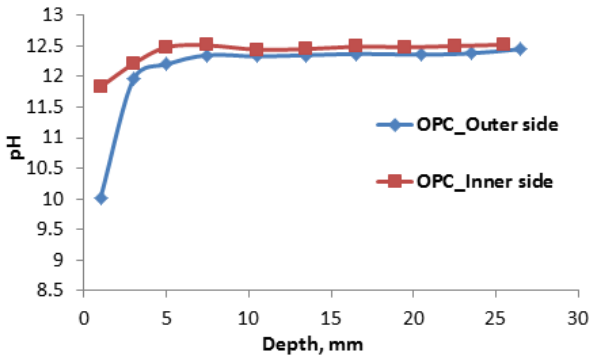

Figure 19. pH profiles of OPC concrete specimen.

It is recognised that carbonation is strongly affected by relative humidity and, therefore, a component of the difference in the depth of carbonation is likely to be due to a difference in moisture movement through the concrete.

Identification of carbonation products

Energy dispersive spectroscopy (EDS) was performed on a Geopolymer concrete specimen. The specimen was split along the crack and EDS was carried out on fractured surface. Figure 20 shows the EDS point scan results of Geopolymer concrete specimen. Both figures show the formation of some platy like crystals. EDS spectra confirm that the platy like structures only contain Ca and O.

Based on the EDS results, the probable crystalline products would be $CaCO_3$ or $Ca(OH)_2$. In order to identify the crystalline product, Raman spectroscopy was carried on the fractured surface. Figure 20 shows the Raman spectrum observed on fractured surface of EFC specimen. The figures shows that the intensity peaks of the observed spectrum of EFC coincide with the reference spectrum of calcite, indicating the formation of calcite in the self-healed zone. This result suggests that the penetrating CO_2 reacts with EFC and forms calcite as a carbonation product that subsequently heals the cracks. As a result, the self-healing process occurring is similar to OPC.

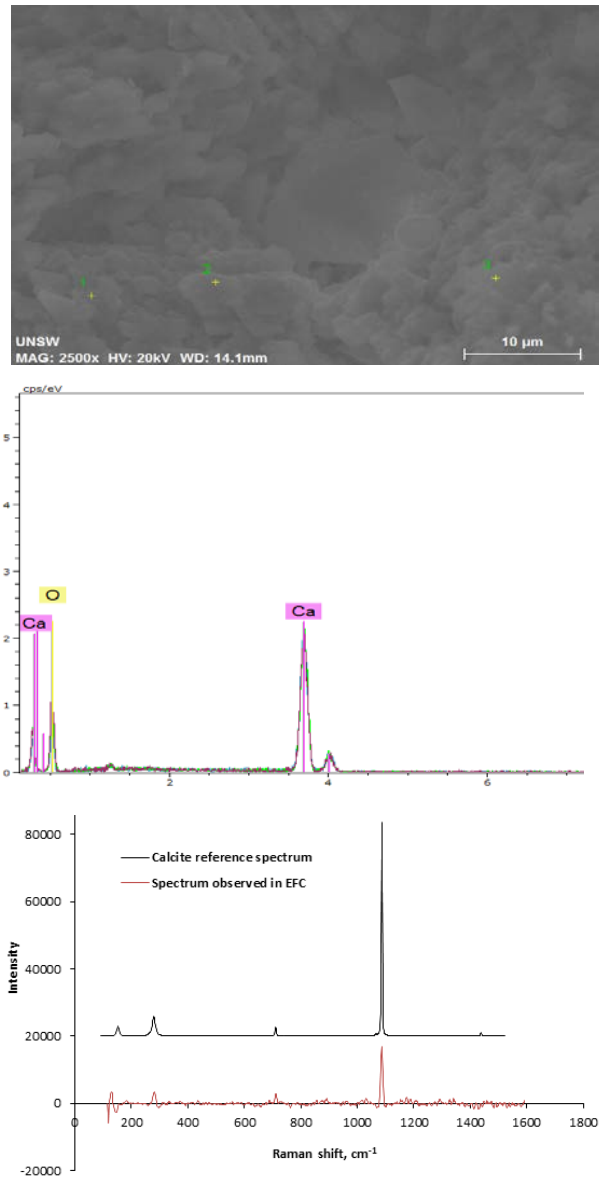

Figure 20. EDS results and Raman spectra of EFC specimen.

Conclusions

The following conclusions are made from this study:

1. Carbonation rate of the slag based Geopolymer concrete was higher than that for the OPC concrete control; and
2. Slag based GPC can experience efficient self-healing due to the formation of Calcite.

Lake King Western Australia (SUT)

Introduction

Geopolymer concrete box culverts located at Lake King in Western Australia were investigated. The site is 430 km west of Perth. The culverts were installed in an inland salty lake in December 2009 as part of a Curtin University research project. AS 3600 exposure classification for saline environments is U. The culverts were cast using concrete based on fly ash activated with combination of sodium silicate and sodium hydroxide activator and curing by using steam curing method. Culverts constructed from ordinary Portland cement (OPC) concrete were also exposed at the same site and enable direct comparison of performance. After three years of exposure in the saline environment, chloride diffusion coefficient, carbonation, resistivity and pH value were determined by Dr. Didar Cheema (Main Roads Western Australia) for his research study. In October 2015 additional inspection, in-situ testing and core sampling were performed. The testing enabled monitoring the behaviour of both Geopolymer and OPC concrete in a saline environment versus time.

Figures 21 and 22 show, respectively, the Geopolymer and the OPC concrete culverts.

The following in-situ tests were performed on the culverts:

- resistivity;
- half-cell potential and corrosion rate; and
- air permeability.

In addition, core samples were extracted from the culverts and underwent the following investigations:

- visual condition, including any corrosion of reinforcement;
- carbonation measurement;
- pH profile;
- chloride concentration profile;
- volume of permeable voids;
- sorptivity; and
- microstructure and phase analysis by using SEM, XRD, FTIR and TGA methods.

Figure 23 illustrates coring of the Geopolymer concrete culvert in progress and Figure 24 shows a typical core sample.

Figure 21. Geopolymer concrete culvert at Lake King site, WA, in October 2015.

Figure 22. OPC concrete culvert at Lake King site, WA, in October 2015.

Figure 23. Coring of Geopolymer concrete culvert at Lake King site, WA, in October 2015.

Figure 24. Typical Geopolymer concrete core sample from Lake King site, WA, in October 2015.

Test results

Scaling effect and sulphate penetration in concrete

Figure 26 depicts the visual appearance of the concrete structures after 6 years of exposure in the saline environment. The OPC concrete structure showed no significant changes in the visual appearance over time. In contrast, the mortar from the GPC surface, especially from the leg part of the culvert that is frequently in contact with saline lake water, has been lost and the aggregate is clearly exposed on the surface as also has been observed previously [23]. This is called a scaling effect in concrete structures. Salt scaling occurs when the concrete surface is subjected to accelerated wet and dry cycles. This induces a salt deposit on the concrete surface, which results in severe damage to the surface of concrete. Here, in addition to salt crystallisation, the presence of a high quantity of $MgSO_4$ components in the soil and lake water also provides a higher scaling effect on the concrete structure. Soil rich in sulphate can also cause the deterioration of the concrete structure and spalling of the concrete surface due to the reaction between the sulphate ions and the hardened concrete [24] and the diffusion of Mg^{2+} ions also deteriorate the binder in the concrete.

Although both structures were exposed to a similar environment, the scaling effect in GPC was high, whereas no significant effect was identified in OPC structure. It should be noted that the interaction between Geopolymer concrete and the sulphate or the chloride ions from saline water is significantly different to the reaction between OPC concrete and those aggressive agents. This is due to the nature of the aluminosilicate gel in Geopolymer materials compared to hydration reaction components. Geopolymer concrete is rich in Na in the pore solution and this produces thenardite (Na_2SO_4), from the reaction with sulphate ions. Hime et al. [25] determined that the thenardite turns to mirabilite (Na_2SO_4. $10H_2O$) components during the wetting periods and this causes an expansion of the structure. This can therefore explain the higher scaling activity in GPC compared to OPC concrete. The test results of the sulphate measurements of core specimens extracted from the leg parts of the box culvert are shown in Figure 25 and this confirmed that the GPC had higher sulphate ingress compared to OPC concrete.

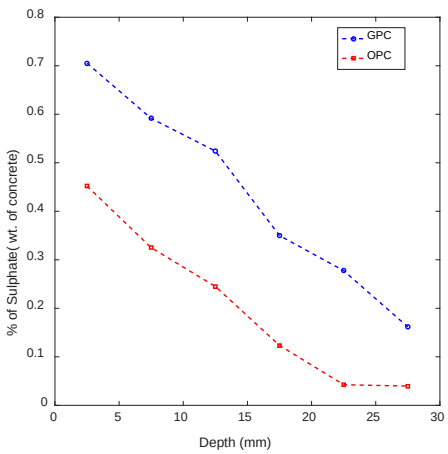

Figure 25. Sulphate measurements of concrete.

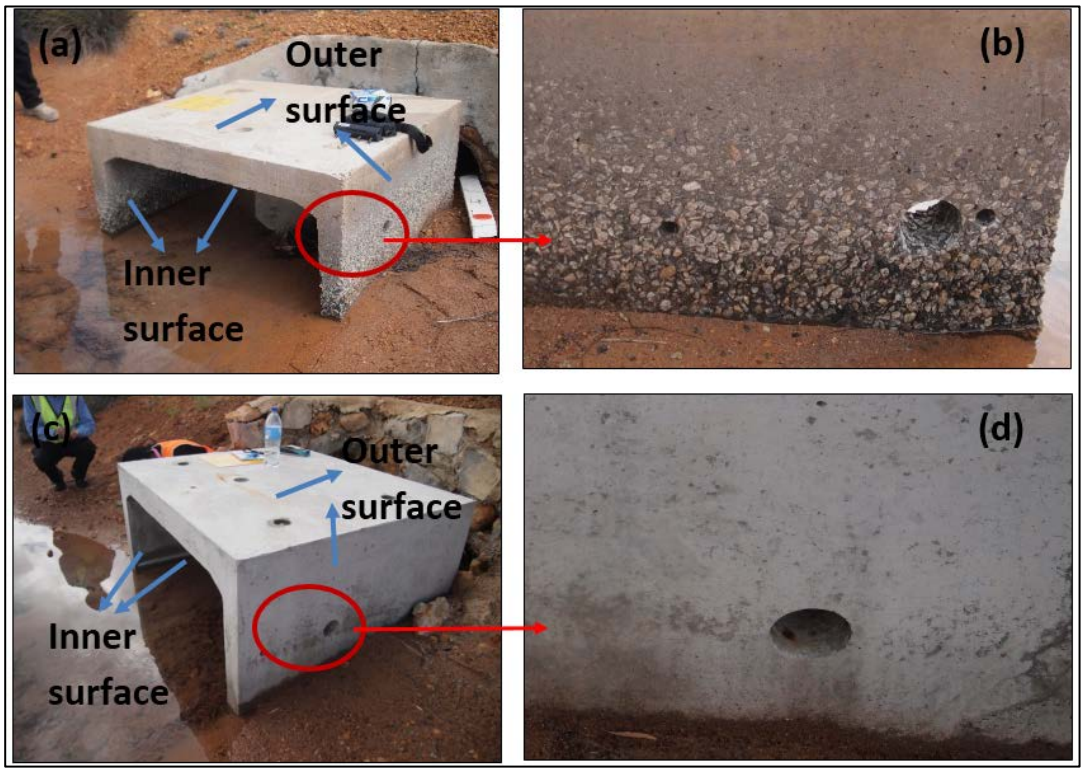

Figure 26. Visual appearance of concrete structure (a) GPC concrete culvert, (b) outer surface of GPC showing exposed aggregate, (c) OPC concrete culvert, (d) outer surface of OPC with no visual evidence of deterioration.

Carbonation resistance of field exposed GPC

Carbonation depth measurements obtained using the phenolphthalein indicator are presented in Figure 27a. The application of the phenolphthalein indicator revealed that the carbonation rate in GPC concrete was much greater than that of OPC concrete in the same environment. The core specimens from the GPC concrete culvert remained colourless after phenolphthalein application for the entire depth (approximately 90 mm of leg parts and 135 mm of the top slab of the culvert). However, some shades of colour were observed unlike OPC where the carbonated remain completely colourless. It is thought that this effect observed in GPC is combined actions of leaching to the running water and carbonation. The carbonation depth values derived from the OPC concrete core specimens are provided in Table 7.

As shown in Table 7, the carbonation rate in the top slab area was higher than the leg parts of the culverts due to the moisture variation between the slab surface and leg parts of the culvert, which would affect the diffusion of CO_2 to the concrete surface. Since the top slab is subjected to the sun, the humidity within the concrete is less compared to the leg part of the culvert, which is located within the tidal or splash zone of the lake. Internal humidity of concrete is known to have a strong influence on carbonation rate [26]. It can be concluded, therefore, that the high moisture content is contributing to the lower carbonation effect in the leg part of the culvert by lower CO_2 diffusion. On the other hand, the GPC concrete core specimens from both atmospheric and splash zones reveal that the carbonation rate in GPC concrete is high compared to OPC concrete under wet and dry conditions. In fly ash based GPC concrete, sodium carbonate (Na_2CO_3) is formed as a primary carbonation product and this product would be dissolved in water when it is exposed to field environments. Therefore, removal of this carbonation component from concrete surface can increase the porosity and causes higher CO_2 diffusion through the concrete surface. This will be discussed further in section below.

Table 7. Carbonation depth measurement of OPC concrete.

Core No	Carbonation depth measured from outer surface	Carbonation depth measured from inner surface
OPC 1(Leg)	10 mm	0 mm
OPC 2(Leg)	7 mm	0 mm
OPC 3(Leg)	5 mm	4 mm
OPC 4(Leg)	5 mm	4 mm
OPC 5(Top slab)	20 mm	10 mm
OPC 6(Top slab)	20 mm	9 mm

pH measurements on concrete core samples

The pH value versus depth of concrete is presented in Figure 27b. Since the CO_2 and chloride ions can penetrate through both surfaces (outer and inner surface) of the culverts, the pH analysis was conducted on the powder samples collected from both sides of the core specimens. The powder sample was collected with 5 mm depth intervals up to 30 mm depth from the outside and inside exposed surfaces. The pH trend of GPC was around 7.0 to 7.5 from the outside and inside surface. The pH of OPC concrete was in the range of 8.5-10, which is significantly higher than the pH of GPC concrete. It shows that the combined action of leaching and carbonation is more aggressive in GPC than in OPC for the same exposed environment.

The GPC prepared with same mix composition exposed to atmospheric environment for 8 years displayed a pH range 9.9 to 10.4 from the exposure surface to 30 mm depth level [27]. This range is higher than the pH range obtained for saline environmental exposed GPC concrete. In a saline environment, ingress of salt and carbonation to the concrete surface induces a greater pH reduction compared to the concrete structures exposed to the atmospheric environments. In addition to the salt ingress, the pH reduction in GPC is also due to the wash out of soluble Na_2CO_3 by contact with water whereas insoluble calcium carbonation is produced when OPC concrete carbonates.

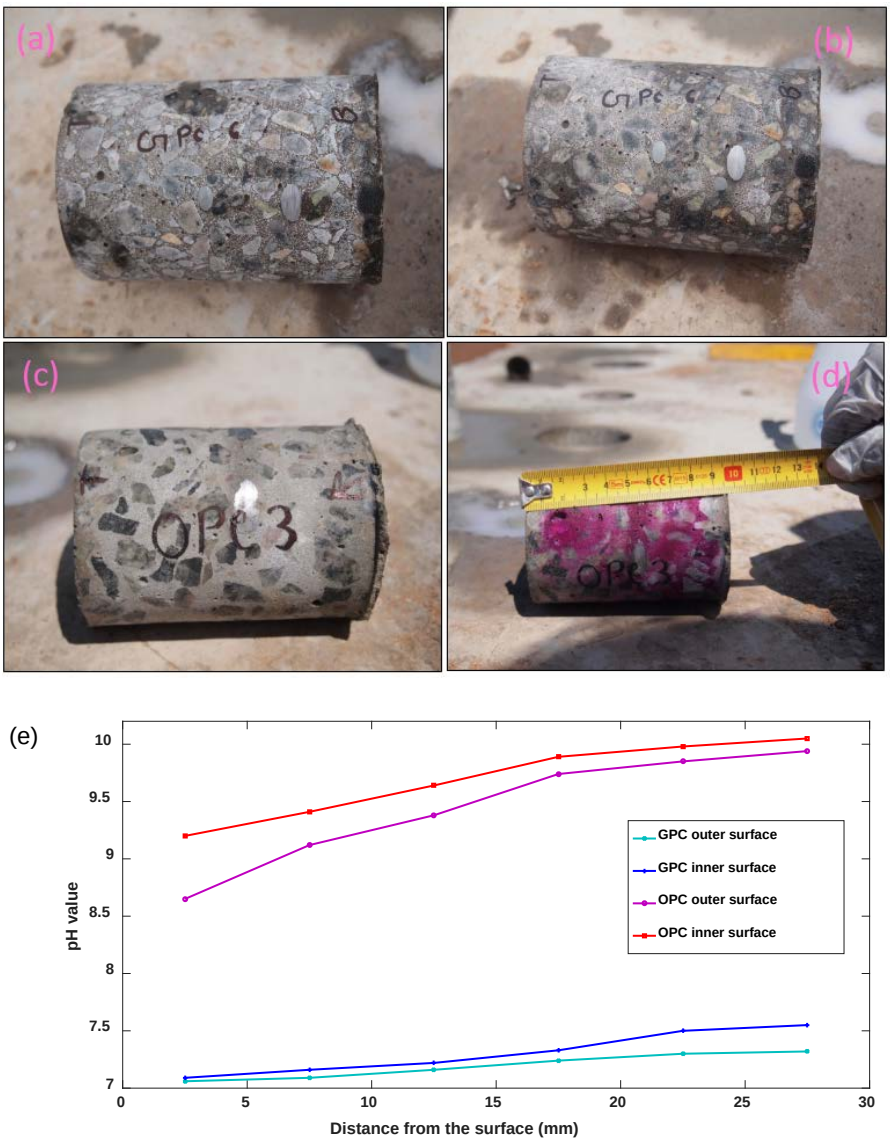

Figure 27. Carbonation depth measurements of core specimens using a phenolphthalein indicator: (a) GPC specimen before applying phenolphthalein; (b) GPC specimen after applying phenolphthalein; (c) OPC specimen before applying phenolphthalein; (d) OPC specimen after applying phenolphthalein; and (e) pH variation with depth values.

Fourier transforms infrared (FTIR) analysis

The FT-IR technique was used as a qualitative method to identify the effect of carbonation on concrete. Carbonation depth was determined from the position of the C–O characteristic peaks relative to the baseline at wave range 1410-1420 cm^{-1} [21, 27]. The FT-IR spectrum of GPC concrete specimen is presented in Figure 28. 'GPC T' series reflect the powder samples collected from the outer surface of structure with 5 mm depth intervals, whereas 'GPC B' series indicate the test results from the powder sample collected from the inner surface of the structure.

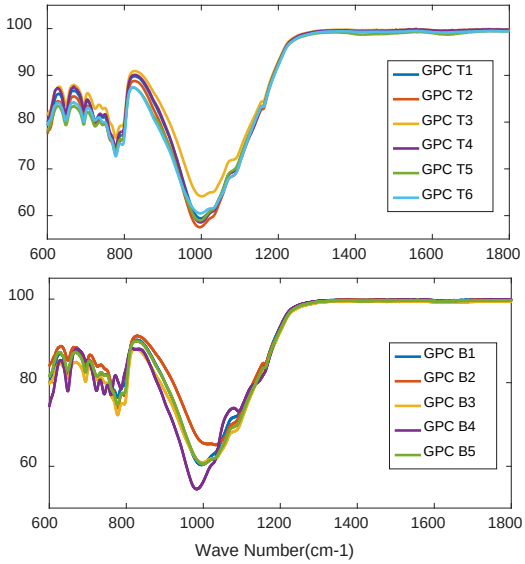

Figure 28. FTIR spectrum of GPC concrete samples with various depth intervals.

Similarly, in Figure 29, 'OPC T' and 'OPC B' are associated with the test results of powder collected from the outer and inner surface of OPC concrete specimens, with 5 mm depth variation, respectively. As shown in Figure 28 and Figure 29, the C-O bond was not recognized in all GPC concrete samples. However, the application of phenolphthalein indicator showed that all the GPC concrete core specimens were entirely carbonated (90 mm and 135 mm) and the pH profile measurements also confirmed the carbonation in GPC concrete. Therefore, the FT-IR results reveal no carbonation components presents in fly ash based GPC concrete under field exposed condition.

The formation of Na_2CO_3 in fly ash based GPC has been identified in previous studies by FT-IR assessment of laboratory prepared specimens at the wave number 1460 cm^{-1} [28]. An accelerated carbonation test was therefore conducted on laboratory prepared concrete specimens to ensure the presence of the carbonation component in fly ash based GPC. Cylindrically shaped specimens with 100 mm diameter were prepared with a similar mix composition and an accelerated carbonation test was carried out in a carbonation chamber at 21°C with 65% relative humidity. Since higher concentrations of CO_2 produce bicarbonate components in Geopolymer

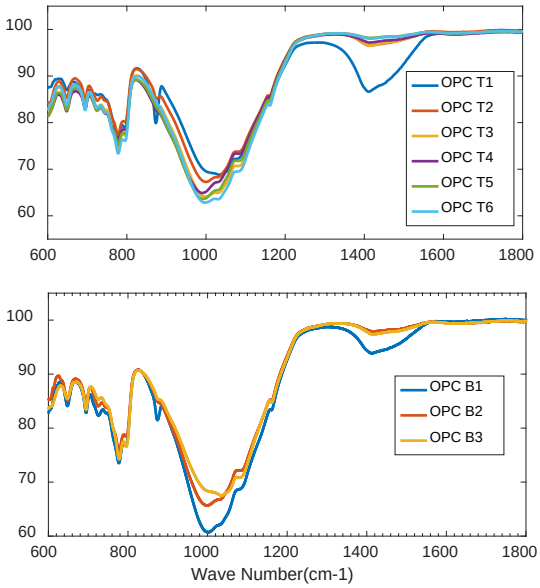

Figure 29. FTIR spectrum of OPC concrete samples with various depth intervals.

concrete [29], the concentration of CO_2 used in this experiment was 1% to produce the same type of products that would form under natural carbonation conditions. Figure 30 shows the FT-IR results for the sample collected from a specimen that was exposed to the carbonation chamber for 4 weeks and the powder sample extracted from the GPC culvert core specimens at a depth level of 0-5 mm. According to Figure 30, the C-O bond was recognized in laboratory prepared GPC samples at 1450 cm^{-1}. This suggests that carbonation components have been formed in the fly ash based Geopolymer concrete samples. Therefore, carbonation reaction products in the GPC culvert appear to have dissolved in water from rain and the lake under field exposure conditions. In contrast, a solid dense layer of calcite ($CaCO_3$) is formed as a result of carbonation in OPC concrete by the dissolution of CO_2 in the concrete pore fluid and this reacts with calcium from calcium hydroxide ($Ca(OH)_2$) and calcium silicate hydrate. The formation of this water insoluble densified layer on concrete surface further reduces the carbonation rate.

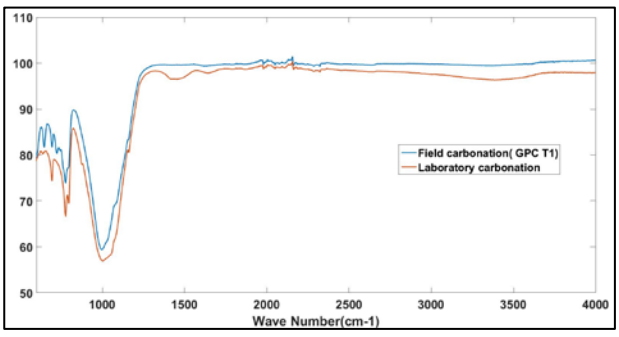

Figure 30. FTIR spectrum of GPC concrete samples (field and laboratory)

The FT-IR analysis of OPC concrete (Figure 29) revealed that the C-O bond was identified up to 30 mm depth from the outside surface and 15 mm from the in-

side surface. However, application of the phenolphthalein indicator showed that the maximum carbonation depth values of the leg part OPC concrete cores was approximately 10 mm. The carbonation depth results from FT-IR analysis are therefore clearly higher than the field measurement by phenolphthalein solutions and it is known that the carbonation front is ahead of that shown by phenolphthalein [30]. The phenolphthalein indicator can only determine the complete carbonation zone when the pH range is less than 9.0 (presence of more $CaCO_3$ components), whereas the FT-IR test is an accurate method to identify the partially carbonated zone, which contains the combination of $Ca(OH)_2$ and $CaCO_3$ components. The pH range of the partially carbonated zone is about 9.0-11.5 [27] and the carbonation depth with this pH range cannot be determined accurately by phenolphthalein. A higher carbonation depth was therefore obtained from FT-IR spectrum due to the presence of a partially carbonated zone. However, comparing to other depth intervals, a higher intensity peak was observed for the powdered samples collected from the surface to 5 mm depth intervals at the band 1410-1420 cm^{-1} and the stretching vibration of CO_3^{2-} was also recognized at the band 873 cm^{-1} [21]. The peak obtained at 1410-1420 cm^{-1} is due to the existence of calcite and the carbonation components, such as vaterite and aragonite were identified at the band of 873 cm^{-1}[31]. This indicates that, the effect of carbonation is high in the first layer (up to 5mm) compare to other layers. Further, peak obtained at 1100 cm^{-1} in Figure 28 and Figure 29 is corresponding to the S-O bond [32], which confirmed the penetration of sulphate ion from the environment.

Chloride penetration of concrete

Profiles of free chloride

The test results of the free chloride measurements of core specimens extracted from the leg parts of the box culvert are shown in Figure 31. Free chloride profiles are plotted with the Fick's second law mathematical equation. According to Figure 31, the series indicated as 'GPC T' and 'GPC B' are associated with the free chloride profile of GPC concrete samples, collected from outer and inner exposed surfaces, respectively. Similarly, 'OPC T' and 'OPC B' were assessed with the powder samples collected from outer and inner surface of the OPC concrete culvert. As shown in Figure 31, chloride penetration in GPC specimens was found to be greater than in OPC concrete. The free chloride contents at 30 mm depth from the outer surface and inner surface of GPC concrete exceeded or were close to the value of 0.4% free chlorides by weight of concrete. This indicates that the chloride content of GPC is sufficient to initiate corrosion activity in the reinforcement due to a rupture of the passive layer. On the other hand, the amount of free chloride in the OPC concrete was low compared to GPC concrete. Inspection of the steel bars in the GPC concrete also confirmed the presence of corrosion whereas bars in the OPC concrete were not corroded.

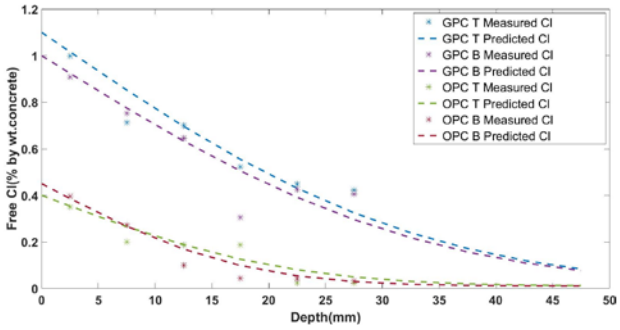

Figure 31. Free chloride variation with depth values.

Alumino silicate gel (N-A-S-H) structure is the main reaction components in fly ash based GPC concrete. This is a three dimensional network product and therefore this promotes a higher porosity in concrete structures. In addition, the presence of un-reacted fly ash particles in GPC concrete also caused the higher porosity GPC and a higher transfer of chloride ions into the concrete surface [33]. However, the inclusion of slag into fly ash based system produces a dense C–S–H phase, in addition to N-A-S-H gel, establishes a highly refined pore network by filling the pore volume of aluminosilicate Geopolymer gel and reducing the chloride ion penetration to the concrete surface [34]. Here, only fly ash was used as a precursor for the Geopolymer concrete. Therefore, high chloride penetration results are attributed to the porous structure of GPC concrete.

Total chloride content and diffusion coefficient

The chloride diffusion coefficients of the core specimens were calculated according to Fick's second law mathematical equation, provided below [35]

$$Cx = Cs\left(1 - erf\left(\frac{x}{4\,Da \times t}\right)\right) \quad (1)$$

where *Cx* is chloride concentration at depth *x*, *Cs* is surface chloride content at the surface, *Da* is apparent diffusion coefficient, *x* is depth, *t* is time of exposure and *erf* is an error function.

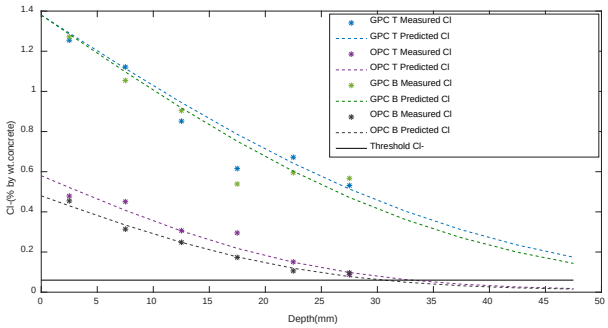

Figure 32. Total chloride variation with depth values.

The apparent diffusion coefficient (Da) and the surface chloride content (Cs) were calculated by plotting the chloride profiles and determining the best fit curve using Fick's second Law equation. Figure 32 illustrates the plots of total chloride content by weight of concrete versus depth and Table 8 summarises the Da and Cs of

both types of concrete. As previously mentioned, 'GPC T', 'GPC B', 'OPC T' and 'OPC B' are associated with the total chloride profile of powder specimens collected from the outer and inner surface of GPC and OPC concrete, respectively. According to Figure 32 and Table 8, the chloride content in GPC was much higher than the chloride contents in OPC concrete and, moreover, GPC concrete showed high diffusion coefficient values compared to OPC concrete. The predicted chloride curves indicate that the amount of chloride content at the reinforcement (45 mm depth) of GPC concrete would be greater than the assumed threshold Cl^- limit values (0.06% by wt. of concrete), whereas the predicted chloride content at the reinforcement bar in OPC concrete is at the lower level of the threshold limit. This is consistent with the observation of corrosion of reinforcement in the GPC but not the OPC concrete.

Table 8. Apparent diffusion coefficient and surface chloride content values.

	Apparent diffusion coefficient (Da)×10-12 m^2/s	Surface chloride content (Cs) (% by wt. of concrete)
GPC T	2.50	1.38
OPC T	1.0	0.58
GPC B	2.20	1.38
OPC B	0.95	0.48

It is well established that the chloride diffusion and the surface chloride content of concrete depends on the mix proportions, especially the binder type and curing conditions [36]. In this study, two different curing processes were conducted, a heat curing method for GPC concrete and an ambient temperature curing for OPC concrete. The high temperature curing method accelerates the curing process and produces better chloride resistance than ambient cured concrete at the younger stage, whereas ambient cured concrete may contain lower chloride diffusion at the latter stage due to the continuous curing process with age [37]. In past studies, fly ash based GPC concrete showed lower chloride diffusion compared to OPC concrete at an early age [8, 38, 39], whereas this investigation showed that the GPC concrete had higher chloride diffusion than OPC concrete after 6 years of exposure. It can therefore be concluded that the higher chloride diffusion in fly ash based GPC after long-term exposure in the saline environment is associated with the heat curing process, which reduces the continuous reaction in GPC concrete. In addition, the presence of a C_3A component (tri calcium aluminate) or C_4AF (tetra calcium alumina ferrite) phases and C–S–H gel in OPC concrete binds the chlorides [40]. By contrast there is no C_3A constituent in fly ash based Geopolymer concrete, which contributes to the higher chloride diffusion compared to OPC concrete [41]. It has also been demonstrated that the chloride ions in OPC concrete are bound forming Friedel's salt and calcium chloride phases, from the reaction between hydration phases of cement and chloride. The formation of soluble metal salt components, as a reaction between Geopolymer concrete phases and chloride ions, would not be sufficient to provide binding capacity [42].

The higher surface chloride concentration in GPC concrete samples is possibly also related to the availability of carbonation reaction components in the concrete surface. In OPC concrete, the pore structure of the concrete surface is filled with $CaCO_3$ components, which reduces the surface chloride, whereas in GPC, the pore structure enhancement with carbonation induces the higher sorption on the surface, which increases the concentration of surface chloride. Overall, compared to OPC concrete, the effect of chloride and chloride diffusion of fly ash based GPC concrete was greater in saline environments with long-term exposure. To understand the potential detrimental effect of chloride ions on the microstructure of the concrete, SEM morphology analysis was carried out on the samples collected from various depths in the core specimens.

Chloride penetration depth

Chloride penetration depth was measured by spraying silver nitrate ($AgNO_3$) solution on freshly split core samples from the leg part of the culverts. As shown in Figure 33, chloride ions completely penetrated the entire depth of the GPC concrete culvert, whereas the ingress of chloride ion in the OPC concrete was only 10 mm and 20 mm from the outer and inner surface, respectively. This is consistent with the results of chloride profile measurements and SEM/EDX analysis. According to the SEM/EDX investigation, chloride ions were identified in all specimens extracted from outer, middle and inner parts of the GPC concrete, while chloride ion was only observed in OPC samples extracted from outer and inner part and not the middle layer.

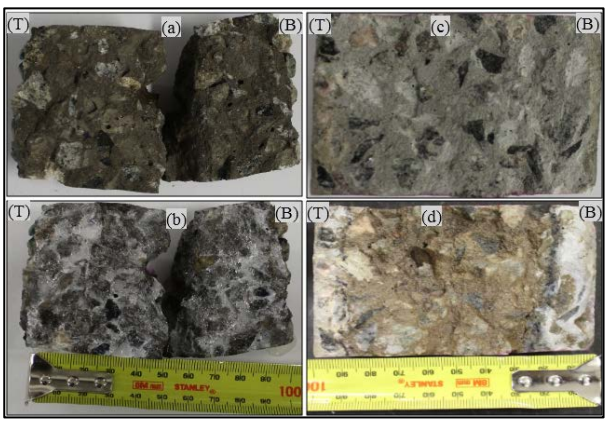

Figure 33. Chloride penetration depth measurements of core specimens using a $AgNO_3$ solution (a) GPC specimen before applying $AgNO_3$, (b) GPC specimen after applying $AgNO_3$, (c) OPC specimen before applying $AgNO_3$, (d) OPC specimen after applying $AgNO_3$.

Capillary sorptivity test

Figure 34 depicts the sorptivity curves of the concrete core specimens to compare the sorption of concrete surface with chloride diffusion values. In a tidal environment, capillary absorption is an important mechanism for the ingress of chloride into the concrete structures. As illustrated, the reduction of sorptivity in OPC concrete is an agreement with well refined and lower pore structures that are related to lower chloride penetration. By contrast, the higher sorptivity of GPC concrete is related to a higher porosity, which are associated with the higher chloride penetration in the GPC compared to OPC concrete.

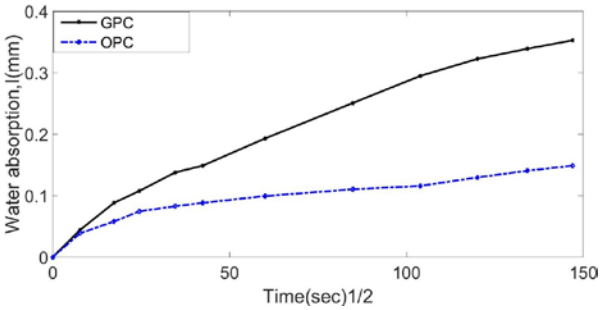

Figure 34. Capillary absorption of GPC and OPC concrete.

Microstructural analysis

SEM/EDX analysis

The results of the SEM/EDX analysis of the samples collected from the outer, middle and inner part of GPC and OPC core specimens are given in Figure 35 and Figure 37. As shown in Figure 35, the presence of Cl^- ions was identified in a higher proportion compared to Si and Al components, in all GPC concrete samples (outer, middle, inner), which is observed with the aid of the EDX results. This indicates that the chloride ions completely penetrated the GPC concrete culvert. As shown in Figure 36, the sodium chloride salt was deposited as a film layer on the microstructure of GPC concrete and this was confirmed by the EDX spectra. However, this was not detected in the SEM micrograph of OPC concrete. The SEM/EDX spectra of OPC concrete (Figure 37) revealed the presence of Cl^- ions in outer and inner part samples, in a lower proportion compared to Ca ions and Cl^- was not identified in the middle part of the sample. Again, this is consistent with the chloride penetration depth results.

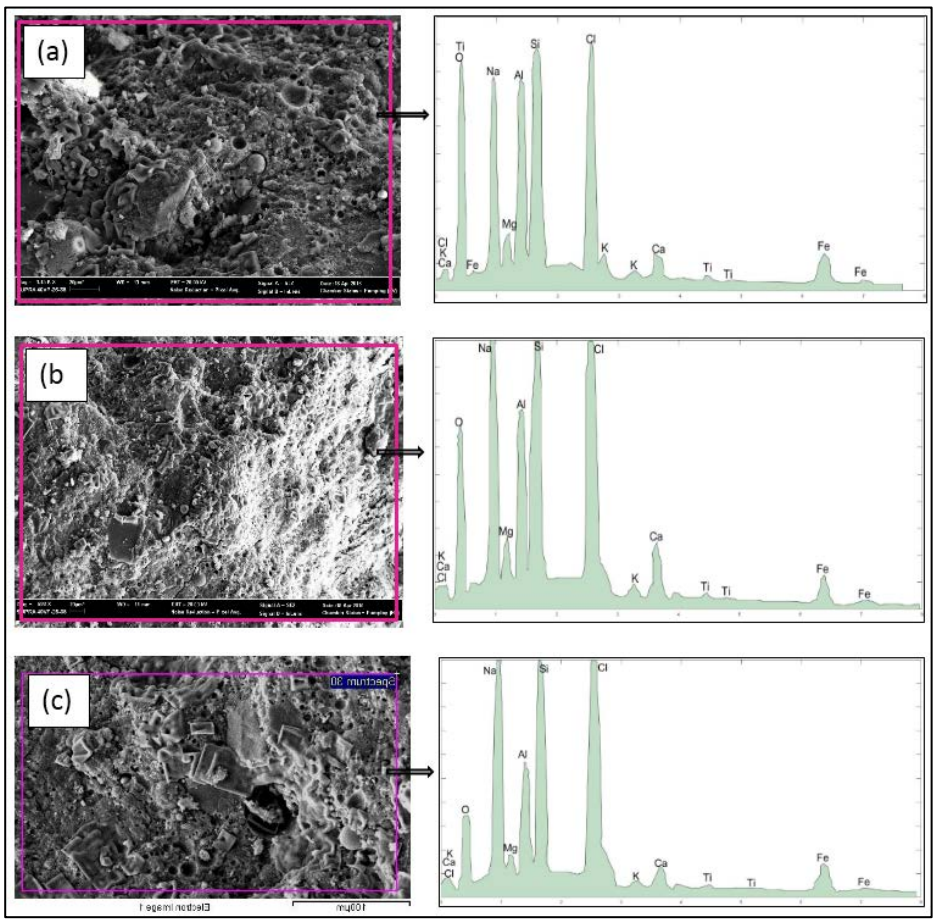

Figure 35. SEM micrograph of (a) Top, (b) Middle and (c) Bottom part of GPC concrete core specimens with corresponding EDX.

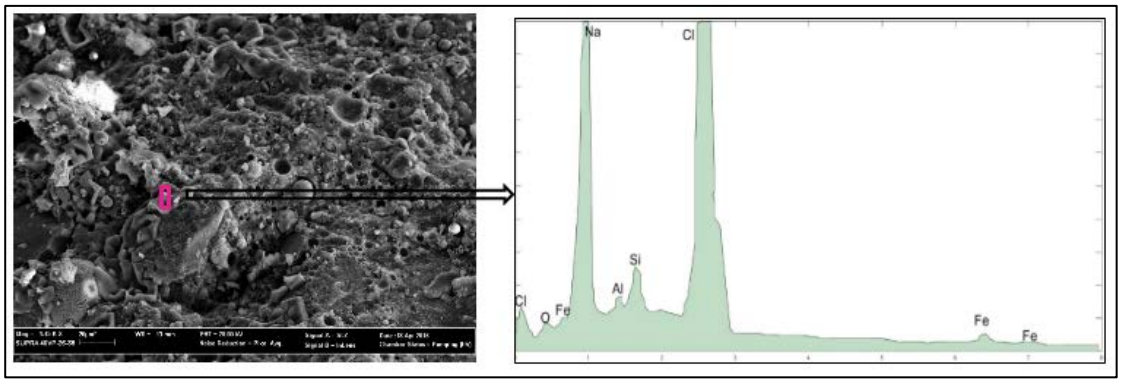

Figure 36. SEM micrograph of chloride deposit on GPC concrete specimens with corresponding EDX analysis.

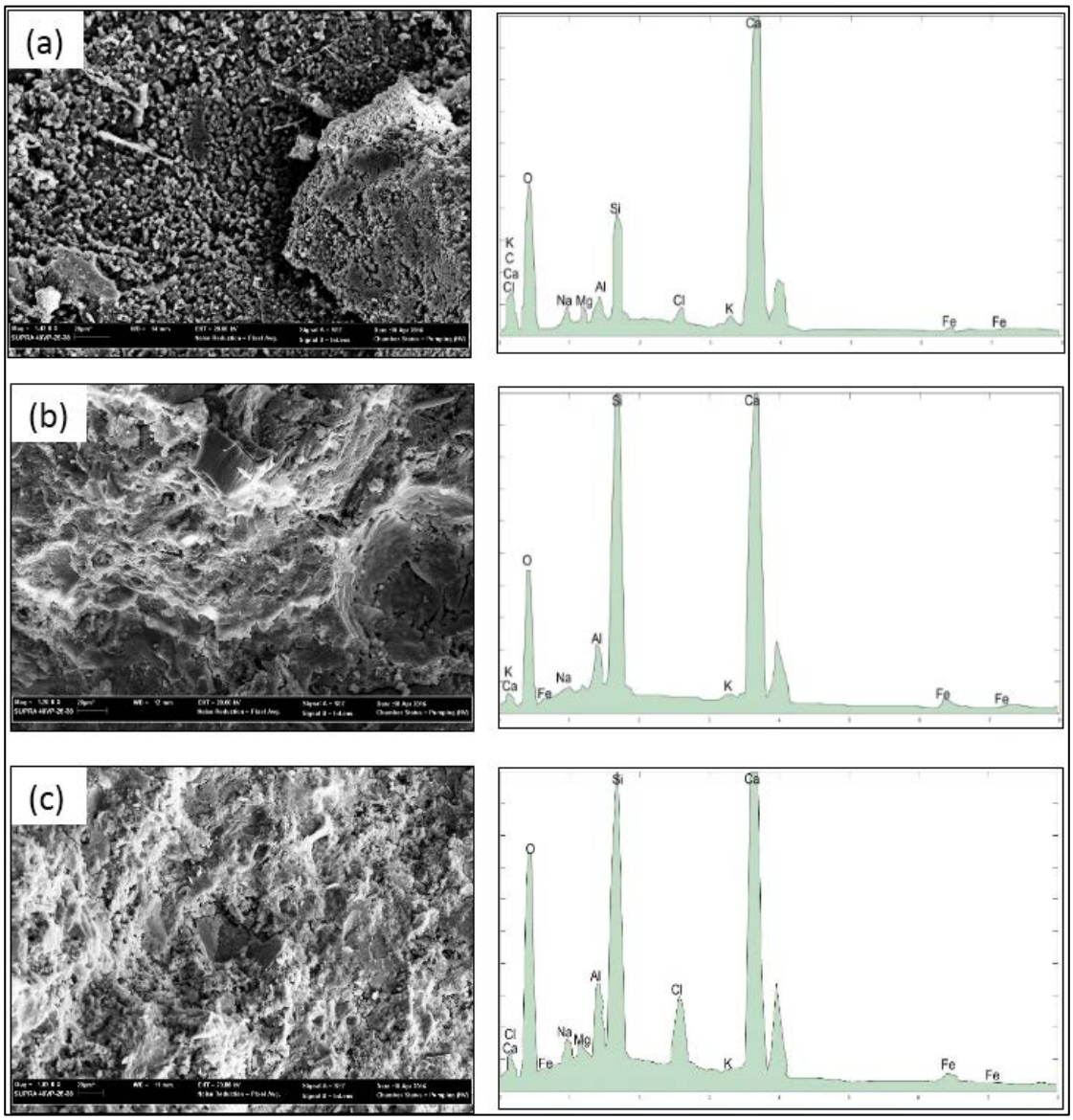

Figure 37. SEM micrograph of (a) top, (b) middle and (c) bottom part of OPC concrete core specimens with corresponding EDX analysis.

Figure 38 depicts the SEM micrograph of GPC and OPC concrete specimens obtained from the outer surface of cored specimens. The ettringite formation was identified in the morphology of OPC concrete provided in Figure 38(b) and there is no evidence for the existence of ettringite in GPC specimens (Figure 38(a)). The exposed soil is rich in magnesium sulphate ($MgSO_4$). In OPC concrete, the ingress of $MgSO_4$ reacts with $Ca(OH)_2$ and calcium aluminate hydrate components and this produced the ettringite component. By contrast, in GPC concrete, ettringite should not be formed due to the absence of those components. However, the EDX results (Figure 35) of GPC revealed that the GPC concrete had a higher level of Mg ions compared to OPC concrete. Therefore, this indicates that the mechanism of sulphate attack in GPC is different than OPC concrete and this requires further investigation.

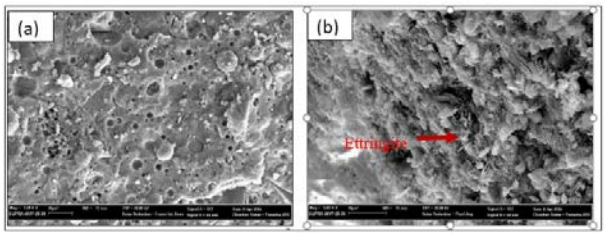

Figure 38 SEM micrograph of (a) GPC, (b) OPC concrete specimens.

XRD analysis

Figure 39 shows the XRD patterns for GPC and OPC concrete samples at the outer surface of the culvert structures. Since sand existed in both samples, the numerous peaks of crystalline phases such as Quartz (SiO_2) and Mullite ($Al_6Si_2O_{13}$,) were identified in all samples. As such, it was difficult to determine the main reaction components from geopolymerisation and the hydration process in GPC and OPC samples as well as the formation of new structures from the degradation of concrete in the saline environment. From the XRD test results of OPC concrete, vaterite and calcite were found to be the main polymorphs of $CaCO_3$. In contrast, no carbonation components were identified in GPC samples and this is associated with the FT-IR spectra. Furthermore, the geopolymerisation reaction components, including $Na(AlSi_3O_8)$ and $Na_2Si_2O_8$ were identified in GPC concrete and $Ca(OH)_2$ and calcium silicate hydrate (C-S-H) components were observed in the XRD results for OPC concrete. However, Cl^- was not detected by XRD analysis for both GPC and OPC concrete due to the interference of other components.

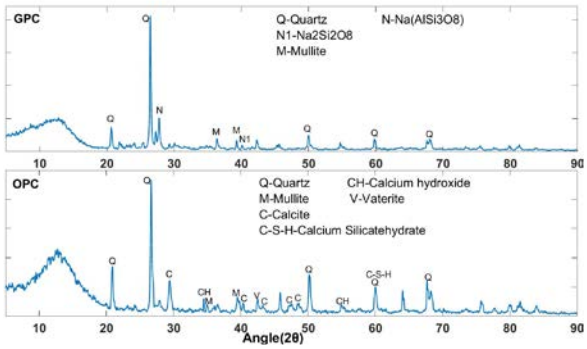

Figure 39. XRD analysis of GPC and OPC specimens at 0-5mm intervals from outer surface.

Evaluation of steel/concrete interface

Visual inspection

Figure 40 illustrates the interface and the reinforcement bars in the GPC and OPC concrete specimens. Figure 40 (a) and Figure 40 (d) show the steel/concrete interface of the leg part of GPC and OPC culverts with a 45 mm cover value. Figure 40 (b) and Figure 40 (e) show the conditions of the steel bars at the same location of the GPC and OPC specimens, respectively. Figure 40 (c) and Figure 40 (f) show the photo of the steel bar with a cover value of 30 mm from the inner surface of the top slab of GPC and OPC structures, respectively. The bars in GPC concrete displayed corrosion products, whereas little visible signs of corrosion products were observed in the bars in the OPC concrete. The reinforcement bar in GPC concrete was corroded over the entire surface and more corrosion products were deposited at the steel/concrete interface compared to OPC concrete. The combination of higher chloride ingress and carbonation accelerated the de-passivation of steel and resulted in more extensive corrosion in GPC concrete compared to OPC concrete.

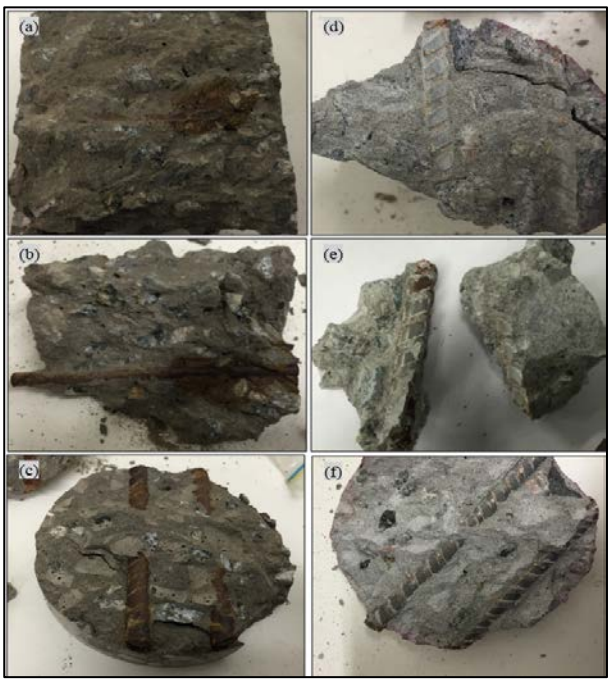

Figure 40. Rebar interface and reinforcement bar after 6 years of exposure, (a) typical rebar interface of GPC concrete specimen, (b) reinforcement bar in leg part of GPC culvert, (c) reinforcement bar in top slab of GPC culvert (d) typical rebar interface of OPC concrete specimen, (e) reinforcement bar in the leg part of OPC culvert, (f) reinforcement bar in the top slab of OPC culvert.

SEM analysis of the interface area

An SEM/EDX analysis was conducted on samples collected at the reinforcement bar/binder interface to determine the micro structural characteristics. Figure 41 shows the SEM micrograph of GPC and OPC concrete specimens collected at the steel/concrete interface area. As shown in Figure 41, the form of flowery structures indicated the presence of lepidocrocite [γ-FeO(OH)] at the interface area of both concretes [43]. An EDX analysis of GPC concrete showed strong peaks of Fe and O and confirmed the presence of corrosion products such as γ-FeO(OH) at the interface area, whereas EDX test results of OPC concrete revealed intermediate peaks of Fe and O, which represents the fewer corrosion products at OPC steel/concrete interface. These results are similar to visual observations of the interfacial area.

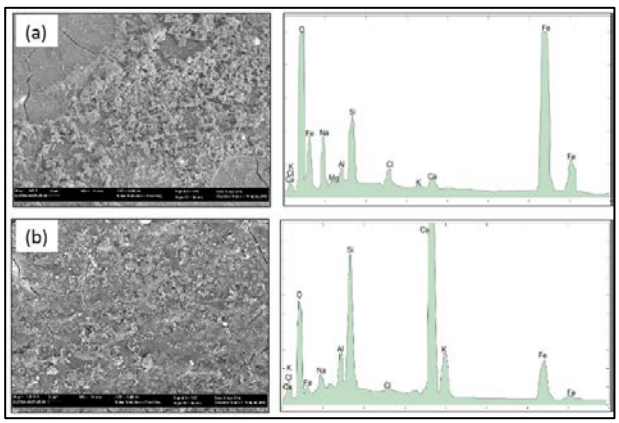

Figure 41. SEM micrograph of (a) GPC; (b) OPC at the rebar/matrix interface with corresponding EDX analysis.

Pore size distribution

Table 9 shows the pore distributions of the concrete specimens, categorized based on the IUPAC classification system. According to that, the GPC contains fines pores and the majority of pores have a diameter between 1.25 nm-25 nm. By contrast, OPC concrete displayed a range of pore diameters with a substantial percentage of pores detected in the range of macro pores and Air voids/cracks range. This indicates that, the average pore size in OPC concrete was greater than the average pore size of GPC. This would be due to the ingress of salt in the saline environment. Higher ingress of salt in GPC fill more pores and reduce the pore size compared to the pore structure changes in OPC concrete. This has been confirmed with SEM/EDX test results, indicates the chloride ions was deposited as a film layer on the GPC surface. However, the MIP results shows the total porosity of the GPC specimens are slightly higher than the porosity of the OPC concrete specimens.

Conclusions

This study investigated the durability of fly ash based Geopolymer concrete exposed to a saline lake environment for 6 years. Based on the experimental results, the following conclusions can be drawn:

1. The salt scaling effect in GPC culvert was higher than OPC concrete culvert. The mortar from the GPC surface, especially from the leg part of culvert that is frequently in contact with saline lake water, has been lost and the aggregate is clearly exposed on the surface, whereas no significant changes has been identified in the visual appearance of OPC concrete culvert over time.
2. The action of leaching due to exposure to running saline water combined with carbonation during dry cycles is found to be more aggressive in GPC than in OPC. This result was obtained after 6 years of exposure.
3. The test results of FT-IR and XRD analysis confirmed the dissolution of carbonation products in fly ash based GPC when it is exposed to field conditions, whereas CaCO3 components were detected in the OPC concrete specimens.
4. The chloride penetration in the GPC concrete was high in saline environments. According to the total chloride analysis, the surface chloride content and the chloride diffusion coefficient of GPC concrete was approximately 2.5 times greater than the values obtained for OPC concrete. Besides, SEM analysis revealed that the chloride contents were deposited as a film layer on the GPC concrete.
5. The GPC culvert displayed higher ingress of sulphate compared to OPC concrete. This produced more scaling effect in GPC structure. SEM/EDX test results also revealed the higher sulphate penetration and there is no formation of ettringite observed in GPC specimens. This indicates, the mechanism of sulphate attack in GPC is different from OPC concrete.

Table 9 Pore size percentages (based on IUPAC classification)

Specimens	Porosity	Pore size distribution (%)			
		Micropores(< 1.25nm)	Mesopores (1.25–25 nm)	Macropores (25–5000 nm)	Air voids/cracks (5000–50,000 nm)
GPC	12.6%	-	62%	19.3%	18.9%
OPC	9.5%	-	12.3%	48.4%	39.2%

6. The combination of higher carbonation and chloride penetration produced higher corrosion activity of the steel bar in GPC. The reinforcement bar in GPC concrete was corroded on the entire surface and the deposition of corrosion products at the interface area of GPC concrete was much greater than for OPC concrete.
7. Although the total porosity of GPC was higher than OPC concrete, the majority of the pores are fines pores. Specifically, GPC has more pores between 1.25 nm-25 nm diameters, whereas the most of the pores identified in OPC concrete in the range between 25-50,000 nm.
8. Finally, this study shows that the Geopolymer concrete prepared with the activation of low Ca fly ash based GPC concrete by the NaOH and Na2SiO3 activators has lower resistance to combined carbonation, chloride and sulphate ingress in the aggressive saline environment. It should be noted that exposure to moving water is particularly deleterious to Geopolymer as it appears to be more susceptible to leaching in such exposure conditions. Therefore, investigation of suitable Geopolymer concrete mix design is required to enhance the durability in aggressive environment.

Perth, Western Australia (SUT)

Introduction

Geopolymer and OPC concrete box culverts that had been stored in the precasting yard in Perth for 8 years were investigated. The AS 3600 exposure classification for the site is B1. The culverts were cast using a fly ash based geopolymer mix design supplied by Curtin University.

The culverts are shown in Figures 42 to 44. In-situ testing of the culverts included resistivity measurements. Core samples were extracted and subjected to the following tests:

- Visual condition, including any corrosion of reinforcement
- Carbonation measurement
- pH profile
- Chloride concentration profile
- Volume of permeable voids
- Sorptivity
- Microstructure and phase analysis by using SEM, XRD, FTIR and TGA methods

Figure 45 shows a typical GPC core.

Figure 42. Geopolymer concrete culvert at casting yard in Perth, WA, in October 2015.

Figure 43. OPC concrete culvert at casting yard in Perth, WA, in October 2015.

Figure 44. Coring of OPC concrete culvert at casting yard in Perth, WA, in October 2015.

Figure 45. Typical Geopolymer concrete core from culvert at casting yard in Perth, WA, in October 2015.

Test results

Carbonation depth measurements

Carbonation depth and coefficient of carbonation (K)

Figure 46 shows the carbonation depth measurements of the core specimens after extracted from the concrete structures by spraying phenolphthalein solution. The carbonation coefficient (*K*) corresponding to that depth value was estimated by the following empirical relationship:

$$Xc = K\sqrt{t} \quad (2)$$

where *Xc* is the tested carbonation depth (mm), *t* is the exposure period (year), and *K* is the corresponding carbonation coefficient (mm/year$^{0.5}$). This formula is based on the square-root-t-law, which has been used previously by many researchers to determine the carbonation behaviour of concrete [44-46]. According to Figure 46, GPC specimens did not show a clear carbonation depth. As for fly ash based Geopolymer concrete [8-10], after spraying the phenolphthalein, the surface of the GPC concrete specimens turned light pink throughout the entire depth. However, as mentioned by Khan et al. [11], carbonation depth of GPC specimen was divided into 3 categories (Figure 46a). According to that, the GPC specimens had 45 mm of fully carbonated zone and 70 mm partially carbonated zone after 8 years of exposure.

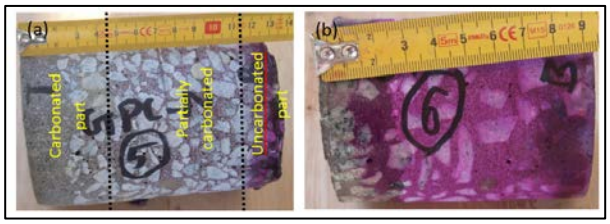

Figure 46. Carbonation depth measurements of core specimens using a phenolphthalein indicator: (a) GPC; (b) OPC concrete.

On the other hand, OPC concrete specimens revealed a good response to the phenolphthalein indicator. OPC concrete specimens revealed that the carbonation depth values were ranging from 4 to 10 mm depending on the location. This is due to the variation in moisture content along with the culvert structure, which affects the diffusion of CO_2 through the concrete. Carbonation coefficients values of OPC concrete calculated with depth measurements were small, in the range of 1.06 to 3.54 mm/year$^{0.5}$, which is comparable with the results obtained in a previous study [4]. Conversely, GPC specimens displays higher coefficient of carbonation, which is about 15.9 mm/year$^{0.5}$.

Carbonation process by FTIR analysis

The IR spectra of the GPC and OPC concrete are shown in Figure 47 and Figure 48, respectively. Figure 47 displays the spectra of GPC samples, obtained up to 30 mm depth level with 5 mm intervals from exposed surface. The IR spectra shown in Figure 48 corresponds to the powder samples collected from OPC concrete specimens up to 15 mm depth with 5 mm intervals. The FT-IR technique is used to identify all saturated (pH < 8.3) and non-saturated (pH > 8.3) carbonation products present in concrete [47, 48]. In FT-IR analyses, the peak of the carbonation characteristics, corresponding to the C-O bond, should be identified at the wave number 1417 cm^{-1} [47, 48]. Figure 47 revealed that the C-O bond was not identified in any spectra corresponding to the GPC concretes sample after 8 years of exposure in atmospheric conditions. However, Na_2CO_3 was observed in laboratory prepared fly ash based GPC samples previously with FT-IR analysis at the wave number 1417 cm^{-1}[49]. This indicates that the carbonation reaction products have been removed from the GPC after 8 years of exposure in the atmospheric environment. This is likely due to washout by rainwater.

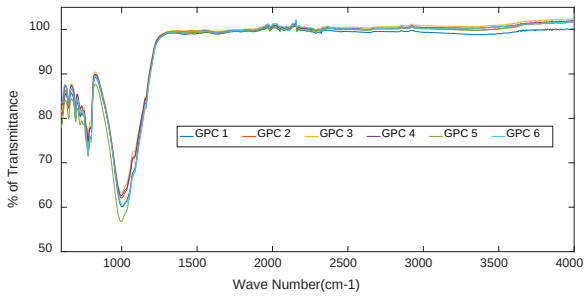

Figure 47. FT-IR spectra for GPC concrete.

In contrast, the IR spectra of OPC concrete revealed the occurrence of a C-O bond at the wave number 1417 cm^{-1}, corresponding to the $CaCO_3$ formation in OPC concrete. The peak taken at the surface of the concrete (0-5 mm) was identified with high intensity, indicating that the carbonation at the surface of the concrete was severe compared to the inner part of the sample. The peak at 899 cm^{-1} relates to the stretching vibration of C-O bond that was found in the first layer of OPC concrete, indicating more carbonation in the first layer compare to other layers. Moreover, the C-O bond was identified in all OPC concrete samples (up to 15 mm depth), whereas a maximum of 10 mm carbonation was identified by the phenolphthalein indicator. The FT-IR technique is a powerful tool to identify all carbonation products at any saturation level. Therefore, the minor $CaCO_3$ content observed here could be identified at 10 and 15 mm depth levels.

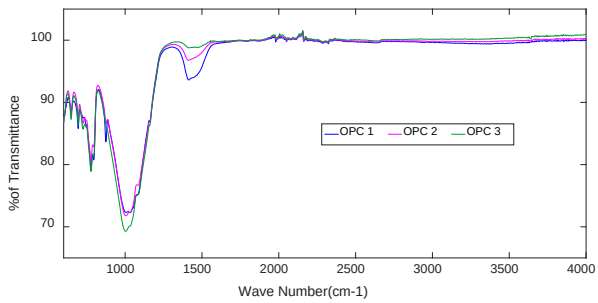

Figure 48. FT-IR spectra for OPC concrete.

A FT-IR spectrum also provides the peaks for a geopolymerisation reaction as well as a hydration reaction in GPC and OPC concrete, respectively. The peak at 997 cm^{-1} in GPC concrete is associated with asymmetric stretching vibration of the Si-O-T (T is Si or Al) bond and the peak detected at 997 cm^{-1} in OPC concrete specimens correspond to the stretching Si-O from the C-S-H phase. Finally, the peaks between 647 cm^{-1} and 777 cm^{-1} are related to the crystalline phase of quartz components.

pH measurements

Figure 49 depicts the pH value variation with depth from the outside exposed surface, measured on the core specimens obtained from the leg part of the culverts. The pH of GPC did not vary significantly with the depth of the samples; the pH range was 9.9 to 10.4 from the exposure surface to 30 mm depth level, whereas the pH of OPC concrete increased from 10.8 to 12.3 from the exposure surface to 30 mm depth. In OPC concrete, the pH of the pore solution is attributed by a combination of $Ca(OH)_2$ and C-S-H gel. In contrast, the pH of GPC is influenced by the activator pH value and the amount of residual activator that remains in Geopolymer binder. Therefore, the pH of the GPC specimen was controlled by the NaOH activator [10]. The pH of Geopolymer concrete is approximately 11.5 [10, 50, 51] and in this work the value was 10.0-10.5, indicating that a pH reduction in GPC concrete has occurred due to the carbonation in atmospheric conditions [50]. While the pH of GPC specimens was maintained above 9.0, the steel bar embedded in the GPC culvert with 45 mm cover depth showed corrosion as discussed in the following section.

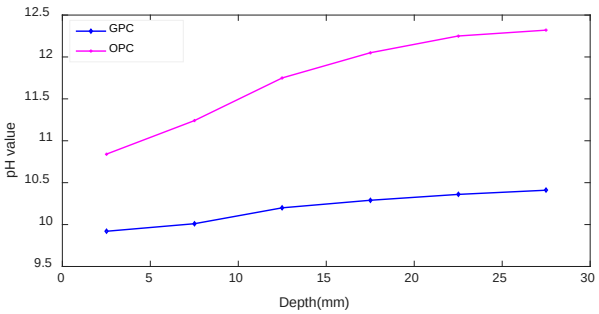

Figure 49. pH variation with depth of concrete from exposed surface.

The carbonation depth of the OPC concrete core specimen as determined from pH measurement was 3 mm and the pH value obtained at 5 mm depth level was 10.8. This indicates that the rate of carbonation in OPC concrete is low and that the sample was partially carbonated and consisted in non-saturated carbonation products including $Ca(OH)_2$ and calcium silicate hydrate [48]. This was confirmed by FT-IR analysis, which showed the C-O bond up to 15 mm.

Condition of reinforcement

In OPC concrete, protection of the reinforcement from the corrosion is provided with alkalinity ($Ca(OH)_2$) component of the cement by forming a thin oxide layer around the reinforcement. This passivation layer will be de-passivated with carbonation process due to alkalinity deduction (pH deduction to less than 9.0) in the concrete. Photos of embedded reinforcement bars which were located in the leg parts of the GPC and OPC concrete culverts with 45 mm cover are provided in Figure 50. The reinforcement bar in GPC displays some superficial corrosion. As no corrosion measurements were taken, and storage was not I a controlled environment, no conclusions are drawn on this observation.

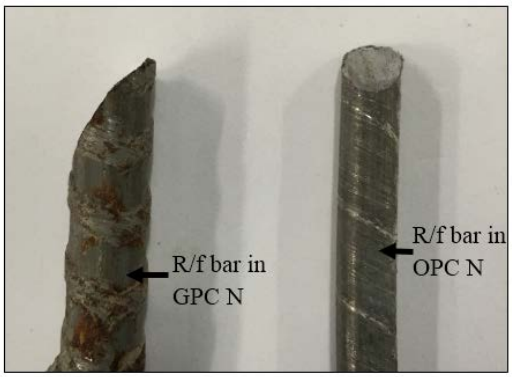

Figure 50. Visual observation of embedded steel bars extracted from GPC and OPC concrete at 8 years exposure (45 mm cover).

Variation of transport properties with age of concrete

Volume of permeable void test results

Table 10 shows the the changes of water absorption and apparent volume of permeable voids (AVPV) values of the concrete samples. The water absorption and AVPV values of the 8-year-old concrete specimens were compared to the concrete properties 28 days after curing. According to that, the variation of water absorption value with the age of concrete was minor for both concretes. The percentage of water absorption varied in the range of 4.90% to 4.97% for the GPC concrete specimens and 5.35% to 5.22% for the OPC concrete. Overall, the concrete specimens exhibited low water absorption values, indicating low porosity.

Table 10 Water absorption and AVPV values

Specimens No	Water absorption (%)	AVPV (%)
GPC 28 days	4.90	11.40
GPC 8 years	4.97	12.27
OPC 28 days	5.35	12.25
OPC 8 years	5.22	12.50

It should be noticed that the effect of aging on AVPV was small with a similar trend observed for water absorption values and the AVPV of GPC specimens. The AVPV of GPC concrete increased from 11.40% to 12.27%, and the AVPV of OPC concrete also slightly increased from 12.25% to 12.50% at 28 days versus 8 years. The OPC concrete with AVPV values less than

13% is classified as good quality concrete [52]. According to these test results, both types of concretes were below this limit at all time, which suggests limited pore interconnectivity.

Sorptivity test results

The results of the sorptivity tests are presented in Figure 51. The notations 'T' and 'M' represent the top and middle part of the core specimens, respectively. The top part of atmospheric exposed GPC specimens (GPC 08 years 'T') had the highest water absorption rate and the top part of atmospheric exposed OPC concrete (OPC 08 years 'T') had the lowest rate. The mid part of 8-year-old GPC specimens display a lower sorption rate, while the mid part of the aged OPC concrete specimens showed a higher rate compared to their top part, indicating that the porosity of the GPC was enhanced when it is exposed to the field environment. However, the OPC concrete specimens at 28 days age display similar sorptivity behaviour for the top and middle section of the specimens. The reduction of water absorption for the top part of atmospheric exposed OPC concrete is the result of carbonation [53]. The pore structure and the interconnectivity of the pore systems of the top surface of OPC concrete change with the formation of $CaCO_3$, a solid densified layer caused by a carbonation reaction. As a result, the water absorption rate of the top part of the OPC concrete sample reduces with the age of the concrete. On the other hand, the porosity increase in atmospheric exposed GPC is attributed to the formation of soluble carbonated products such as sodium carbonate (Na_2CO_3) and potassium carbonate (K_2CO_3), which induce a higher water absorption rate for carbonated GPC concrete samples.

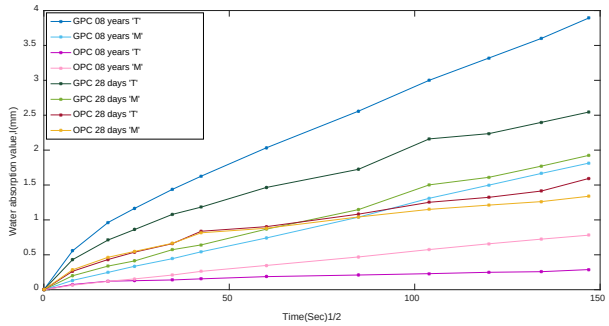

Figure 51. Sorptivity curves of GPC and OPC concretes.

It is important to note that the AVPV values of GPC are very close to that of OPC concrete and that GPC had greater capillary sorption parameters compared to OPC concrete sorption values. Capillary sorption is related to total porosity, tortuosity and the size of the pore network [54], while AVPV is associated with open porosity values. Here, the lower sorptivity coefficient of OPC concrete is associated with the formation of a more densified pore structure, resulting in a more tortuous network and reduced pore size. To further examine the porosity and pore size distribution of both concretes, a Mercury Intrusion Porosimetry (MIP) test was carried out on the concrete samples.

Results of MIP measurements

Figure 52 demonstrates the relationship between the cumulative intrusion (ml/g) and pore diameter (nm) of carbonated and un-carbonated GPC and OPC concrete specimens. The differential pore size distribution of carbonated and un-carbonated specimens is also presented in Figure 52. The main increment of cumulative intrusion of GPC concrete samples occurred in the pore diameter intervals of 20 nm to 160 nm and the OPC concrete specimens also changed at similar intervals (25 nm -170 nm). According to Figure 52, OPC concrete specimens had lower total intrusion compared to GPC concrete, indicating that GPC concrete specimens have higher porosity than OPC concrete samples in both stages, such as before and after carbonation. This may be explained by the formation of porous geopolymerisation reaction products, which is the three dimensional network of N-A-S-H gel by the activation of fly ash.

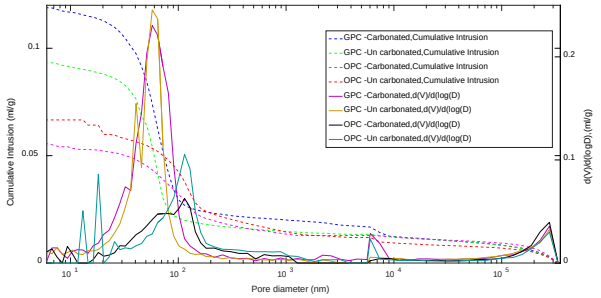

Figure 52 Cumulative intrusion and differential pore size distribution of atmospheric exposed concrete specimens.

It was also shown that the total intrusion in OPC concrete decreases with carbonation, while the total intrusion of GPC concrete increases with carbonation in atmospheric conditions (Figure 52).This is consistent with the corresponding sorptivity test results. Table 11 depicts the total porosity and the proportions of the pores for each category of pore diameters including 0-20 nm, 20-100 nm, 100-200 nm and greater than 200 nm for carbonated and un-carbonated specimens. A pore diameter less than 20 nm is considered "*harmless*" and a pore size between 20 nm and 100 nm is classified as "*minor harmful*" pores. A pore size between 100 nm and 200 nm is defined as "*harmful*" and greater than 200 nm is considered as "serious harmful" pores [55].

According to Table 11 and Figure 52, carbonated GPC concrete showed higher porosity compared to the un-carbonated sample, whereas the porosity of the OPC concrete specimen reduced from 12% to 10.1% with the carbonation reaction in atmospheric exposed condition. The GPC concrete contains fines pores and the majority of pores have a diameter between 20-100 nm. By contrast, OPC concrete displayed a range of pore diameters with a substantial percentage of pores detected in the range of 20-100 nm, 100-200 nm and greater than 200 nm. This indicates that, the average pore size in OPC concrete was greater than the average pore size of GPC concrete.

Table 11. Porosity and pore size distribution of atmospheric exposed concrete specimens.

Specimens	Porosity (%)	Pore diameter (0-20 nm) (%)	Pore diameter (20-100 nm) (%)	Pore diameter (100-200 nm) (%)	Pore diameter (>200 nm) (%)
GPC -Carbonated	20.2	5.1	70.3	5.1	19.4
GPC - Un carbonated	16.1	6.2	72.0	4.0	18.2
OPC -Carbonated	10.1	6.3	36.53	21.8	35.3
OPC - Un carbonated	12.0	10.1	26.7	29.3	33.9

This data illustrates that the percentage of capillary pores (100-200 nm) in GPC concrete increased with carbonation. However, the carbonated OPC concrete contains a lower percentage of capillary pores compared to the un-carbonated OPC concrete specimens. Taken together, this confirms that the porosity of carbonated OPC concrete was reduced by filling pores in OPC concrete with carbonation reaction products. Conversely, carbonation increases the porosity in fly ash based GPC concrete in an atmospheric environment. This was confirmed by the MIP test results obtained from accelerated carbonated GPC concrete specimens. Figure 53 represents the MIP test results of the carbonated samples after 3 months of exposure and control (un-carbonated) GPC concrete samples. The plotted graphs indicate little difference between carbonated and control samples and the total porosity obtained for carbonated and control GPC samples were 15.4% and 14.9%, respectively. This confirms the porosity enhancement of fly ash based GPC concrete in the atmosphere by dissolving carbonated components in water. Moreover, this treatment produces a higher carbonation effect in GPC concrete compared to OPC concrete. The test results from MIP analysis are consistent with the sorptivity test results; while the AVPV test provide contradictory results. As such, both MIP and sorptivity analysis are appropriate methods to determine the pore size distribution of concrete samples.

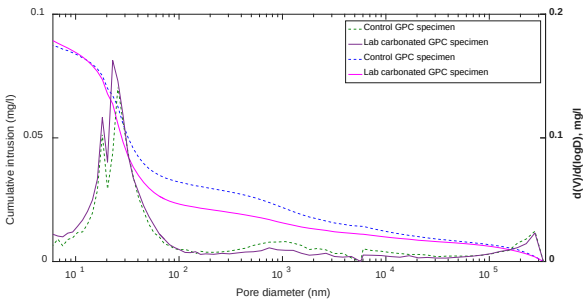

Figure 53. MIP test results for laboratory carbonated fly ash based GPC concrete.

Comparison of carbonation resistance with slag-and fly ash based GPC

The carbonation resistance of fly ash based Geopolymer concrete was compared with the blended slag-fly ash Geopolymer concrete. The study on the carbonation of blended slag-fly ash Geopolymer concrete in atmospheric field conditions after 8 years of exposure has been conducted previously [56]. The carbonation depth values of blended slag-fly ash Geopolymer concrete specimens after eight years of exposure in real field environment were measured as 8.0–27.5 mm; this is smaller than the values obtained for Geopolymer concrete in this study. This indicates that fly ash based Geopolymer concrete has lower resistance to carbonation and the carbonation resistance is improved with the addition of slag content in the Geopolymer mixture. In addition, the porosity test results from MIP analysis and the water absorption value from the sorptivity test measurement of slag-fly ash Geopolymer concrete were 17.63% and 2.4 mm [56], respectively. In contrast, porosity and the maximum water absorption value from the sorptivity test of the GPC specimens were determined as 20.2% and 3.9 mm. Therefore, this confirmed that the durability of the fly ash based GPC concrete is less compared to slag-fly ash Geopolymer concrete.

Conclusions

The durability of precast fly ash based Geopolymer concrete in an atmospheric environment was investigated and compared to OPC concrete. Based on the results, the following conclusions can be drawn:

1. The effect of carbonation was greater in fly ash GPC compared to OPC concrete and the FT-IR spectra revealed the removal of carbonation products in the low Ca fly ash based GPC exposed to field conditions probably due to dissolution in water.
2. The pH of carbonated GPC was higher than 9.0. However, the reinforcement in the GPC was more

prone to corrosion with despite the high pH value; the embedded reinforcement in GPC begun to corrode at pH 10.40. In contrast, corrosion of reinforcement in OPC concrete typically occurs when the pH is less 9.0.

3. According to the sorptivity test results, the sorptivity characteristic of GPC increases with the age of the concrete, while the sorptivity of OPC concrete reduces with age. This suggests that the pore structure of the outdoor exposed GPC surface changes with age and this was verified by the MIP porosimetry test results.
4. The MIP test results confirm the porosity increase with carbonation in field conditions. The carbonated part of field exposed GPC sample shows higher porosity than un-carbonated GPC sample, whereas the GPC specimens, that was from the accelerated carbonation test displays similar porosity compared to un-carbonated GPC sample. On the other hand, field exposed OPC concrete had lower porosity compared to un-carbonated OPC samples.
5. Therefore, this study shows that the carbonation resistance in atmospheric environment of fly ash based GPC concrete used here is lower compared to OPC concrete.

Portland, Victoria (SUT)

Introduction

Cores were sampled from concrete blocks (Figures 54 to 56) exposed to marine environment. Analysis carried out aimed to compare the performance against chloride penetration of GPC to that of OPC reference concrete.

Figure 54. GPC and OPC concrete blocks in Portland, Victoria, in June 2016.

Figure 55. Coring of GPC block at Portland, Victoria, in June 2016.

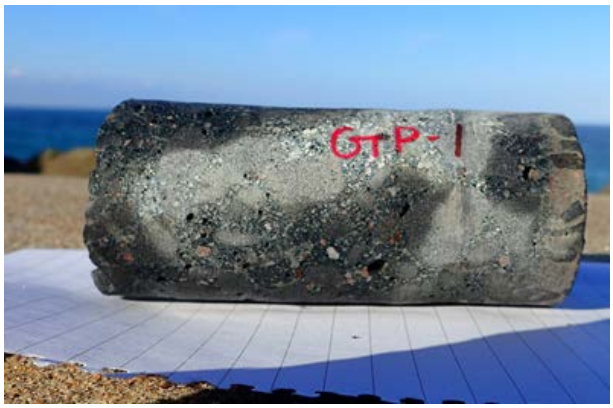

Figure 56. Typical Geopolymer concrete core from block at Portland, Victoria, in June 2016.

Test results

Alkalinity reduction in marine environment

In OPC alkalinity reduction is normally associated with carbonation of concrete. In GPC it appears that leaching of alkalinity when exposed to moving water is also a major issue and leads to a reduction in alkalinity. Thus the phenolphthalein test, normally used in OPC to measure carbonation, measures both carbonation and leaching effects, particularly in the splash zone of marine environments where leaching problem is exacerbated. Further, it should be noted that in tidal/splash zone the carbonation is generally low as the concrete is quasi-saturated limiting the penetration of carbon dioxide.

Reduction in alkalinity (either by carbonation or leaching) is an important phenomenon for the degradation of durability of concrete structures in the field conditions. Figure 57 shows the phenolphthalein test measurement of core specimens; the variation of depth values with different exposure periods are presented in Figure 58.

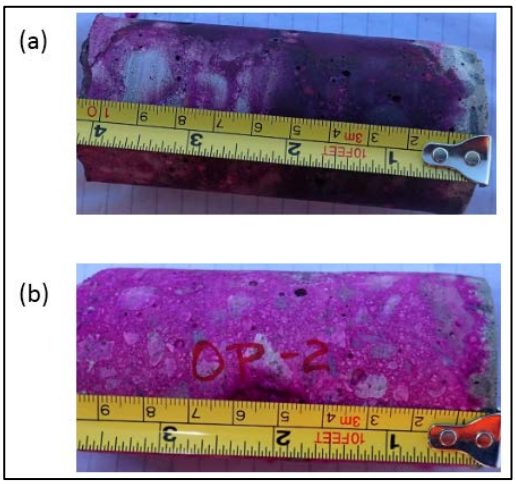

Figure 57. Carbonation depth measurements core specimens by phenolphthalein solution: (a) GPC core specimen; (b) OPC concrete core specimen.

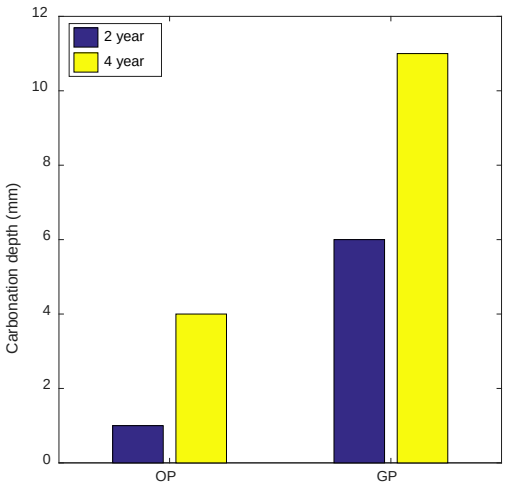

Figure 58. Carbonation depth values after 2 years and 4 years of exposure.

Compared to OPC concrete, GPC concrete showed higher loss of alkalinity after 2 years and 4 years of exposure in marine conditions. The GPC had 6 mm depth, while OP concrete revealed only 1 mm depth after 2 years of exposure.

In the marine atmosphere, the rate of alkalinity loss is lower than that of concrete in normal atmospheric environment due to the frequent contact of water. It has been reported in the previous study that the carbonation depth of OPC concrete in the atmospheric zone can reach 4 to 7 mm after 4 years of exposure [57]. In this investigation, the OPC concrete displays alkalinity loss at 4 mm depth after 4 year of exposure, which is similar to previous results. On the other hand, the GPC specimen displayed a value of about 11 mm after 4 years of exposure.

It is widely known that the pH of the OPC concrete is decreased with the carbonation reaction due to the formation of calcium carbonate ($CaCO_3$) from the reaction between calcium hydroxide ($Ca(OH)_2$) and carbon di oxide (CO_2). Figure 59 shows the pH variation with the depth of the concrete specimens after 4 years of exposure. The pH of the OPC concrete dropped from 12.3 to 9.0 with the carbonation reaction (4 mm depth), while the pH of carbonated GPC concrete is in the range of 8.5 to 10.0. In OPC concrete, pH reduction is due the formation of $CaCO_3$. However, a lower amount of $CaCO_3$ formation is expected in slag based Geopolymer concrete due to lower Ca content compared to OPC [58] and the formation of Na based carbonation components as a results of the reaction between NaOH and CO_2 is leading to a higher pH in carbonated Geopolymer concrete. In addition, it should be noted that from the test results, the pH value of un-carbonated Geopolymer concrete (11.5) is lower than the pH of un-carbonated OPC concrete, and the similar behaviour has been identified in the previous studies.

Furthermore, it should be noted that the pore structure of the concrete is influenced by the CO2 diffusion through the surface. Therefore, Mercury Intrusion Porosimetry (MIP) analysis was carried out to determine the pore size and pore network of the concrete specimens.

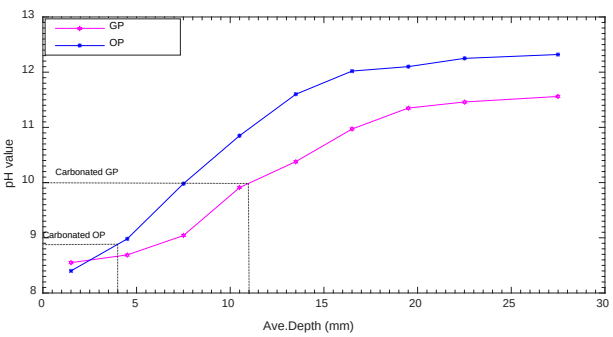

Figure 59. pH variation with depth of the concrete from the exposed surface.

Chloride diffusion coefficient of concrete

The chloride diffusion coefficient is used to compute the resistance of chloride ion penetration through the concrete structure [59]. In this study, the chloride diffusion coefficient of a concrete (D_c in mm^2/year) was calculated using the Fick's second law of diffusion equation [35, 60]. According to that the relationship between chloride content of concrete ($C_{x,t}a$), and the depth from the exposed surface (x) can be written as:

$$C_{x,t}a = C_s\left(1 - erf\left(\frac{x}{4\,D_c \times t}\right)\right) \quad (3)$$

where $C_{x,t}$ is the total chloride concentration (% by weight of concrete) at the position x and exposure time t; x is the distance from concrete surface (mm); t is the exposure time (seconds); C_s is the chloride concentration at concrete surface (% by weight of concrete) at exposure time t; D_c is the chloride penetration coefficient (mm^2/s) at exposure time t and *erf* is the error function. The value of D_c is determined from the chloride penetration profile of specimens obtained from concrete structures exposed in the field environment.

Figure 60 shows the total chloride profiles of GPC and OPC concrete core specimens after exposed to marine environment for 4 years and Table 12 illustrates the calculated chloride diffusion coefficients and the surface chloride concentration values (Co) after the exposure of 2 years and 4 years of periods. The chloride profile and the results of chloride diffusion coefficient and surface chloride concentration show that the GPC specimen had lower resistance to chloride transportation compared to OPC concrete.

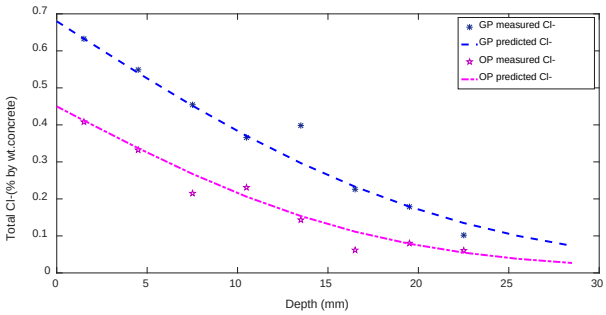

Figure 60. Chloride profiles of concrete after 4 years of exposure in marine environment.

Table 12. Chloride diffusion coefficient and surface chloride content of concrete.

	Chloride Diffusion Coefficient, D_c (1×10^{-12} m^{2}s^{-1})		Surface Chloride Concentration, C_o (% by weight concrete)	
	2 years	4 years	2 years	4 years
GP concrete	1.92	1.15	0.651	0.68
OPC concrete	N/A	0.45	N/A	0.45

Previous studies has shown that the chloride resistance of slag-based Geopolymer concrete is greater than OPC concrete [18, 33]. The slag based Geopolymer concrete produces cross-linked C-A-S-H (tobermorite) phase which is high density compare to OPC concrete due to the formation of non-cross linked C-S-H (tobermorite) [61]. Therefore, the Geopolymer containing higher slag content have lower porosity and less pore volume [33], which represents the lower chloride penetration compared to OPC concrete. However, this study shows higher chloride diffusion in GPC compared to OPC concrete after 4 years of exposure in the marine conditions. It should be noted that the ingress of chloride ions to the OPC concrete reduces with age of concrete due to continuous hydration reaction in OPC concrete with time. However, the geopolymerisation reaction is quicker than the hydration of OPC concrete [10] and this would produces higher chloride transportation in GPC specimens after the 4 years of exposure period.

Table 12 shows that the D_c and C_o values of the GPC specimens are reduced with the exposure period. The diffusion coefficient of GP concretes was 1.92×10^{-12} and 1.15×10^{-12} m²/s at 2 years and 4 years of exposed time, respectively. These values are higher than the value observed by Ismail et.al [62] for high slag based Geopolymer concrete with accelerated testing methods. Since there are no diffusion coefficients and the surface chloride values are calculated for OPC concrete after one year of exposure, the variation of D_c and C_o values of OPC concrete could not be achieved.

Chloride binding capacity of concrete

The chloride binding capacity in concrete was calculated using the values of free chloride and total chloride content. Eq. (4) was used to determine the chloride binding capacity of both concretes [60, 63]:

$$P_{bc} = \frac{Ct - Cf}{Ct} * 100\% \quad (4)$$

where P_{bc} is the chloride binding capacity, Ct is the total chloride content and Cf is the free chloride content in the concrete. Accordingly the chloride binding capacity of the GPC and OPC concrete specimens are 34% and 46%, respectively.

There are two mechanisms, in general, that influence the chloride binding capacity of concrete; they are physical adsorption and chemical reactions [64]. The chloride binding capacity of concrete increases with the C_3A content as the C_3A component in the cement binder reacts with bound chloride and produced calcium chloroaluminate hydrate ($3CaO{\cdot}Al_2O_3{\cdot}CaCl_2{\cdot}10H_2O$), which is known as Friedel's salt [65]. This enhances the chemical binding of chloride. On the other hand, the chloride ions are physically bounded with the C-S-H gel in the hydration products and the ettringite components. However, in slag based Geopolymer concrete, the chloride ion is bound by C-A-S-H gel [33] and C-S-H gel. According to the test results, GPC specimen had less binding capacity compared to OPC concrete and therefore this indicates more chloride ions bound with the OPC concrete phases compared to the GPC reaction components.

Capillary water absorption

Sorptivity curves of the GPC and OPC concrete samples are shown in Figure 60. The sorptivity parameters represent the ability of water absorption of the concrete surface by the capillary suction and it is related to the pore structure and interconnectivity of pores [33].

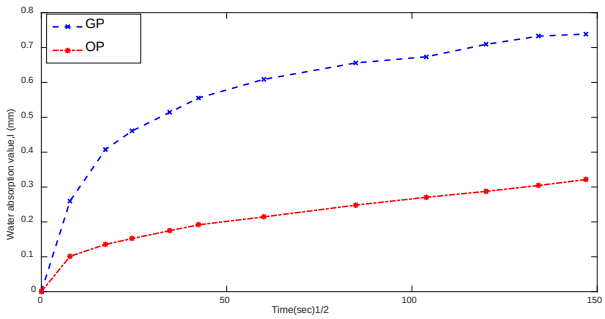

Figure 61. Test results from sorptivity analysis.

The rate of water absorption can be calculated by two stages such as initial water absorption rate and secondary water absorption rate. However, the initial water absorption rate is associated with the capillary pores in the concrete surface and that is associated to the chloride transportation into the concrete. The initial rate of water absorption or the sorptivity coefficient of GPC and OPC concrete samples are given in Table 13.

Table 13. Coefficients of sorptivity values.

Specimens	Initial sorptivity coefficient(mm/s$^{1/2}$)
GPC	0.0101
OPC	0.0016

As shown in Figure 61 and Table 13, capillary absorption of GPC specimens is high compared to OPC concrete specimen. This is similar to the experimental test results of chloride diffusion and carbonation. It can therefore be concluded that the sorptivity test is an appropriate test to assess Geopolymer concrete performance for carbonation and chloride penetration.

Furthermore, capillary sorption parameter is related to the total porosity and the tortuosity of the concrete pore structure [33]. Therefore, this test results indicates that OPC concrete had a dense and lesser porous network compare to GPC specimen. The mercury intrusion porosimetry (MIP) test, however, provides a better understanding of the pore structure and pore size distribution of concrete and, thus, was conducted on the concrete specimens.

Mercury intrusion porosimetry (MIP) test

Figure 61 shows the cumulative pore size distribution of both types of concrete samples from 0-3 mm (top-level) and 25-30 (mid-level) mm depth levels. The total volume of intruded mercury for GPC concrete specimens is higher than that of the OPC concrete specimens. The GPC specimens had 0.085 ml/g for 0-3 mm depth level and 0.081 ml/g of cumulative pore volumes for the

sample from 25-30 mm, whereas OPC concrete showed the of cumulative intrusion volumes are 0.048 and 0.055 ml/g for the samples from 0-3 mm and 25-30 mm depth levels, respectively. Figure 63 shows the differential pore size distribution and Table 14 displays the overall pore characteristic details of both types of concrete specimens at the depth level of 0-3 mm and 25-30 mm. According to that, the total porosity of top level of GPC specimen is higher than the sample from mid-level, whereas, top level OPC concrete specimen had lower porosity compared to mid-level of OPC concrete. This indicates, the carbonation reaction in OPC concrete reduces the porosity of the surface, whereas no such effect occurred in Geopolymer concrete surface. In OPC concrete, formation of $CaCO_3$ fills the pore structure and reduces the pore sizes of the concrete surface. Although $CaCO_3$ is the primary carbonation products in slag based GPC, the amount of Ca in slag is lower compared to that of OPC. As a result, the deposition of $CaCO_3$ is lower than in OPC concrete [58]. Therefore, the amounts of CaCO3 components in slag-based Geopolymer concrete are not enough to fill the pores and reduce the pore size concrete surface. As a result, porosity of the top level of the GPC sample has not been reduced with the carbonation reaction.

Although the GPC specimens had higher porosity, they possess similar or lesser average pore diameter values compared to the OPC concrete specimens. Figure 62 shows the differential pore size distributions of both types of concrete. As per that, both type of concrete specimens had a larger proportion of pores with diameter less than 50 nm, which are harmless or less harmful pores [22]. However, some noticeable amount of harmful pores with diameter ranging from 50 to 100 nm were identified close to the surface of GPC concrete specimens (0-3 mm), which can explain the higher CO_2 and Cl- penetration observed in GPC concrete.

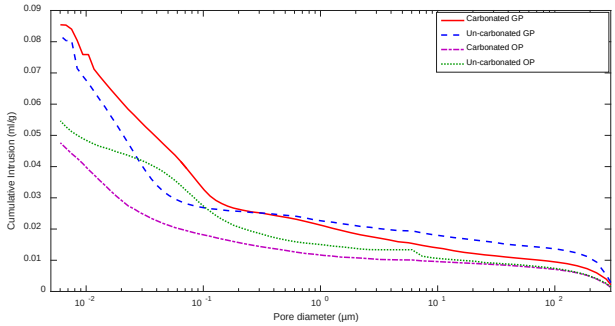

Figure 62 Cumulative pore size distribution obtained for both types of concrete at the surface level and the mid depth level.

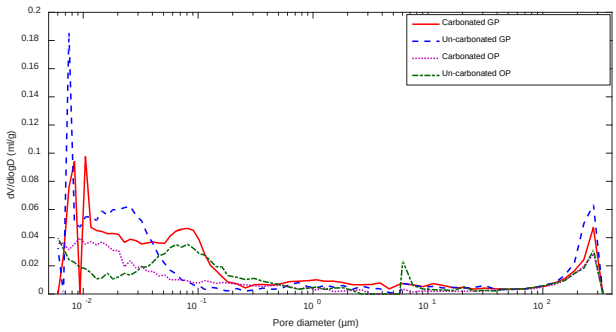

Figure 63. Differential pore size distribution obtained for both types of concrete at the surface level and the mid depth level.

Table 14. The pore characteristics details of both types of concrete specimens.

	GPC (0-3 mm)	GPC (25-30 mm)	OPC (0-3 mm)	OPC (25-30 mm)
Porosity (%)	14.5	14.2	8.7	9.9
Ave.pore diameter (nm)	28.3	21.9	22.3	34.8
Total pore area(m^2/g)	12.09	14.97	8.52	6.27

Conclusions

Based on the experimental results obtained in this study, it may be concluded that slag based Geopolymer concrete is less durable as OPC concrete. The following conclusions are made:

1. Loss of alkalinity (due to either carbonation and/or leaching) is higher in the slag based Geopolymer used, and tested, in the aggressive leaching (marine) environment of this study.
2. During 4-year exposure in a marine environment, the chloride penetration of slag-based Geopolymer concrete was found to be higher than OPC concrete. Geopolymer concrete displayed higher chloride diffusion and lower chloride binding capacity compared to Portland cement concrete.
3. The test results from sorptivity analysis showed that the capillary water absorption parameters are strongly related to the CO_2 and chloride diffusions. According to the test results, higher sorptivity coefficient identified in Geopolymer concrete, whereas OPC concrete displayed lower sorptivity coefficient value.
4. The MIP analysis illustrates the relationship between the porosity and the penetration of aggressive agents. Specifically, the test results revealed that the Geopolymer concrete had a higher porosity and a higher total pore area than OPC concrete. This correlates well with the experimental results obtained from carbonation and chloride penetration tests.

Long-term Performance Monitoring of Geopolymer Concrete Structures

Wellcamp Business Park entry bridge project, Toowoomba, Queensland (UNSW)

The performance of a Geopolymer concrete bridge in Queensland has been monitored since September 2014. The two-way bridge, located on International Drive near the junction of Cecil Plains Road, and about 140 km from the coast, was constructed by Wagners in 2014 as the entry to the Wellcamp Business Park in Toowoomba, Queensland. The structure comprises of two bridges, each acting as a one-way passageway. Figure 64a shows the bridge near completion at September 2014 and Figure 64b as it is in August 2017.

Design and construction of the bridge

The design of the bridge incorporated Wagners EFC (Earth Friendly Concrete) to form the vehicular pavement top deck to sit on top of Wagners FRP (Fibre Reinforced Polymer) composite element girders that provide the bridge with structural support as they span the length of the assembly.

Figure 65 shows the dimensions of the west side of the bridge structure. Due to the bridge being symmetrical, the east side is exactly the same as the west, where they are separated by a 7.04 metre gap. It is seen that the Toowoomba Cecil Plains Road side (entrance) of each bridge section has a width of 13.1 metres while the Wellcamp Business Park side has a width of 11.88 metres with both sections having a 3.4 metre wide footpath. The length of the bridge spans a distance of 11.5 metres while the Geopolymer concrete deck has a thickness of 200 mm with 50 mm asphalt on top acting as the road surface material.

(a)

(b)

(c)

Figure 64. (a) Geopolymer concrete bridge at Wellcamp airport business park precinct, Toowoomba Queensland: (a) nearing completion at in in September 2014 (photo courtesy of Wagners); (b)-(c) completed bridge and road development (photo taken August 2017).

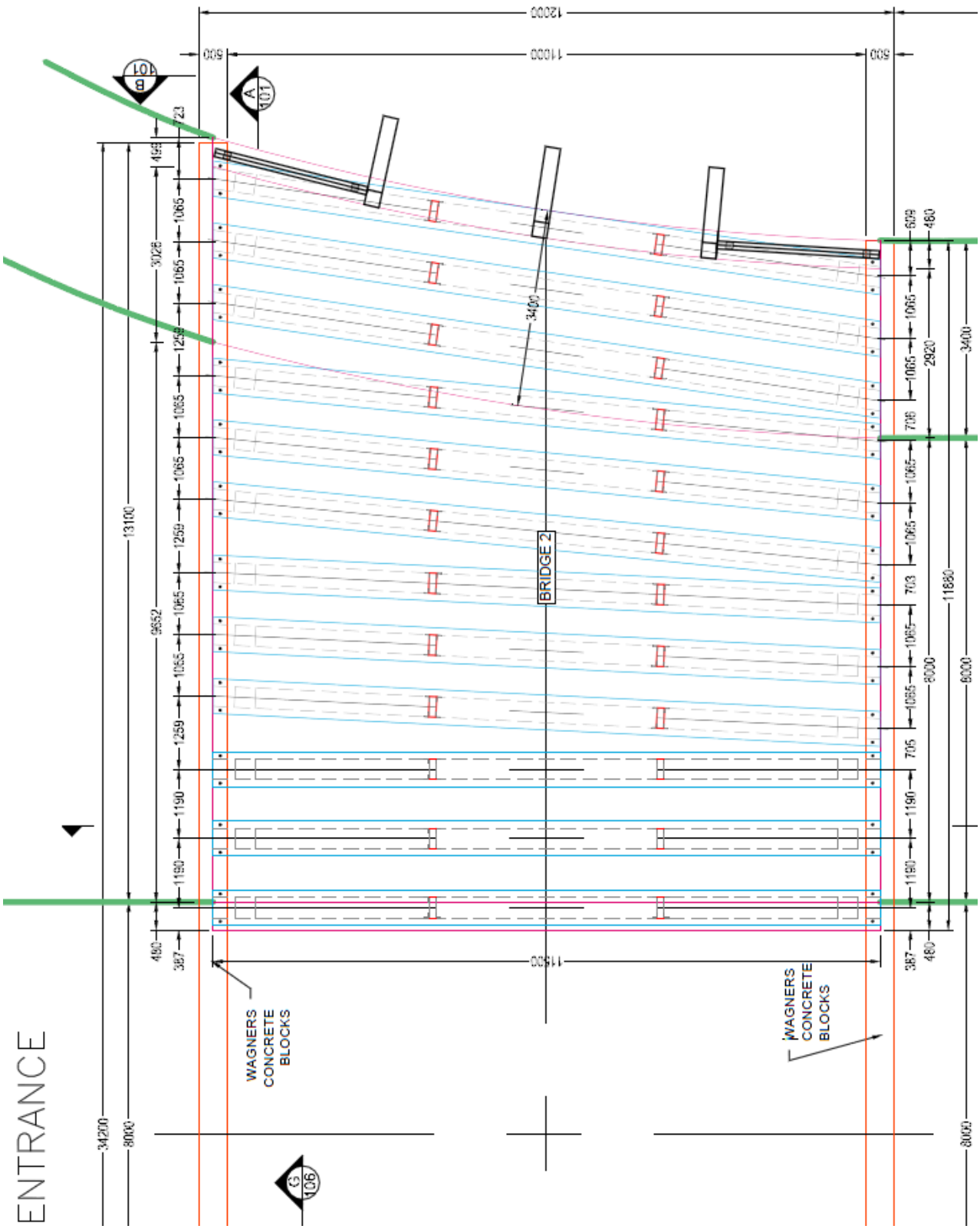

Figure 65. Top View of West Side of Symmetrical Bridge Showing Dimensions (i3 Consulting Pty Ltd).

The deck and kerb were constructed from Wagner's Earth Friendly Concrete (EFC) which is a binding mixture of fly ash and blast furnace slag, where there was no inclusion of OPC. The 28-day compressive strength of the material is 40MPa with a corresponding tensile flexural tensile of 5.5 MPa and an elastic modulus of 28 GPa. The deck consists of N16 bars at 150 mm each way on the top, and N16 bars at 125 mm each way on the bottom. The footpaths on both bridges have N12 bars at 150mm each way on the top only. The reinforcement installation in the East Bridge is shown in Figure 66.

Figure 66. Reinforcement Installation at Toowoomba Bridge Site, QLD in September 2014 (Wagners).

Figure 67. Installation of FRP Girders at Toowoomba, QLD, in September 2014 (Wagners).

Fibre Reinforced Plastic (FRP) composite elements form the girders of the bridge structure that support the 200 mm road deck. FRP is a promising, and relatively new, material that is substantially lighter than steel of concrete while also being easier to install. Since these girders were not constructed from Geopolymer concrete, the strain and temperature data obtained from the applied sensors were not analysed within this project. Figure 67 shows the installation of FRP girders in the East Bridge in September 2014.

Design monitoring system and live load testing

During the construction of the bridge, two VWSG's and two RFSG's were embedded within the GPC of both the deck and interior kerb while four additional RFSG's were fixed to the FRP girders, as given in Figure 68. Consequently, strain and temperature data were obtained allowing for serviceability performance assessment of the bridge. Due to construction timing, the Hygropin sensor and Corrowatch Multi-probe shown in design description were not installed.

Figure 69 illustrates the three monitoring zones within the outbound bridge to the west side of the site.

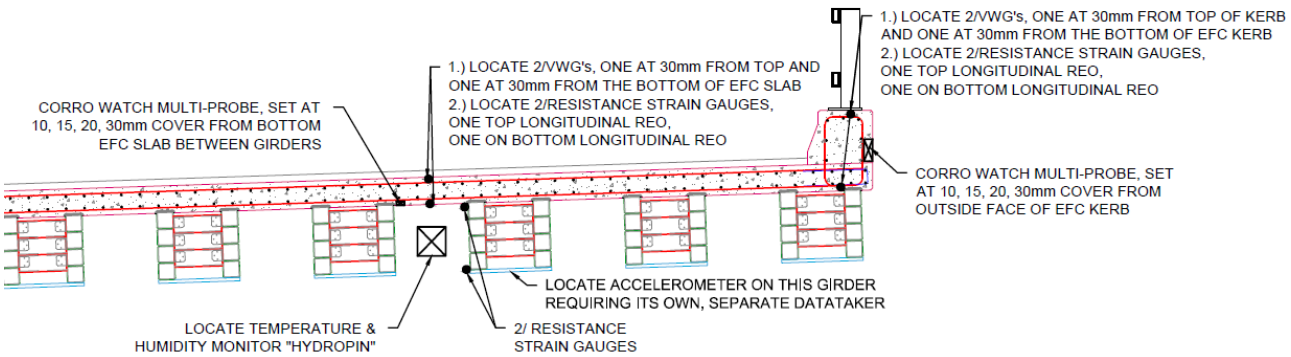

Figure 68. Locations of Sensors Placed at Toowoomba Bridge Site, QLD (i3 Consulting Pty Ltd)

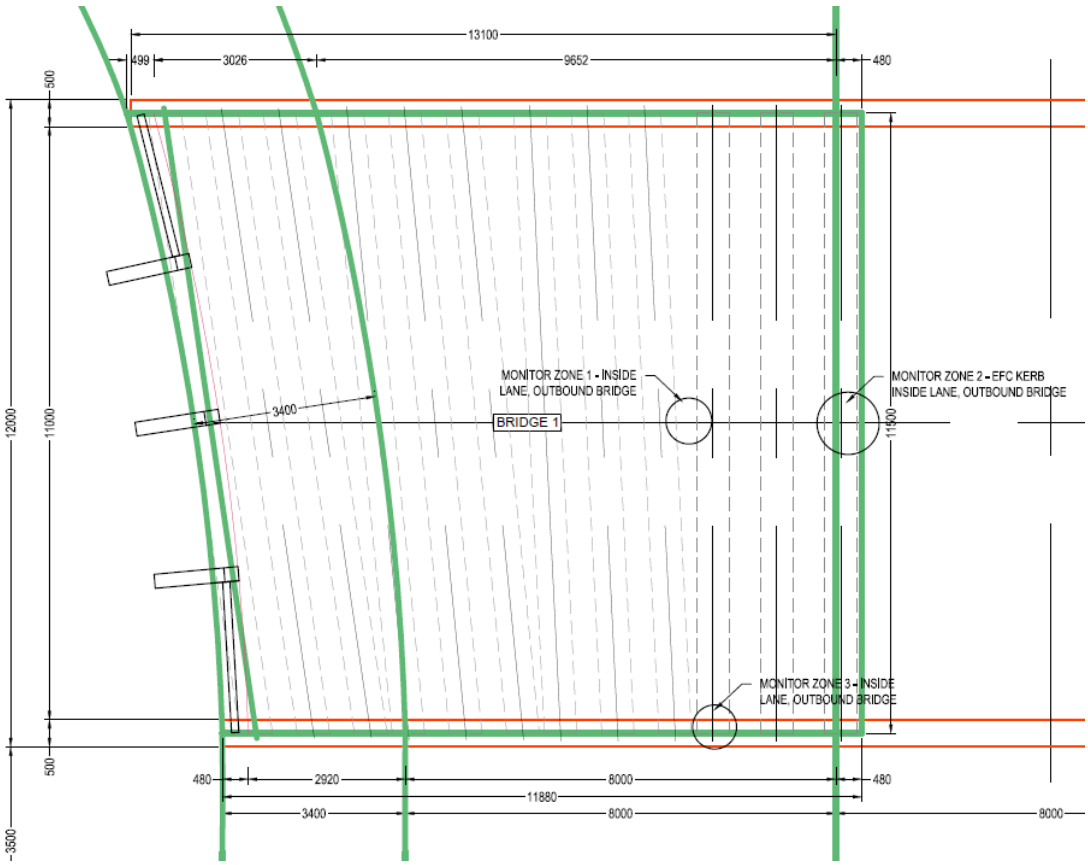

Figure 69. Monitoring Zones at Toowoomba Bridge Site, QLD (i3 Consulting Pty Ltd).

Vibrating wire strain gauges

The VWSG devices used within the bridge structure were purchased from DGSI (Durbham Geo Slope Indicator), as shown in Figure 70.

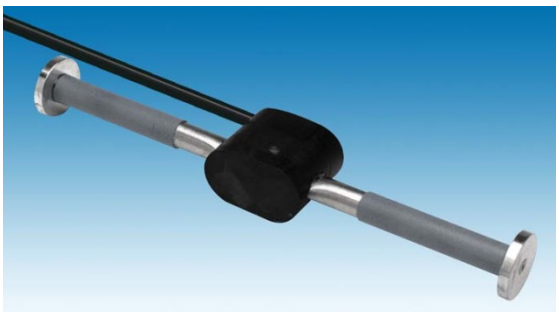

Figure 70. Vibrating wire strain gauges used (DGSI).

The specifications of the VWSG are:

- Range: 3,000 με with VW indicator
- Accuracy: ±0.1% FS
- Resolution: 1 micro-strain with VW indicator
- Thermal coefficient: 12 ppm/°C
- Length: 150 mm

Resistance foil strain gauges

The RFSG used to measure the strain data within the bridge were type FLA-5-11 and manufactured by TML, as given in Figure 71.

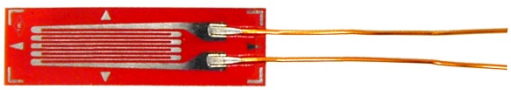

Figure 71. Resistance foil strain gauges (TML).

The specifications of the RFSG are:

- Gauge Factor: 2.13 ±1%
- Coefficient of thermal expansion: 11.8x10-6/°C
- Temperature Coefficient of G.F.: 0.1 ±0.05%/10°C
- Tolerance: ±0.85 m/m/°C

Data logger

A DT80 Series 2 data logger were utilised in the project to collect and store the sensing data from the VWSG and RFSG devices, as shown in Figure 72. The frequency for data collection was programmed at once per 30 minutes. The monitoring data stored locally can be retrieved by USB input, FTP, cell phone, Ethernet or

Web. This is achieved by converting the incoming analogue signal generated by the sensing devices into a digital signal, allowing for it to be stored for long periods of time or transmitted back to the office. The DT80 had a range of 12 digital channels that allows the easy storage and transmittal of data while it also is capable of processing up to 300 analogue inputs when connected to a CEM20 channel expansion module. The average power consumption of the DT80 was 1.35W (12VDC and 112.5mA) with a peak power of 12W (12VDC and 112.5mA).

Figure 72. DT80 Series 2 data logger (dataTaker).

A dataTaker CEM20 was installed into the sensing system in order increase the channel capacity of each analogue channel of the data logger (Figure 73). This is achieved by producing 20 universal data logging channels that connect to one of the DT80 analogue channels. Accordingly, the DT80 was able to have a total of up to 300 analogue inputs due to its connection with the CEM20 channel expansion module. The CEM20 required a 12VDC power supply with an average power consumption of 0.36W (12VDC and 30mA) and peak power of 0.36W (12VDC and 30mA).

Figure 73. CEM20 channel expansion module (dataTaker).

Once the monitoring system was installed, a water resistant enclosure was fabricated and mounted beneath the Geopolymer concrete slab to securely accommodate the DT80 data logger and the CEM20 channel expansion module, as shown in Figure 74.

Figure 74. Control box of the monitoring system at Toowoomba Bridge site, QLD.

Solar power supply and 4G wireless data communication system

A solar power supply system was added to the bridge site in December 2015 to allow 24/7 continuously monitoring of the bridge, as shown in Figure 75. A Comset 4G industrial Modem was also installed for retrieving stored monitoring data remotely. Figure 76 shows the controller and battery of the solar power system, as well as the 4G modem.

Figure 75. Solar power supply system used at Toowoomba Bridge site, QLD.

Figure 76. Interior view of the solar control box at Toowoomba Bridge site, QLD.

4G Wi-Fi router

Wireless communication is also introduced into this monitoring system. A 4G Wi-Fi router (Figure 77) was selected from Comset Inc. (Model: CM685P-W). It possesses a fast internet connect with download speeds of up to 21 Mbps and is designed to comply with Australian telecommunication standards. It performs fast and reliable data communication for a broad range of Machine-to-Machine (M2M) applications.

Figure 77. CM685P-W 4G Wi-Fi router.

Data analysis

This study may be regarded as a primary study on the serviceability of GPC structure. By gathering the temperature data at different depths, the thermal effect in terms of temperature gradient and average temperature in the GPC slab is evaluated. As the system is designed for long-term monitoring with a relatively long measurement interval, the data collected are not able to capture the response of the slab due to the traffic load. Thus, the measurements mostly capture the daily and seasonal strain and temperature variations. The collected temperature data will also be compared to the design limits in existing OPC concrete standard AS5100.

The collected strains are used to assess the stress at either upper or bottom of the slab and also reflect the slab curvature deformation. More importantly, the integrated information can be used to determine if there is any change in the GPC structure integrity under long-term exposure to the normal service conditions. For instance, if strains show a change with a large magnitude, it probably indicates that cracks are formed at some locations of the bridge.

Thermal conductivity measurements

Concrete has a low thermal conductivity that reduces the heat transferred in structural members which is the principal factor that determines the thermal gradient [66]. The occurrence of temperature gradient may lead to cracks in a concrete structure [67]. Although a broad range of research has investigated the mechanical properties of GPC, relatively little work has been done on the thermal conductivity of GPC. To predict cracking of GPC structure, the thermal conductivity parameter needs to be determined. The testing procedure adopted in this research is based on ASTM-C518 Standard-Test Method for Steady-State Thermal Transmission Properties by means of the Heat Flow Meter (HFM). Companion specimens, cast using the same EFC as the one used for the bridge slab, were batched to carry out the test.

This test uses a Heat Flow Meter Apparatus (HFM). The Heat Flow Meter consists of a cold plate and a hot plate which incorporate heat flux transducers for measuring heat flow. The specimen is placed between the two plates which are controlled and expose to different temperatures. The heat flow created from the hot plate to the cold plate is captured by the transducers. The device is calibrated against materials with known thermal conductivity and can be used to measure flat materials in a wide range of thickness and conductivity. The thermal conductivity (k-Value) and thermal resistance (R-Value) are determined. These values can be used to determine energy losses through a material. The experiment was conducted using the machine HFM436 from NETSCH Pty Ltd.

Live load testing

A load testing has been carried out on the bridge to assess the response to live loading. The test was divided into several scenarios using a known weight truck parking at different locations along the span. Three truck positions were selected with 5 mins parking time at each location which allows sensors to record the response of the bridge sufficiently. The truck started at the southern slab end drove through the traveling lane. The distances from the rear axle to the southern edge of bridge entry were 1.01 m, 5.65 m and 10.35 m respectively of the three parking locations (Figures 78 to 80). Meanwhile, the measurement interval of the strain gauge was adjusted to 1 min providing five recordings at each location. The truck total weight is 38 tonnes with 13 tonnes self-weight and 25 tonnes fully loaded with clay. Each axle is estimated with an average load of 63.33 kN.

As the load testing was completed in a short period of time, the strain data were not affected by the temperature; self-weight; creep or other factors. The

collected strain information was used to evaluate the flexural behaviour of the GPC slab subject to short-term loading. The data collected will be then compared to the finite element simulation results to assess the accuracy of an existing simulation model which is essential before investigating the thermal strain response of the bridge deck.

Figure 78. Live load testing: truck position 1.

Figure 79. Live load testing: truck position 2.

Figure 80. Live load testing: truck position 3.

Data validation - finite element model (FEM)

A finite element model (FEM) was developed using ANSYS APDL15.0 to simulate the bridge behaviour. The accuracy of the finite element analysis (FEA) is assessed primarily based on the live load testing strain results. The daily temperature variation was modelled as a sinusoidal function and calibrated using the measured data. The simulation results from FEA are compared to the measured temperature gradient and corresponding strain data in the concrete slab under thermal effect.

Results and discussion

Average temperature

The design limit of average bridge temperature is significantly important as it affects the safety and economy of a bridge. Current standard divides Australia into three regions while assigning specific extreme values for bridge average temperature. The GPC bridge at Toowoomba, QLD is located in Region I and the height above the sea level is less than 1000 m. The extreme shade air temperature ranges from 0 ^{o}C to 46 ^{o}C. Accordingly, the recommended maximum and minimum bridge design temperatures are 48 ^{o}C and 3.5 ^{o}C, respectively, which are calculated by linear interpolation from the standard.

The bridge average temperature can be calculated from the temperature data collected by the strain gauges at various locations. Figure 81 shows the computed monthly maximum and minimum mean bridge temperatures. The calculated mean bridge temperatures were plotted for several critical months in 2015. Typically, both maximum and minimum bridge temperatures show the same increase and decrease tendency in accordance with the seasonal change. The monthly maximum and minimum mean temperature values were 39.31°C and 10.36°C recorded in February and July respectively, which correspond to summer and winter in Australia. Despite the limits of one-year temperature data, the measured maximum and minimum bridge mean temperatures are significantly lower than the one specified in AS5100–2017. Nevertheless, the current standard AS5100 Part 2 is also applicable for the GPC bridge as the calculated bridge mean temperature values are within the design range.

Thermal conductivity

Table 15 shows the results of thermal conductivity of the Geopolymer concrete (EFC) for temperatures ranging from 0 to 80 ^{o}C. The average thermal conductivity is 0.402 W/(mK) and the thermal resistance is 0.052 (m^2 K)/W. The density of the Geopolymer concrete was 2420 kg/m^3. The accuracy of the results is within ±10%.

Similar to fly ash based Geopolymer concrete, the EFC thermal conductivity is lower than the one of metakaolin-based Geopolymer concrete reported in the literature and also lower than the one of OPC concrete which ranges from 0.8 to 1.2 W/(mK) [68, 69]. Results are consistent with the conclusions by Demirboga [66] and Kim [67] where the increase of fly ash and silica fume replacement caused a significant decrease in the thermal conductivity [67]. This is attributed to the lower density of the amorphous structure of fly ash based Geopolymer compares to OPC [70].

Figure 82 shows the effect of the temperature on thermal conductivity of GPC. The thermal conductivity increases with the temperature increasing from 0 ^{o}C to 60 ^{o}C. However, the thermal conductivity slightly decreases when the temperature is higher than 60 ^{o}C and this might be due to the dehydration of the concrete [71].

On the one hand, a low thermal conductivity of concrete is useful for heat insulation. Combined with a good resistance against fire, fly ash based GPC appears to be a suitable concrete material for the building construction. On the other hand, concrete with high thermal conductivity can reduce the temperature gradients in structures. The thermal stresses resulting from temperature gradients may cause concrete cracking, concrete mechanical property degradation and even warpage in the structure. Bridges are among structures that tend to encounter temperature differentials between their top and bottom surfaces. In contrast to buildings, bridges do not need thermal insulation. Therefore, concrete with high thermal conductivity is desirable for bridges and related structures [72]. In this thesis, the impact of the lower thermal conductivity of the EFC on structural serviceability will be assessed.

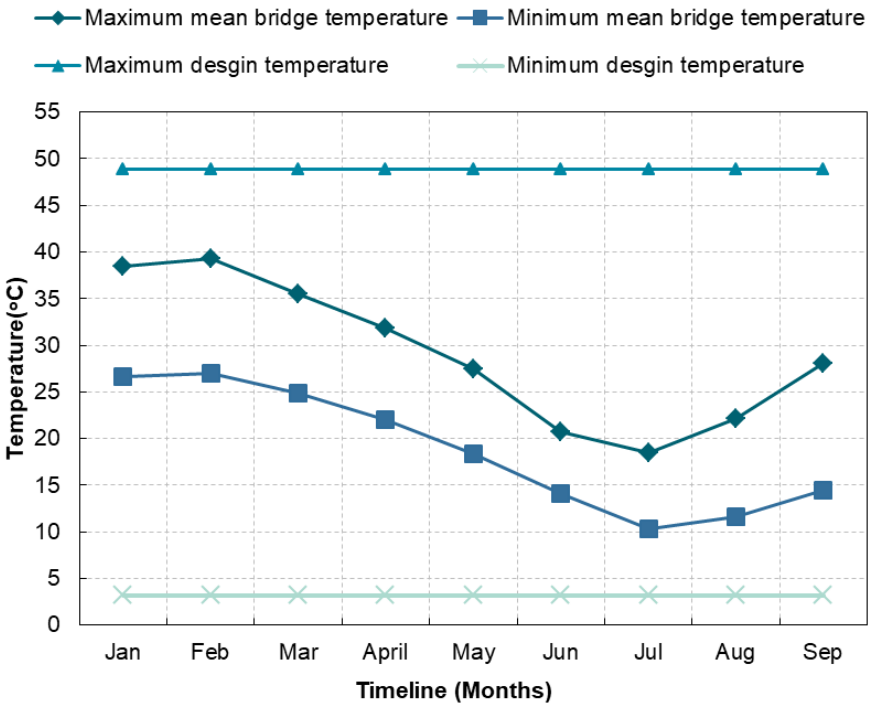

Figure 81. Average bridge temperatures versus temperature design limits.

Table 15. Thermal conductivity of Geopolymer concrete (EFC).

Mean Temp. (°C)	Thermal Conductivity W/(m·K)	Thermal Resistance (m²·K)/W	Density (kg/m^3)
-0.1	0.372	0.056	
19.8	0.389	0.054	
40.0	0.401	0.053	2420
60.3	0.433	0.049	
79.7	0.412	0.052	

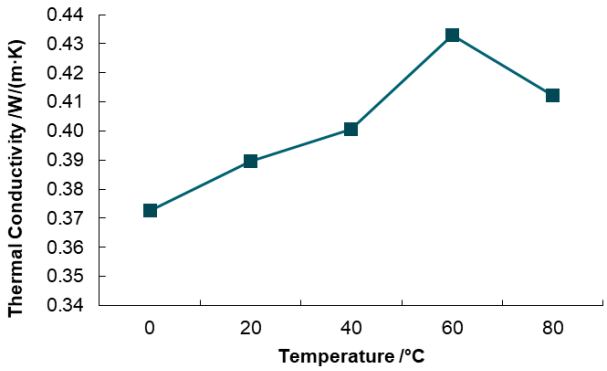

Figure 82. GPC thermal conductivity versus temperature.

Comparing ambient and slab temperatures

Figure 83 presents the temperature change over several critical months in 2015 from the hottest month, January, to the coolest month, July, in QLD Australia. The temperature at both upper and lower layers of the slab follows the seasonal temperature variation. The maximum bridge temperature was found at the top layer of the slab in early January with 47.2 ^{o}C, while the coolest temperature was measured in the bottom part of the slab in late June with 2.7 ^{o}C.

There is a significant difference in ambient temperature daily amplitude at Toowoomba throughout the seasons. Moreover, the temperature at both top and bottom of the concrete slab dramatically decreases from summer to winter. In summer, the daily amplitude of the top slab is about 15 ^{o}C while it is only 11 ^{o}C at the bottom of the slab. In winter, the daily temperature ranges at top and bottom are 8 ^{o}C and 6 ^{o}C respectively. The daily temperature amplitude in the slab decreases due to the solar radiation reduction in winter.

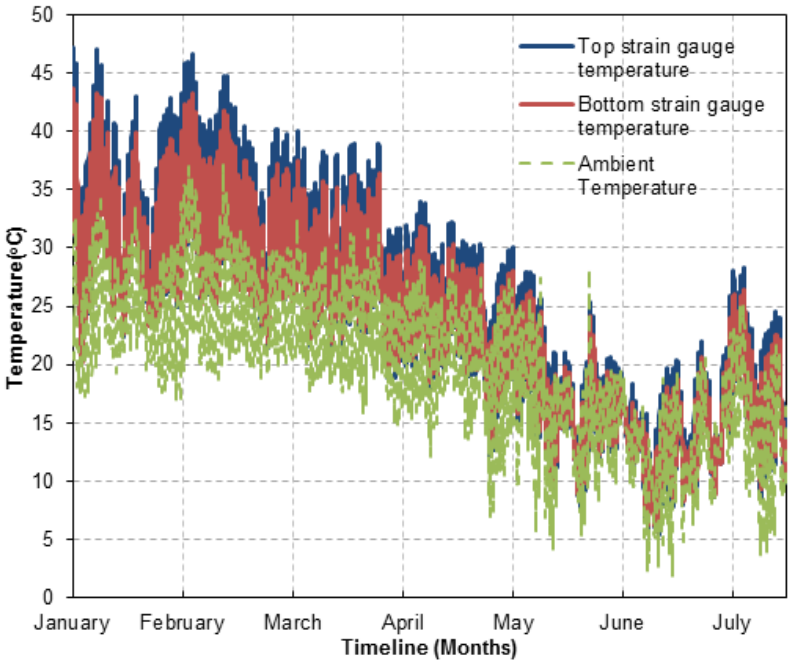

Figure 83. Bridge Temperature data from January to August 2015.

Bridge daily temperature change

Figures 84 and 85 show detailed temperature data over 48 hours in summer and winter, respectively. The temperatures present a daily cycle in both seasons. A temperature difference remains throughout the slab as the heat in concrete comes from the solar radiation and usually takes hours to transfer from the top surface to the bottom. A time delay is observed between ambient and concrete temperature variations for both maximum and minimum temperatures. This time delay is strictly governed by the thermal conductivity. The ambient temperature reaches its maximum or minimum firstly; then comes the top slab temperature while the bottom slab temperature comes to the last.

In summer, recorded temperature on top slab is approximate 10 ^{o}C higher than the ambient temperature. The slab experienced a positive temperature difference approximate from 8:00 to 20:00, while a negative temperature gradient happened in the next 12 hours. In winter, bridge temperature shows only 2 ^{o}C to 3 ^{o}C difference to ambient temperature with positive temperature gradient occurring from 10:00 to 20:00.

Temperature gradient

The temperature gradient will largely depend on the thermal conductivity. It is important as it can generate thermal stress leading to concrete cracking at large magnitude. Following results show the extreme temperature difference measured between the upper and bottom slab area as well as the temperature gradient distribution in both summer and winter.

Figure 86 shows the calculated temperature gradient from summer to winter using the results from the top and bottom strain gauges located in the concrete 30 mm and 140 mm from the top slab surface. The maximum positive and negative temperature differences both happened in January: 6.5 ^{o}C and -1.7 ^{o}C respectively. The positive temperature gradient decreases from summer to winter due to the decline in solar radiation strength. However, there is no significant influence of seasons on the magnitude of the negative gradient which remains similar throughout the year.

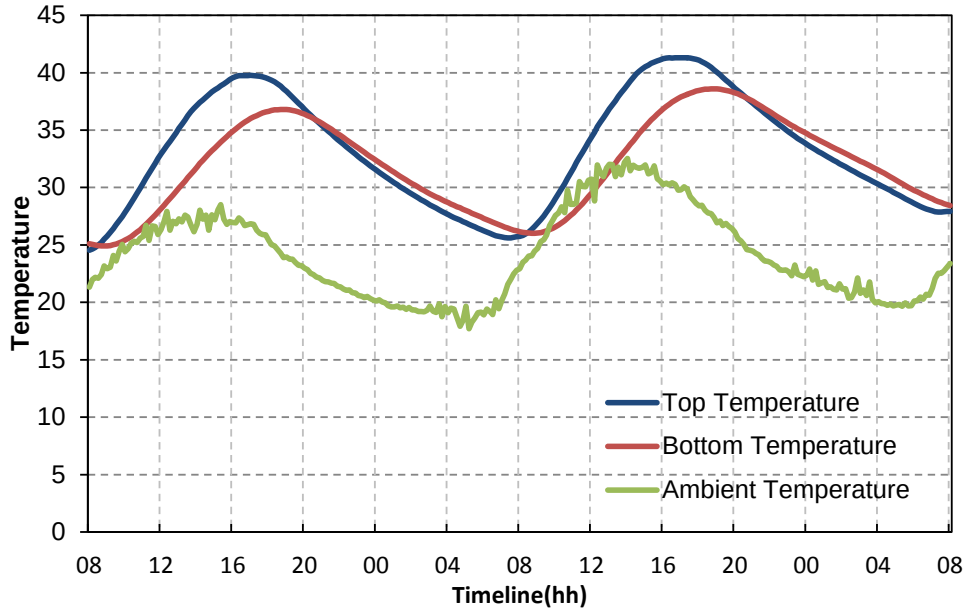

Figure 84. Temperature measurements taken over a 48 hour period during summer: top and bottom of the slab and ambient temperatures.

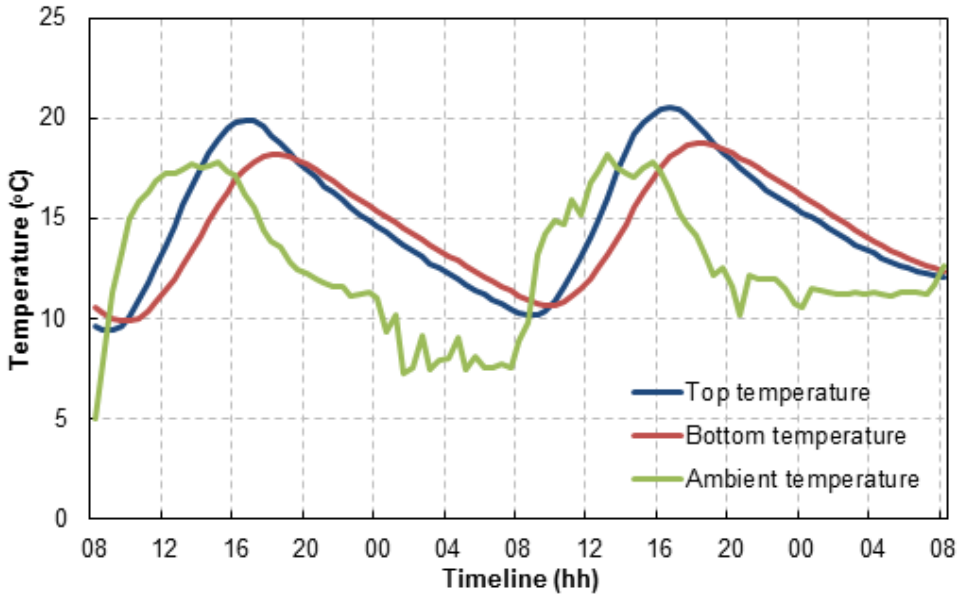

Figure 85. Temperature measurements taken over a 48 hour period during winter: top and bottom of the slab and ambient temperatures.

Figures 87 and 88 show the summer and winter temperature gradient distributions, respectively. The temperature gradient is divided into several classes with an interval of 0.5°C. Both trend lines in summer and winter are potentially subjected to a normal distribution curve. The positive and negative temperature gradient equally own 50% frequency in summer, while the GPC slab mostly shows negative temperature gradient in winter with total distribution frequency of 58.86%. The largest frequency happened at negative temperature gradient class [-1~-0.5] with 30.03% in summer and 27.33% in winter. The negative classes [-1~-1.5] and [-0.5-0] have a similar frequency in both seasons with 10% in summer and 16% in winter. Each group in positive temperature gradient owns a similar percentage of approximately 5% frequency.

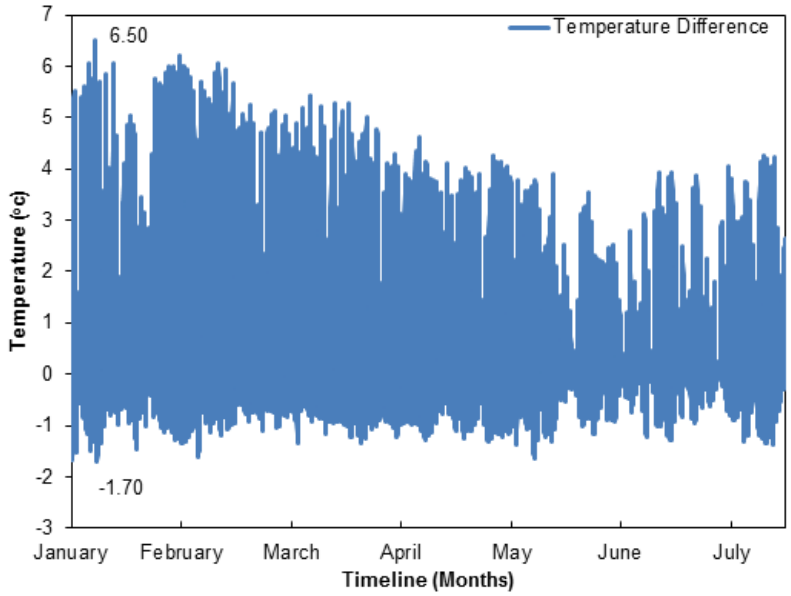

Figure 86. Temperature gradient between top and bottom of the slab.

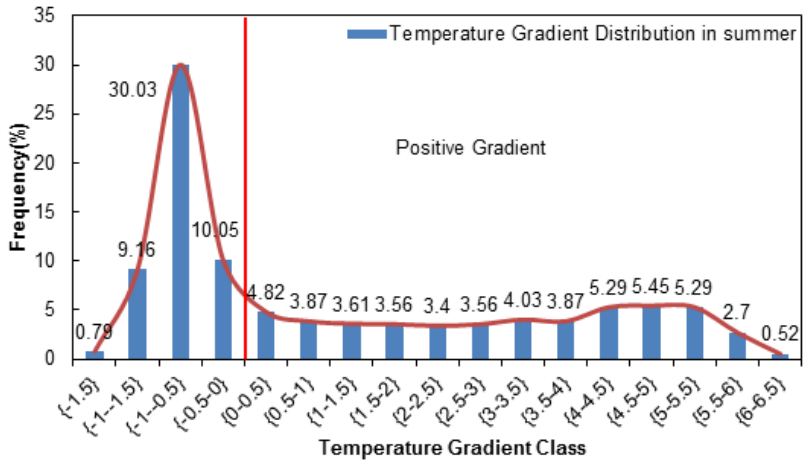

Figure 87. Temperature gradient distribution in summer.

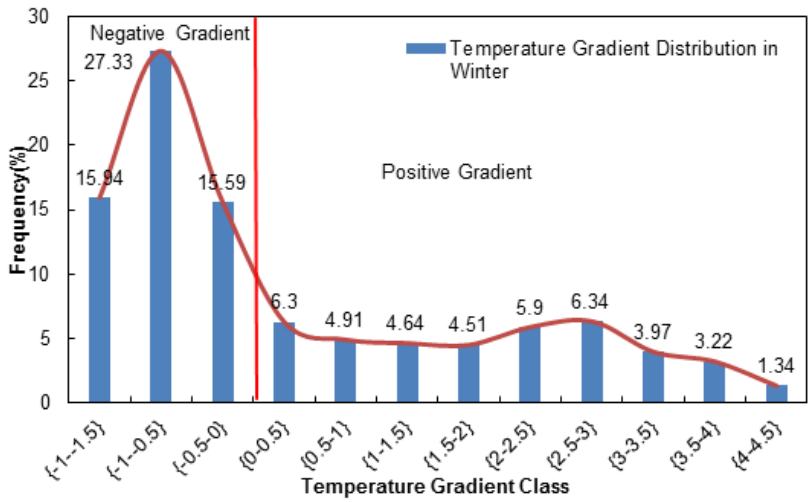

Figure 88. Temperature gradient distribution in winter.

Curvature of the slab

Curvature of the PGC slab is representative of its response to environmental loading, which governs the magnitude of the thermal stresses in the slab. Slab curvature quantifies the warping and load deflection based on the collected strains. The positive curvature value indicates an upward deformation shape at slab edge and the negative value presents a downward deformation shape at slab edge.

A summary of half a year slab curvature values is presented in Figure 89. Curvatures are calculated using the measured strain from the top and bottom of the slab.

Results show the actual slab curvature development due to multiple factors, including temperature gradient, moisture gradient and restrained condition at the interface between the slab and the girders.

The actual slab curvatures are mostly positive (>99%) and the daily slab curvature range decreases from summer to winter. As a result, the top surface would be subjected to tension stress. Therefore, it is predicted that the concrete cracking is more likely to propagate firstly at the top surface of the slab.

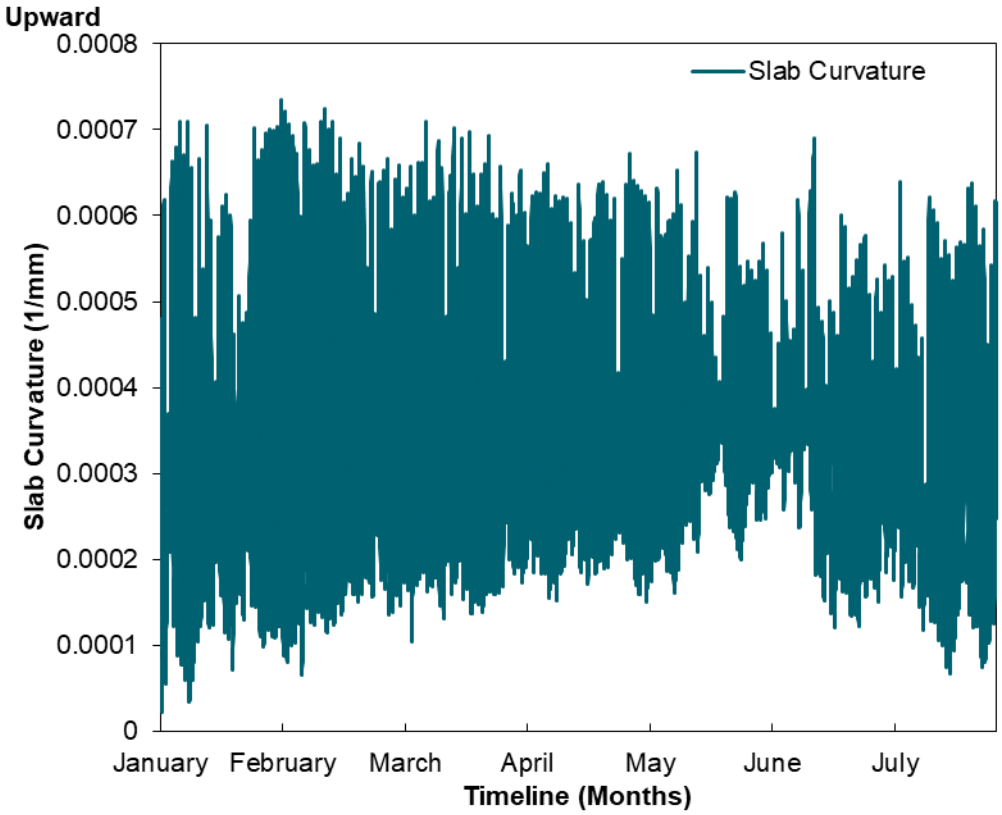

Figure 89. Measured slab curvature.

Correlation between slab curvature and equivalent temperature gradient

Figure 90 shows a linear relationship between the slab curvature and equivalent linear temperature gradient. The equivalent linear temperature gradient was also calculated using the following equation based on the data collected:

$$T_{eq} = \frac{T_b - T_t}{h} \quad (5)$$

Where T_{eq} is equivalent temperature gradient (^{o}C/mm); T_b and T_t are the temperature measured at the bottom and the top slab (^{o}C), and the h is the concrete thickness between the measured locations (mm).

Presented data were derived from February 2016, which is the hottest month in QLD Australia providing the widest range of temperature gradient. The slab curvature and equivalent temperature gradient show a linear relationship. The slope represents the thermal coefficient of the GPC with $11\times10^{-6}/^{o}$C which is similar to OPC concrete as assumed earlier. The range of curvature is from 0.00061/m to -0.000015/m.

It is noteworthy that the slab deflects upward rather than remaining flat (zero curvature) at temperature gradient zero as the curvature ranges from around 0.0001/m to 0.0002/m. It can be explained as the slab is usually cast during the daytime which is associated with a positive temperature gradient. Therefore, an effective negative temperature gradient is required to balance this initial curvature. The magnitude of the initial slab curvature is often affected by the ambient temperature; weather condition and curing condition [73].

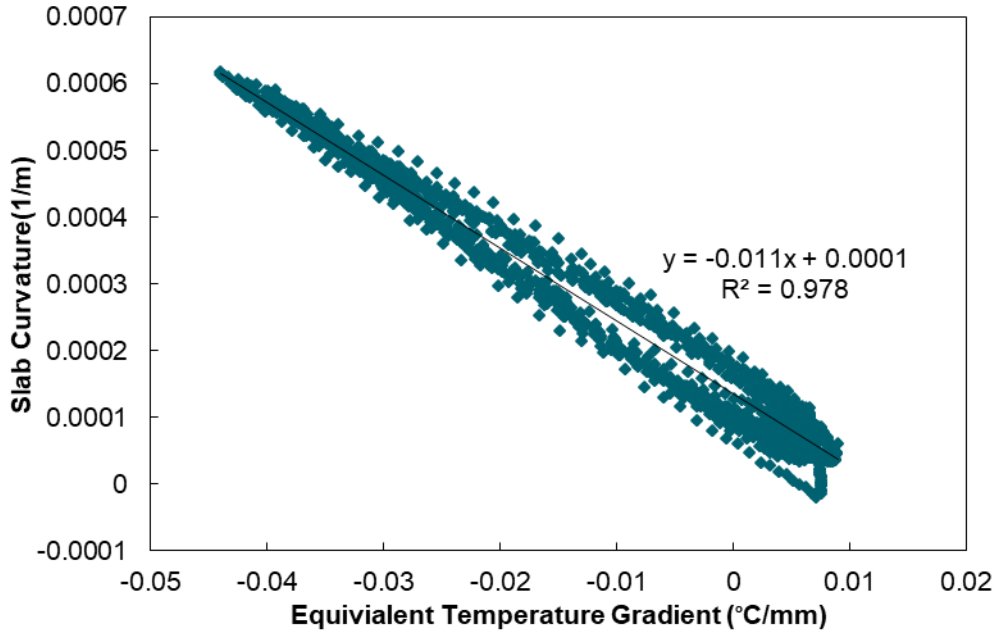

Figure 90. GPC slab curvature versus temperature gradient in February.

Strain analysis

Figure 91 shows the strain variation at both top and bottom slab from summer to winter. The daily strain range decreased from summer to winter is consistent with the previous results where the daily temperature range decreased throughout the same period. However, the tensile strain both at top and bottom slab shows an increasing tendency from summer to winter. Over this period, the maximum tensile strain at both upper and lower slab happened in winter, namely, +113 με and +39 με; the maximum compressive strain is measured at the top of the slab with -60 με which is only a small proportion (less than 5%) of the ultimate compressive strain.

Figures 92 and 93 present the detailed one-week strain data extracted from Figure 91. A good correlation between the strain and temperature gradient is observed. The bottom slab always presents tension strain in normal service conditions. Both top and bottom strains were governed by the temperature gradient. As a result, strains in both seasons are consistent with the temperature gradient change. The largest positive temperature gradient determines the maximum compressive strain at the top slab and the maximum tensile strain at the bottom slab.

As mentioned earlier, negative thermal gradient can be an issue for the serviceability of the structure inducing tension in the concrete top cross section. As shown above, the presence of negative gradient causes high tensile strain occurring at the top of the slab and reaching a maximum when the largest negative temperature gradient appears. This supports that concrete cracking is more likely to form at the top surface rather than the bottom.

In winter, the measured tensile strain at both top and bottom is higher than summer in spite of smaller maximum positive temperature gradient. This is because the strain is affected by a lower average temperature in winter. However, average temperature change typically would not disturb strain data if the deck axial deformation is not restrained which allows the slab to freely expand and contract with the temperature increase and decrease. In this particular bridge, the concrete top-slab is anchored to the composite girders by shear connectors and the different thermal expansion coefficients between the composite FRP girder and GPC slab will create additional friction stresses as the two materials try to match the movements of each other. Those fictions act as a partly rigid restraint to the slab movement.

Results show that the strains are mainly affected by the thermal effect which is significantly greater than other load factors. Indeed, the strains induced by a fully loaded truck at both top and bottom of the slab are in compression only with a maximum of -35 με whereas the total strain range due to thermal loading is from -40 με to +120 με. A 4.0 MPa peak stress over a year happened in winter and was located at the bottom slab which is close to the ultimate tensile stress of 5.7 MPa. To the contrary, compressive stress built up due to the thermal effect remains very small compared to the ultimate compressive strain of GPC.

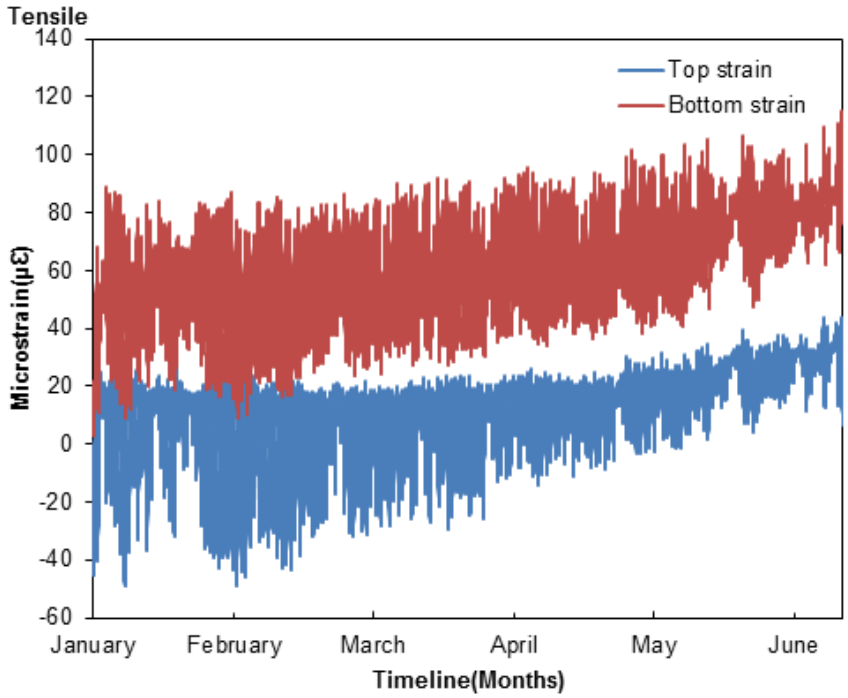

Figure 91. Strain variation of top and bottom slab from summer to winter.

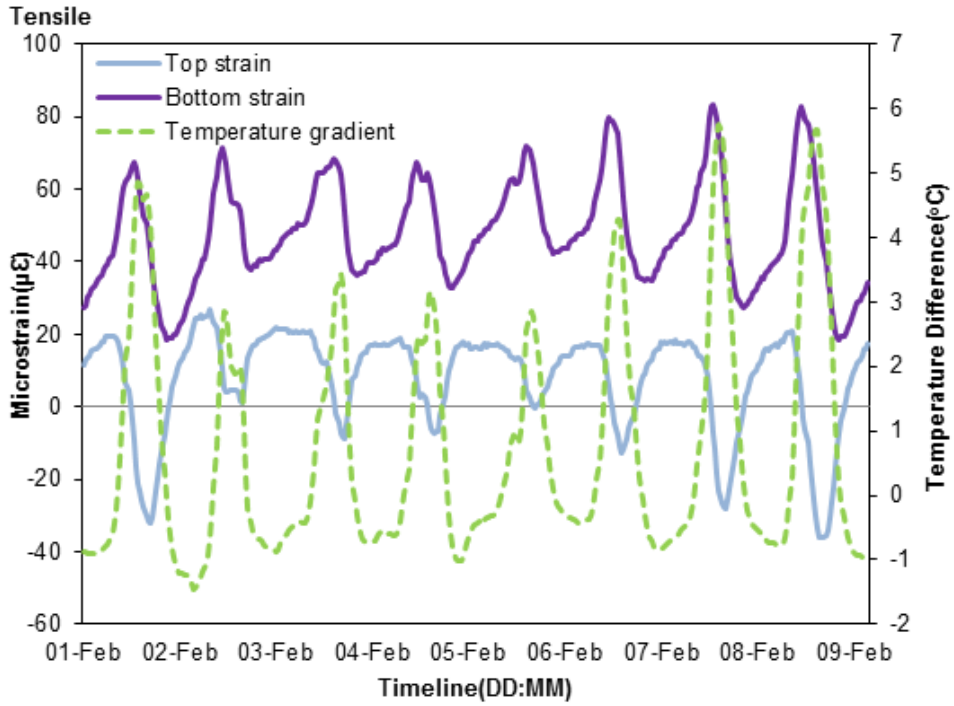

Figure 92. One week of strain and temperature data in summer.

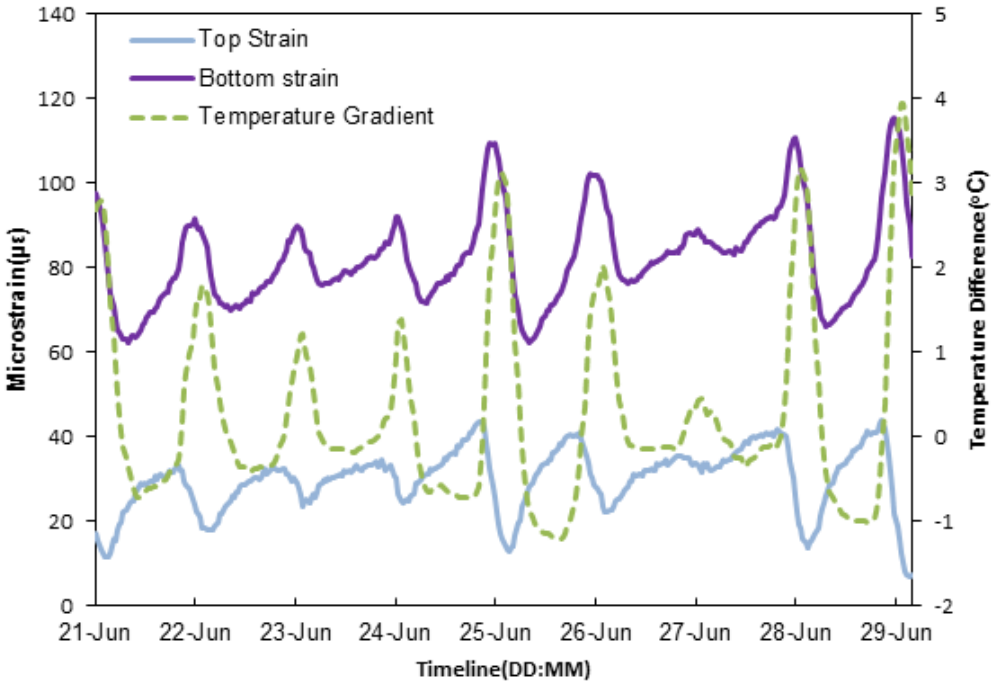

Figure 93. One week of strain and temperature data in winter.

Data validation – FEM

Introduction

A FEM was developed using structural software ANSYS version 15.0 to validate the strain data collected from the GPC bridge. The model was calibrated based on the results of the live load testing. Then, a further thermal strain analysis was carried out by implementing the measured thermal data and concrete parameters.

Figure 94 shows the overview of the FEM model for the GPC bridge deck. The bridge deck consists of Geopolymer concrete bridge slab placed over 12 fibre reinforced polymer girders along the span of the bridge. The dimensions are: 11.5 m span; 13.1 m width on Plains Road-side and 11.88 m on Wellcamp Business Park-side. The slab thickness is 200 mm and the girder height is 500 mm. The interface between the girders and bridge slab is regarded as a rigid connection without friction and separation. This assumption ignores any movement caused by the little difference in thermal expansion between the girders and concrete deck.

The primary purpose of the FEM simulation is to analyse the performance of the slab exposed to thermal loads. Linear analysis was adopted in the simulation as the maximum compressive strain measured in the concrete are less than 5% of the ultimate compressive strength. Eight nodes elements solid 278 and solid 185 were used for both deck top-slab and girders for thermal and structural field respectively. The meshing size is 0.2 m for each element.The boundary condition was applied to the ends of the girders: simply supported. Creep, shrinkage and cracking were not considered in this model.

Material properties are shown in Table 16 The thermal expansion coefficient used of EFC is 11 με/°C. The FRP has a similar elastic modulus and thermal expansion coefficient. The high compressive and tensile strengths make it a suitable material for bridge girder.

Table 16. Material properties.

Material Properties	EFC	FRP
Comp. strength (MPa)	49	550 (longitudinal)
Tensile strength (MPa)	5.7	600 (longitudinal)
Elastic modulus (GPa)	39	41.8
Density (kg/m^3)	2420	2000
Coeff. of thermal expansion (με/°C)	11	10

Model calibration- live load test

Prior to simulating the thermal effect on the bridge, the FE model was tested using the live load testing data. Table 17 gives the different truck parking locations along the traveling lane defined as the rear axle position to the southern entry of the bridge.

Figure 95 shows the truck loading applied in the model. As the truck was stationary at each location for 5 mins, the wheel loads are considered as a static force applied on the nodes. Each wheel loading is estimated to be equal to 63.33KN.

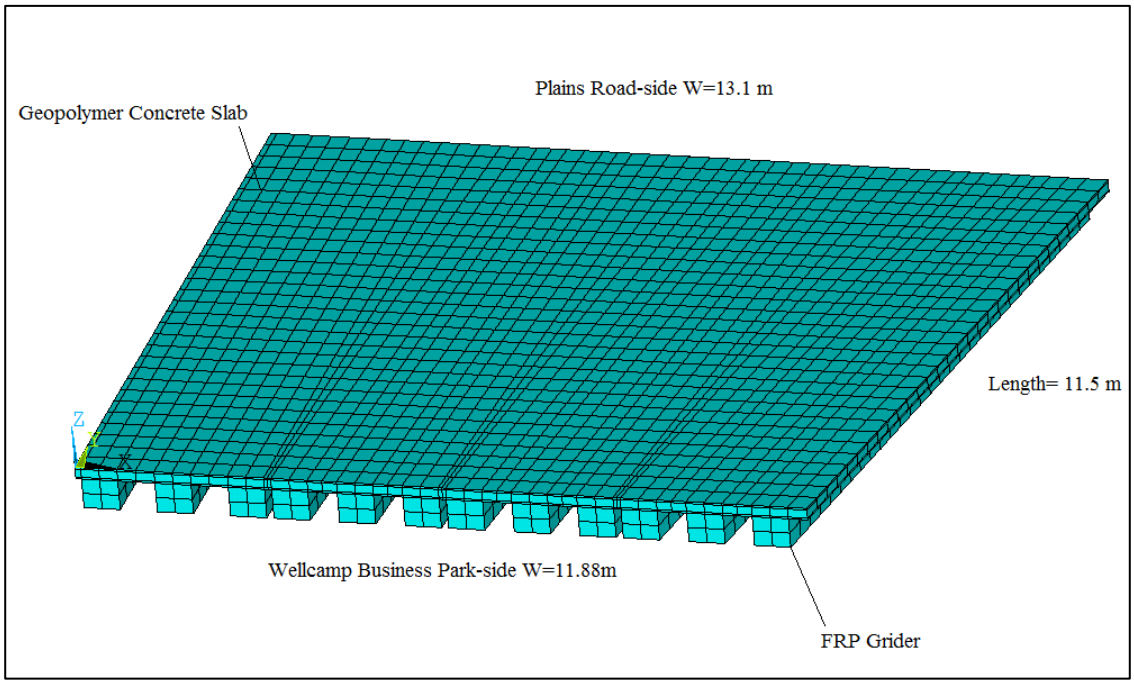

Figure 94. Finite element mesh - bridge view.

Figure 96 shows the strain measurement at the mid-span of the traveling lane and simulation results from the FEM. For truck position 1, the front wheels are located close to mid-span and the top strain is -20 με. For truck position 2, the rear axle is located at the mid-span of the slab. The strain at the top slab reaches the maximum compression strain of -35.24 με as the rear axle carry the majority of the truck weight. Strain then decreases to -7 με in truck position 3. The bottom slab always shows little change in compressive strain but performs the same trend of strain as the top slab.

The simulation results present a similar concrete strain response to the different loading locations. Overall, the difference between the real measurement and simulation is typically less than 5 με which is within an acceptable range.

Table 17. Truck position in FEM.

Item	Distance between rear axle to the entry edge (m)	Wheel load (kN)
Position 1	1.01	63.33
Position 2	5.65	6333
Position 3	10.35	63.33

Thermal-structure coupled field simulation

After validating the FEM using the data from the live load testing, a thermal analysis of the bridge is carried out. Temperature and strain response across the thickness of the slab can be extracted throughout the entire simulation period. The thermal simulation process uses indirectly couple-field method which takes into account the interaction between thermal expansion/contraction and mechanical stress [74]. Thermal-structure couple-field method improves the simulation accuracy where the input of the structural analysis depends on the results from thermal effect. Temperature and heat loss to the surrounding were given as time sinusoidal function and applied as the final boundary conditions in the thermal field. The temperature input in the thermal field was calibrated using the typical daily temperature cycle in summer and winter. The computed thermal results would be transferred into the structure field to calculate the corresponding strain.

Figure 97 shows the simulation results in terms of total strain over 48 hours in summer in comparison with the measured data. The top and bottom of the slab simulation results were extracted from the specific nodes corresponding to the VW-strain gauge location. Results either from strain gauges or FEM show a similar daily cycle variation.

In summer, the top strain is mostly in compression while bottom strain in tension. Bottom strain reaches a maximum tensile strain early in the afternoon which is consistent with the temperature gradient increasing, whereas strain at the top reaches its maximum compression around 17:00 which corresponds to the time of the maximum temperature gradient. Tensile stress appears at the top of the slab at night due to the negative temperature gradient. The simulated maximum tensile value at the top and the bottom of the slab is +11.12 με and +41.2 με respectively which are close to the measured results of +7.85 με and +53.1 με. The maximum measured compressive strain at the top of the slab in summer is -47 με whereas the result from the simulation is -24.94 με.

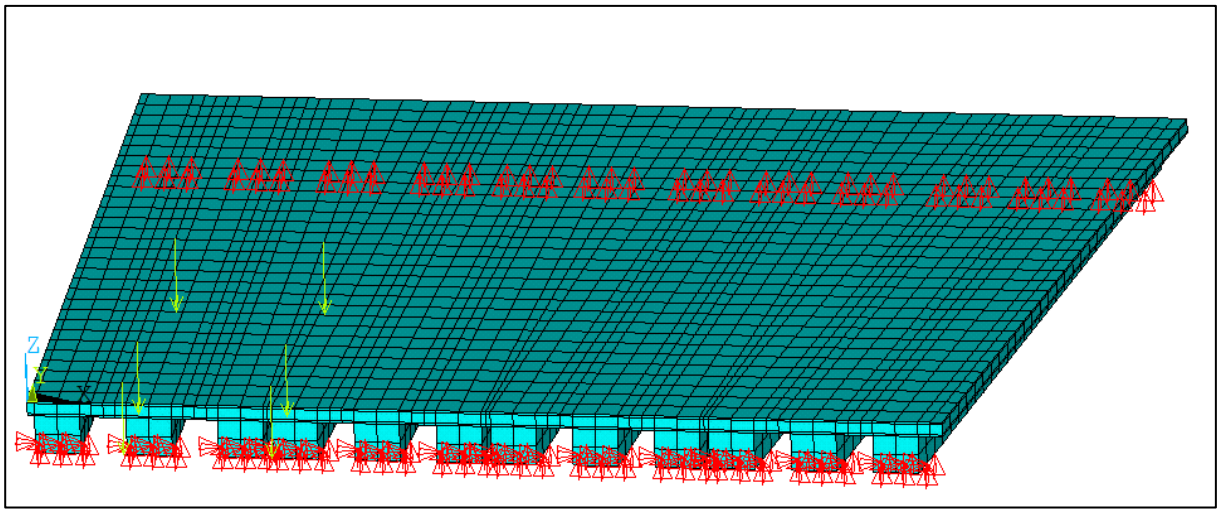

Figure 95. Truck loading in FEM (truck position 1).

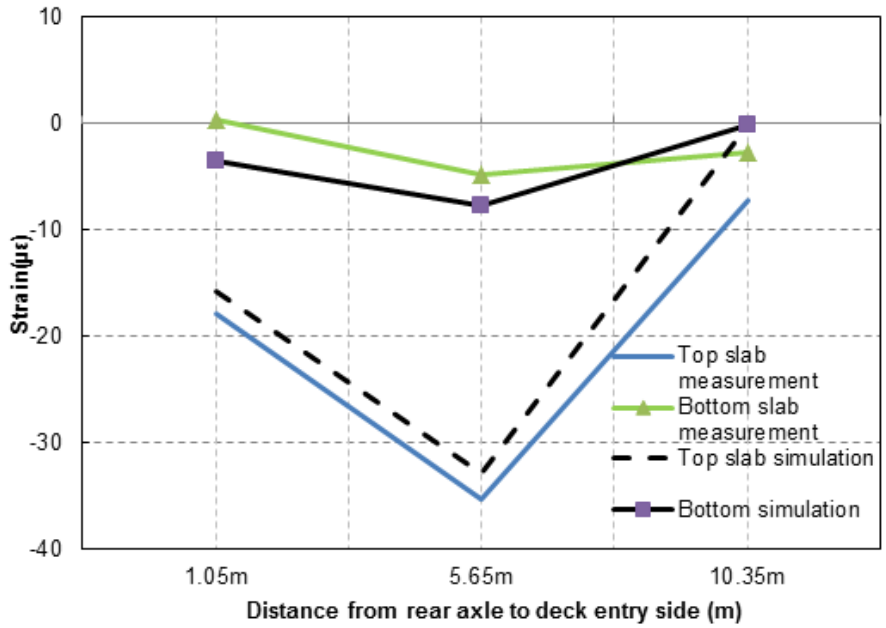

Figure 96. Live load testing results from measurement and simulation.

Figure 98 shows the simulation results in comparison with the measured data in winter. The top and bottom strains of the slab are both in tension and the strains in winter reach the maximum value few hours earlier than in summer. The measured maximum tensions in the top and bottom of the slab are +31 με and +95 με respectively while the simulation results are +30.9 με and +74.6 με. The measured minimum values at the top and bottom of the slab are +8.4 με and +55 με respectively, while the simulation result is +7.39 με and +44.5 με.

Overall, FEM simulation results in both summer and winter are in good agreement with measured data. The difference between measured and predicted strains is typically less than 15 με. However, some differences between experiment and simulation were noticed. The largest deviation happens at the maximum strain value in the top and the bottom of the slab. There are a few possible causes for this: (i) the FEM did not consider the resistance of the relative movements between FRP girder and GPC slab and (ii) the shrinkage; creep and moisture gradient are not taken into account. Nevertheless, the simulation results are still within the acceptable range.

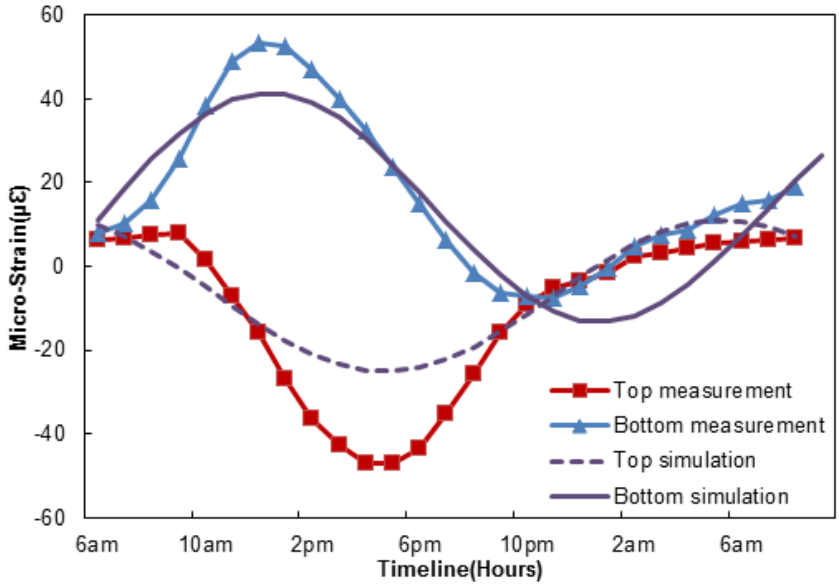

Figure 97. Results of measurement and simulation over a one day cycle during summer.

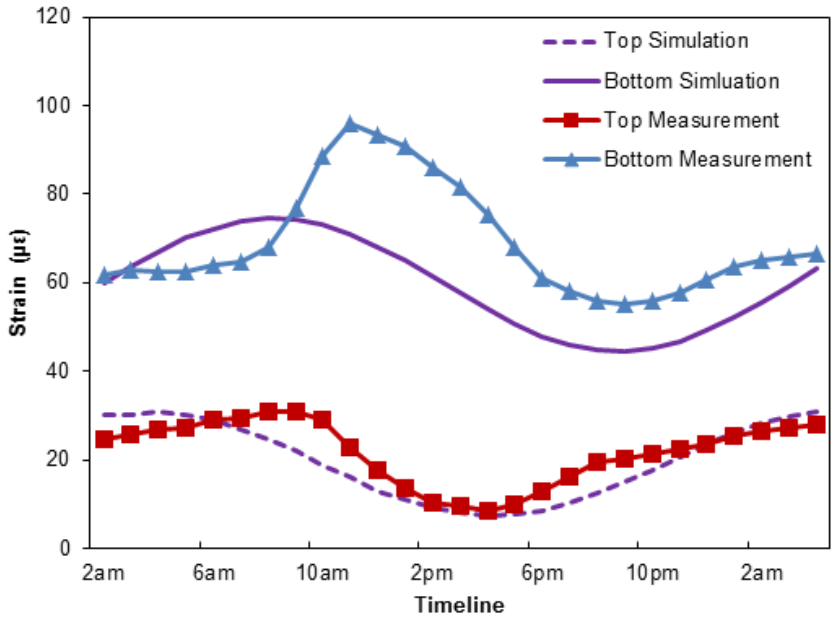

Figure 98. Results of measurement and simulation over a one day cycle during winter.

Conclusions

The results presented in this part assess the serviceability of a GPC bridge deck top-slab under normal site conditions. Overall, the GPC slab performs similar to that expected of a slab constructed with OPC under daily and seasonal temperature variation and without any observed change in structural integrity. The results show that the behaviour of the GPC slab is mainly influenced by the thermal loading, including uniform temperature change and temperature gradient. The response of the bridge to truck loading in terms of deflection was correctly predicted by the FE modelling and in agreement with serviceability demand requirements.

The coefficient of thermal expansion of the GPC was assessed using the strain and temperature data obtained from the GPC slab. The coefficient of thermal expansion of the GPC was found to be similar to that expected for OPC concrete. However, the thermal conductivity of the GPC is lower than that for OPC concrete, which leads to a larger temperature gradient in the slab.

Westport Boat Ramp, Port Macquarie NSW, and Rocky Point Boat Ramp, QLD (UNSW)

Introduction

Durability of Geopolymer concrete in marine environment is under investigation at the Westport Boat Ramp Stage 2 Works at Port Macquarie, NSW. As shown in Figure 99, the aged boat ramp built with cast-in-place OPC concrete was replaced by precast Geopolymer concrete planks. Wagners was selected as the contractor by the Port Macquarie Hastings Council for supply of the planks.

A total of 44 Geopolymer concrete planks were prefabricated at Wagners' precast yard at Wacol, Queensland and then transported to the site at Port Macquarie, NSW, in June 2016. The work on replacing the boat ramp was completed end of July 2016. It is noteworthy that all Geopolymer concrete planks are submerged in sea water permanently after installation.

Westport boat ramp

The new boat ramp consists of 4 rows of planks with 11 planks in each row. The plank is made of Wagners EFC (Earth Friendly Concrete). The dimension of the precast plank is 4,000 mm long × 1,000 mm wide × 200 mm thick, with the mass being 2.0 tonnes. The EFC planks were cured for at least 7 days. The compressive strength of the plank at 28 days was 50 MPa. The steel reinforcement was galvanised and the clear cover of the reinforcement was 70 mm.

Figure 100 illustrates the design of the precast EFC plank and the layout of reinforcement. Figure 101 shows the process of casting EFC concrete for four planks at one batch within Wagners precast yard A completed plank after 7-day curing is given in Figure 102.

Design of the durability monitoring system

The study aims to monitor the chloride diffusion in EFC and the steel reinforcement corrosion in natural marine environment. An integrated sensing system will be embedded within EFC planks to monitor the rate of corrosion and environmental conditions, including corrosion potential, corrosion current, in-situ pH value of concrete, temperature and relative humidity in the concrete.

The concrete durability monitoring system consists of one Caumur II controller and multiple sensors connected via CAN bus cables. Figure 103 shows the structure of the entire monitoring system. The list of embedded sensors is given in Table 1.

Two monitoring zones are selected based on the design of Westport Boat Ramp Stage 2 Works, as given in Figure 104. Table 2 provides the details of the two monitoring zones.

- Monitoring zone 1 located at the 3rd EFC plank from the lower end of the Northern row in the boat ramp. The zone is expected to be submerged in sea water and wet permanently or most of the time. Sensors will be embedded in a standard EFC plank with wire connections to the controller.
- Monitoring zone 2 located adjacent to the ramp in the middle of the tidal/splash zone. The zone is getting continuously wet and dry with sea water which is the worst possible case for chloride induced reinforcement corrosion. A special EFC element will be cast with sensors embedded. Wire connections are needed between the sensors and the controller. The location of the element will fit into the design of the ramp, either within the edge treatment or a stepping stone.

Figure 99. Site view of Westport boat ramp project at Port Macquarie, NSW.

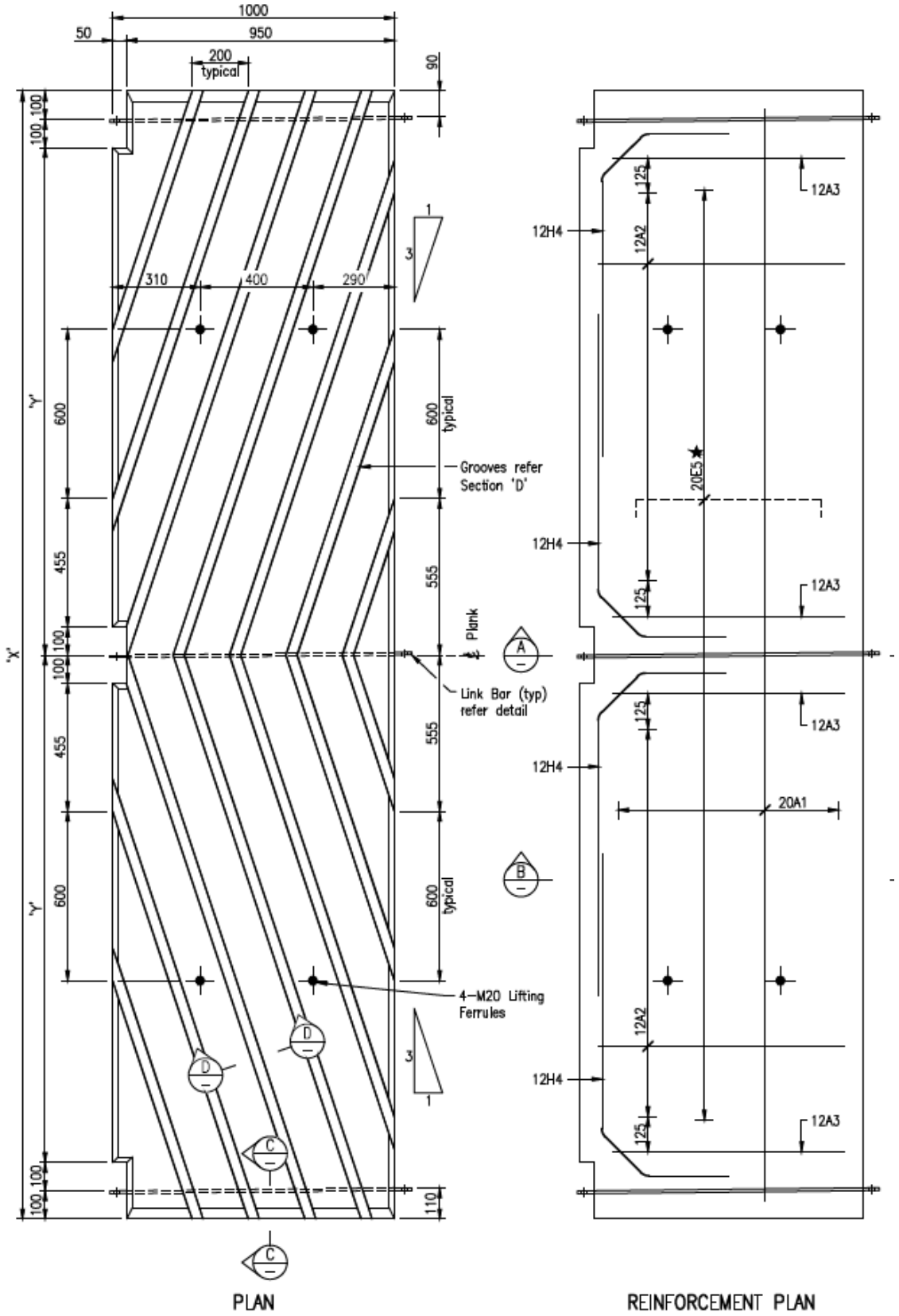

Figure 100. Top views of precast EFC plank and reinforcement (Wagners).

Figure 101. Concrete casting of four boat ramp planks at Wagners precast yard at Wacol, Queensland.

Figure 102. Completed EFC boat ramp plank after curing.

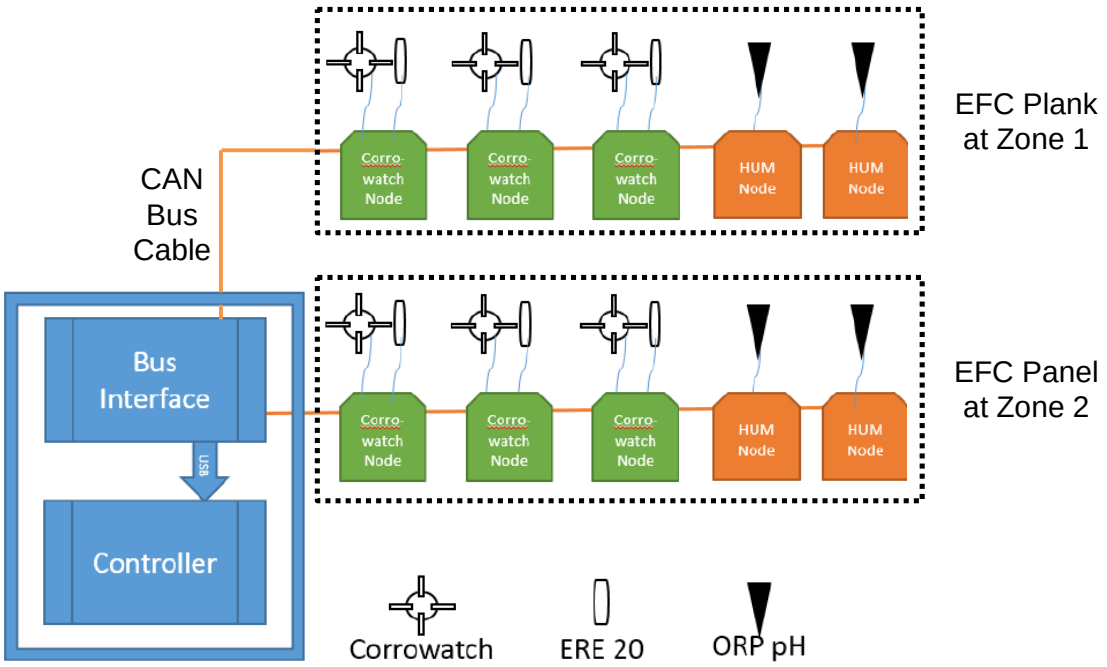

Figure 103. Structure of the Geopolymer concrete durability monitoring system.

Table 18. Embedded sensors used in the Geopolymer concrete durability monitoring system.

Sensor	Number	Location	Dimensions (mm) (Length × Diameter)
Corrowatch	6	Mount on reinforcement bar	55 × Ø85
ERE20 Reference Electrode	6	Mount on the reinforcement bar & close to corrowatch	85 × Ø16
Humidity Sensor	2	Mount with pH sensor	80 × Ø8
pH Probe	4	20 mm & 30 mm deep from surface	220 × Ø25

Table 19. Specifications for the two monitoring zones.

Monitoring Zone	Location	Monitoring Element	Dimensions (mm) (L × W × D)
Zone 1	Submerged in Sea Water	EFC Plank with Reinforcement	4,000 × 1,000 × 200
Zone 2	Tidal/Splash Zone	EFC Panel with Reinforcement	1,000 × 1,000 × 200

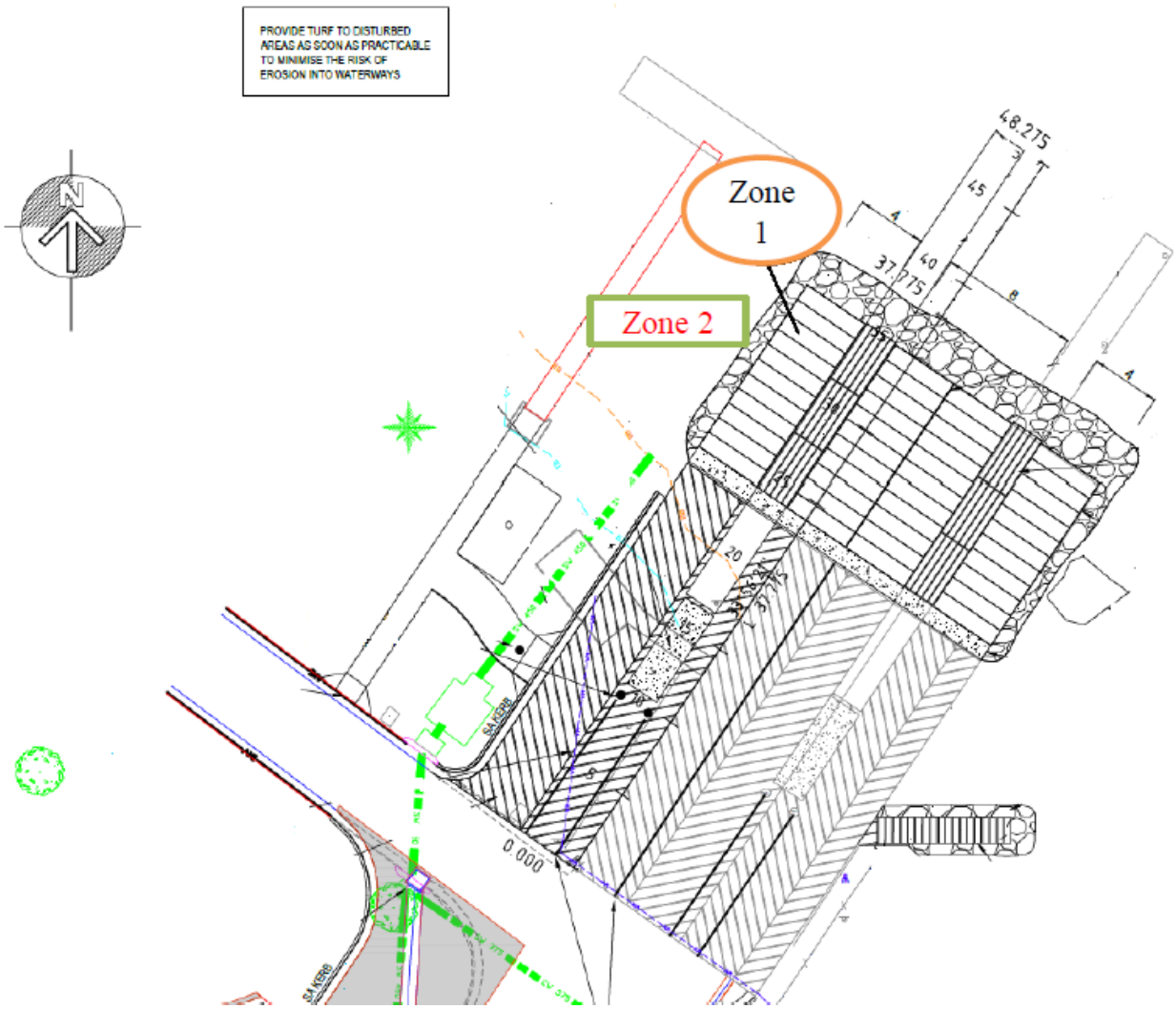

Figure 104. Locations of two monitoring zones at Port Macquarie boat ramp project, NSW.

Corrowatch sensor

The Corrowatch sensor (Figure 105) measures conditions in concrete structures in terms of temperature, current and potential. It works as an early warning system by monitoring the status of corrosion in concrete. The progress of chloride penetration in the concrete as well as steel corrosion will be extensively investigated over time following the procedures established in ASTM-C 876 “Standard Test Method for Corrosion Potentials of Uncoated Reinforcing Steel in Concrete”.

The Corrowatch sensors were mounted on the reinforcement bar in the EFC plank/panel. The sensors were installed at a minimum spacing of 500 mm between each other. Figure 104 shows the locations of the Corrowatch sensors in the EFC plank at Zone 1.

Figure 105. Corrowatch sensor (PCTE).

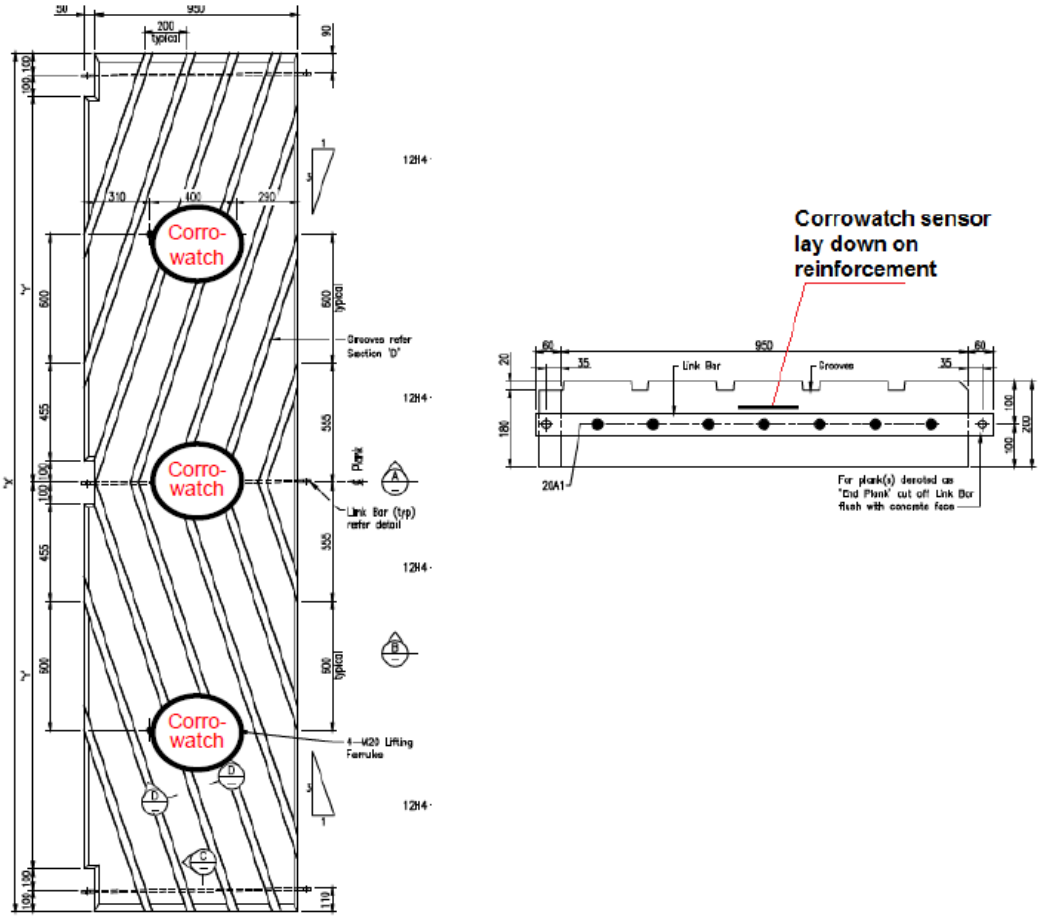

Figure 106. Locations of three Corrowatch sensors in EFC plank at zone 1.

Embeddable Reference Electrode 20 (ERE20)

The ERE 20 reference electrodes (Figure 107) are required for corrosion monitoring by Corrowach sensors. They will be mounted close to the Corrowatch sensors. The potential of ERE 20 is virtually independent of changes in the chemical properties of the concrete. It can be used in wet or dry concrete, whether exposed to chlorides or to carbonation.

Figure 107. ERE20 reference electrode (PCTE).

Humidity sensor

Hygrotemp humidity sensor (Figure 108) can measure the relative humidity at certain depth within the concrete. The humidity information is needed for both monitoring the drying process of EFC and calibrating the pH readings from the pH probe.

Figure 108. Hygrotemp humidity sensor (PCTE).

pH probe

The pH value of concrete is a vital parameter for interpreting steel reinforcement corrosion in concrete. It has been quite challenging to monitor the in-situ pH value of concrete due to high alkalinity condition. The research team at UNSW has successfully developed a new pH monitoring system of Geopolymer concrete in the laboratory, as given in Figure 109. By embedding the pH probe in EFC plank/panel, this project features the very first field trial on continuous pH measurement of Geopolymer concrete.

Figure 109. pH probe and data transmitter system.

Camur II controller and data logger

The Camur II controller (Figure 110) is a small-form-factor field computer capable of communicating with multiple sensors and on-board data storage. Each sensor functions as a node and is connected with the controller using one single CAN bus cable. The concrete corrosion data, such as current of corrosion, humidity potential, pH value etc., are collected and stored in the controller at a pre-defined frequency (e.g. once per hour). Coupled with a 3G/4G wireless modem, the controller can be accessed and programmed from a remote office server in wireless.

Figure 111 shows the sensor installation for one EFC panel at Wagners precast yard at Wacol, QLD. The 1 m × 1 m EFC panel (Figure 112) was cast and transported to the site at Port Macquarie in June 2016.

Figure 110. Caumur II controller (PCTE).

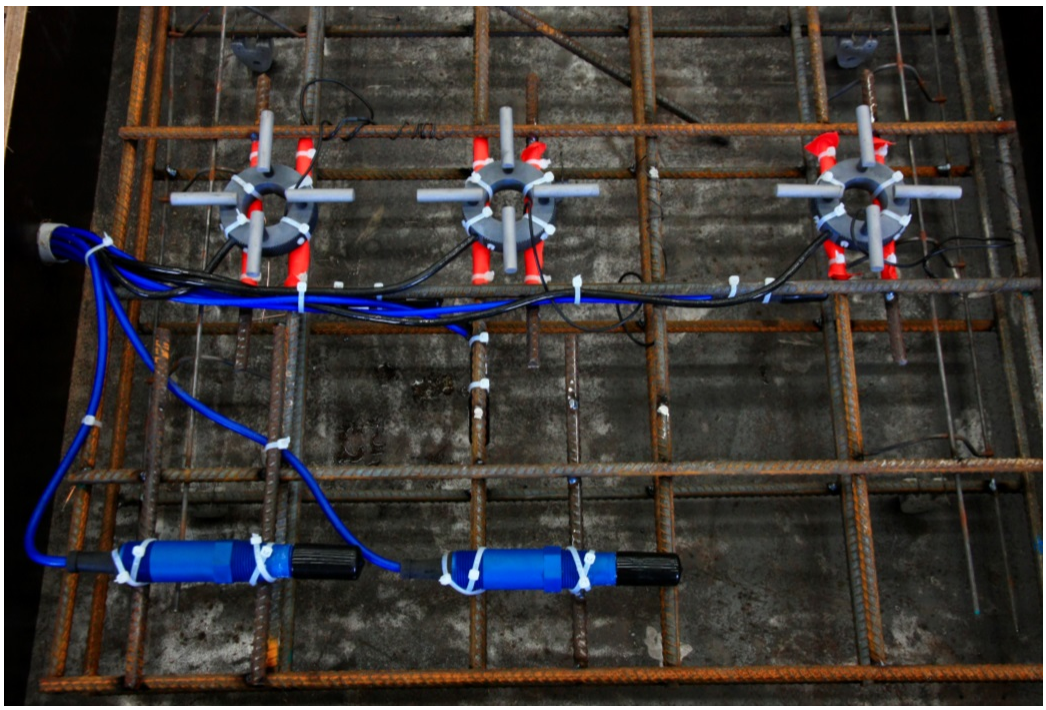

Figure 111. Sensors embedded in one precast EFC panel at Wacol, QLD (June 2016).

Figure 112. Precast EFC panel with sensors embedded at Wacol, QLD, and ready for transport to site (June 2016).

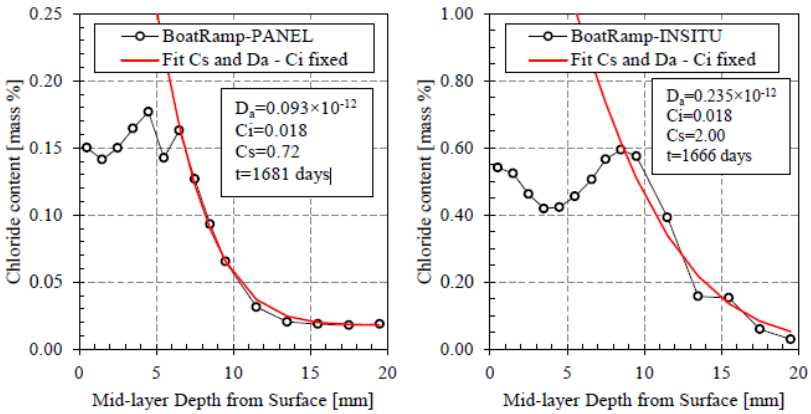

Figure 113. Chloride profiles and chloride diffusion coefficients of the cores sampled in Rocky Point boat ramp

Rocky Point boat ramp QLD

A similar boat ramp manufactured using the same Geopolymer concrete at Rocky Point in the Queensland late 2012 have been tested by sampling cores. After about 56 months of exposure, two cores were sampled: one in an EFC concrete panel and one in the EFC boat ramp plank, both being in the tidal zone. Cores were used to assess the chloride contamination. Concrete powders were sampled every millimetre over 20mm depth in the concrete and the concrete powder were analysed to measure their total chloride content. The chloride penetration profiles obtained were then analysed in order to calculate the chloride diffusion coefficient of EFC concrete. Figure 113 show the chloride profiles and the chloride diffusion coefficients obtained for the two cores.

Results show that the performance of EFC concrete against chloride diffusion is outstanding. The chloride diffusion coefficient measured is drastically lower than the ones measured in the fly Geopolymer and the OPC concrete at Portland site, Victoria exposed to a similar environment for a similar period of time (see Portland site Victoria). At Portland site, the fly ash Geopolymer concrete chloride diffusion coefficient was ranging from $1.15x10^{-12}$ to $1.92x10^{-12}$ and the OPC concrete obtained a chloride diffusion coefficient of $0.45x10^{-12}$. Rocky Point boat ramp EFC concrete chloride diffusion coefficient is ranging from $0.093x10^{-12}$ to $0.235x10^{-12}$.

Conclusions

The monitoring system embedded in the concrete has been successfully installed in the boat ramp site at Westport, Port Macquarie NSW. However, the installation of the solar power supply system has been delayed and is currently in progress. Power supply is required in order to be able collecting continuously test results from the monitoring system in the Boat Ramp. Consequently, no testing results are presented in this report.

Results obtained from Rocky Point boat ramp QLD are promising, showing that EFC concrete performance against chloride diffusion is outstanding.

Biogenic corrosion of Geopolymer mortar at North Head Wastewater Treatment Plant, Manly NSW (UNSW)

Introduction

Concrete is one of the most widely used materials in construction for wastewater treatment, collection and transportation infrastructure. It is susceptible to multi-stage deterioration under highly acidic environment. This results in the degradation of microstructure and performance failure with the passage of time. The main cause of this degradation is the corrosion of concrete due to the in-situ production of sulphuric acid by bacteria. This mechanism is known as bacteriogenic or biogenic corrosion of concrete. This multistage microbially induced concrete corrosion (MICC) results in the reduction of the life span of concrete structures from expected 100 years to 30-50 years and in extreme cases to 10 years [75]. The study being conducted by UNSW Sydney is investigating use of GPC as an alternative to OPC concrete to resist biogenic corrosion at the North Head wastewater treatment plant at Manly, New South Wales, Australia. The early results are reported here.

The effects of the corrosive attack of concrete in sewers can be of the order of several mm per year. Moreover, 20% of the total damage of concrete structures in sewer systems seems to be caused by sulfuric acid or sulphate attack [76]. However, this corrosive attack on concrete is very much dependant on the type of cementitious material used, exposure environment and the microstructure of the system. The development of an accurate and accelerated test procedure is essential to better comprehend the processes and mechanisms involved in all cementitious material. However, to develop such test some additional knowledge is required. This can be achieved by performing some study experiments in *in situ* conditions to determine the biochemical processes and morphological changes taking place in concrete as a result of biodeterioration.

Specimen preparation

Five different mortar specimens were prepared for the *in situ* investigation at North head waste water treatment plant. The first one is low calcium fly ash based Geopolymer mortar (FA-GPm), second was the slag based Geopolymer mortar (Slag-GPm) and the third was sulphate resistant ordinary Portland cement based mortar (SR). All three of them have the same amount of binder and aggregate. In addition to these three, two commercially available mortars were also prepared namely, SweperCoat having calcium aluminate cement as its main binder (CAC) and Miliken Geospray having Geopolymer mortar (MM) for comparative study.

Materials

A low calcium type fly ash (ASTM C 618 Class F) has been used to manufacture the FA-GPm. The source of this FA is Eraring power station in New South Wales, Australia. GGBFS was also used as an aluminosilicate source in both FA-GPm and Slag-GPm. The SR cement (ASTM C 150 Type V) is also used to prepare the mortar specimen. Table 20 represents the chemical composition of these binders using X-ray fluorescence (XRF) analysis. Sydney sand in saturated surface dry (SSD) condition was used as an aggregate having a specific gravity of 2.65 and water absorption of 3.5%. Potable tap water was used for mixing. The CAC and MM mortar specimens does not require the addition of any fine aggregate as they already had the preferred type of aggregate mixed with the binder by the manufacturer in the desired proportion. The CAC mortar has a combination of CA cement with CA aggregate having aggregate to binder ratio of 1.85-2.33.

Mix proportion

The mix design of FA-GPm is derived from the research performed by Noushini et al. [77] with minor modifications and laboratory trial mixes. All three FA-GPm, Slag-GPm and SR cement mortar have the same amount of binder and aggregate. In case of Geopolymer mortars, aluminosilicate binder i.e. FA and GGBFS which is known as supplementary cementitious material (SCM) was used a binder. To activate the binder, an alkaline solution was used having a mixture of sodium hydroxide (NaOH) and sodium silicate (Na_2O_3) solution. The ratio of sodium silicate to sodium hydroxide solution used was set to 2·5:1 (by mass). The NaOH solution was prepared by dissolving sodium hydroxide pellets in water. The concentration of sodium hydroxide solution used is 12 molar (M), which consisted of 480 g of sodium hydroxide pellets per litre of sodium hydroxide solution or 361 g of sodium hydroxide pellets per kg of sodium hydroxide solution. Sydney tap water was used in this study as the solvent to produce the sodium hydroxide solution. Both the alkaline activator solutions were prepared and mixed 24 hours prior to use. The mass ratio of alkaline activator to binder in FA-GPm is kept 0.5 whereas in case of Slag-GPm it is increased to 0.6. The FA-GPm mix consists of 615 kg/m^3 of SCM as binder, having 85% of FA and 15% of GGBFS. The Slag-GPm has 615 kg/m^3 of SCM as binder, having 75% of GGBFS and 25% of FA, whereas SR mortar has 615 kg/m^3 of special purpose (type V) sulphate resistant cement as binder. Table 21 represents the mix proportion of all three type of mortars, which was carried out by mass. For a given GPC, the total mass of water in the mixture is taken as the sum of the mass of water in the sodium silicate solution, the mass of water in the sodium hydroxide solution, and eventually the mass of free water, if any, added to the mixture. The mass of Geopolymer solids is the sum of the mass of SCM, the mass of sodium hydroxide flakes and the mass of sodium silicate solids (i.e. the mass of sodium oxide (Na_2O) and silica (SiO_2) in sodium silicate solution) [77]. Further, the aggregate mass shown in Table 21 is actually under saturated surface dry (SSD) condition.

The technical data sheet of CAC SewperCoat mortar suggests that the water addition must not exceed 0.15 l/kg of dry coat. So, the water content was selected to 0.14 l/kg of CAC binder aggregate mixture. Similarly, Miliken GeoSpray Geopolymer mortar technical data sheet suggests that the w/c ratio must be kept below 0.2. Thus, to get the desired workability and strength it was selected to 0.185.

Table 20. Chemical Composition of FA, Slag and SR Cement Using XRF Analysis

Chemical Oxides	FA (wt. %)	GGBFS (wt. %)	SR Cement (wt. %)
SiO2	66.56	31.52	28.19
Al2O3	22.47	12.22	10.35
Fe_2O_3	3.54	1.14	1.64
CaO	1.64	44.53	51.78
MgO	0.65	4.62	3.47
Na_2O	0.58	0.21	0.2
K_2O	1.75	0.33	0.38
MnO	0.06	0.36	-
P_2O_5	0.11	0.02	-
TiO_2	0.88	1.03	0.71
SO_3	0.1	3.24	2.98
Loss on ignition (LOI)	1.66	0.79	0.39

Table 21. Mix Proportion of FA-GPm, Slag-GPm and SR.

Components	FA-GPm (kg/m^3)	Slag-GPm (kg/m^3)	SR mortar (kg/m^3)
Fine Aggregate	1230	1230	1230
FA	522.75	153.75	-
GGBFS	92.25	461.25	-
SR cement	-	-	615
Sodium hydroxide solution (NaOH)	102.84	87.87	-
Sodium Silicate solution (Na_2SiO_3)	219.7	257.1	-
Free Water	25	25	246
Total Binder (cement or SCM)	615	615	615
Water/binder	0.31	0.36	0.4
Activator/SCM	0.5	0.6	-
Sodium Silicate/Sodium hydroxide (Na_2SiO_3/NaOH)	2.5	2.5	-
Molarity of Sodium hydroxide solution	12M	12M	-

Mixing and curing

All five types of mortars were mixed in Hobart mixer with the following sequence mentioned below. In case of FA-GPm and Slag-GPm, all the SSD condition aggregate and SCM were first dry mixed for 5 min except for GGBFS in FA-GPm to achieve uniform dispersion. After that water and activator ware gradually added and mixed for another 15 minutes. Finally, the slag was introduced in FA-GPm and further mixing was done for 5 minutes. The mixing procedure adopted in case of SR cement mortar was that SSD condition aggregate is dry mixed with binder for 5 minutes, than water was added in the required proportion and mixed for 15 minutes until fresh mortar becomes homogenous. Similarly, same procedure was adopted in CAC SewperCoat mortar. However,

in case of miliken GeoSpray mortar (MM) the geospray was added to water as suggested in technical datasheet.

Three different types of curing techniques were adopted for these mortar specimens. After casting FA-GPm specimen, they were sealed in plastic bag and moved to oven for heat curing. The curing conditions consisted of 75°C temperature for 18 hours. After finishing the heat-curing period, samples were demoulded and stored in a controlled room at a temperature of 23±2°C until the start of the *in situ* experiment. Whereas, the Slag-GPm was cured in such a way that after casting the specimens were covered with the damp cloth and sealed in a plastic bag for 24 hours. After that, the specimens were demoulded and placed in the airtight plastic bags for 7 days. After 7 days in the bag, the specimens were taken out of their bags and placed in the controlled room, at 23±2°C with 50% relative humidity. The OPC based SR cement mortar was water cured after 24h of casting. The specimens were demoulded and placed in lime-saturated water in controlled room at a temperature of 23±2°C. These specimens were removed from water after 14 days and placed in the controlled room having 23±2°C and 50% humidity till the start of the in situ experiment. However, the MM and CAC mortar specimens after casting were covered with damp cloth for 24 hours and demoulded after that. They were kept in the controlled room till the placement of the specimen in site.

Initial observations

Total of 30 cube specimens for each mixed design were prepared for placement in site conditions having 50 mm x 50 mm x 50 mm. Table 22 presents the compressive strength and initial observations carried out before placing these specimens at site. These observations will be helpful for the initial examination of the specimen after removal from the site. This includes the measurement of degradation in terms of loss of mass, change in density, the neutralization depth and by visual inspection. The neutralization depth will be measured using phenol-phthalein indicator and the degradation in cross-section will also be observed.

Specimen assembly for in-situ placement

After specimen preparation, the specimen assembly was proposed through which the specimens were hanged on site. This was the most important step in this experimental study as the assembly must be durable and at the same time easy to handle. First of all the top and bottom surface of the specimens were coated with aluminium foil to avoid multidirectional exposure of specimens. Figure 114 represents the graphical diagram and picture of specimen top and bottom surface sealed for unidirectional exposure.

Next, plastic net having high tensile strength and chemical resistance were cut in such a way, that the specimen completely rest in side and all 6 surfaces are completely covered. For safety purpose, two nets were used for one specimen. Figure 115 represents the net assembly for hanging the specimen with and without the specimen has been placed inside it after sealing their top and bottom with the aluminium foil.

Finally, a hanging assembly was made using a 2 mm durable stainless steel wire with swages to connect them with the top side of net. So to keep wire move freely in a vertical position it is tightened on top of net making a loop and swage it. Considering the site conditions, 1 m long wire was cut for each specimen; after connecting the wire at both ends, the total length remaining was 900 mm. Figure 116 shows the swages on top and bottom of the wire and the total assembly before hanging.

Table 22. Physical properties and observations.

Properties	FA-GPm	Slag-GPm	SR	CAC	MM
Compressive strength (MPa)					
24 hour	44.2	86.8	9.8	26.9	18.8
7 days	46.3	98.7	21.3	38.9	38.4
28 days	46	104.5	42.5	58.3	56.3
Average weight (g)	254.3	285.9	281.4	293.4	277.5
Average dimensions					
Avg. Length (mm)	50.63	50.43	50.49	50.74	50.77
Avg. Width (mm)	50.63	50.28	50.64	50.69	50.7
Avg. Height (mm)	51.37	50.64	50.42	51.45	51.73
Average density (kg/m^3)	1931.2	2226.5	2182.8	2217.2	2084.1

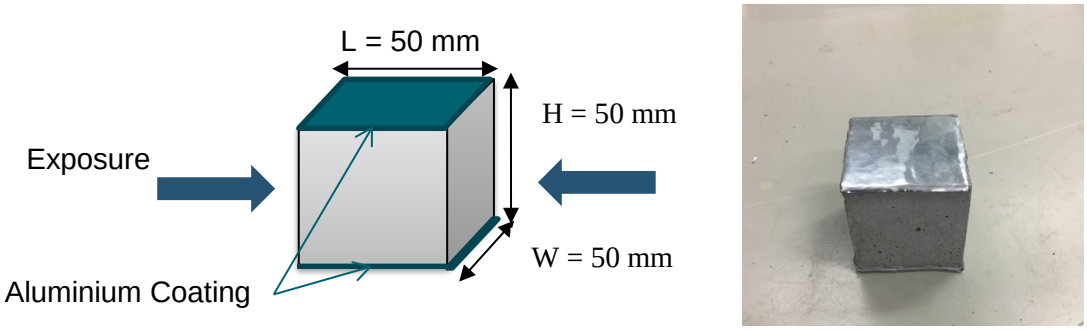

(a) Graphical representation of specimen for exposure.

(b) Specimen with sealed top and bottom.

Figure 114. Specimen before sealing for exposure condition.

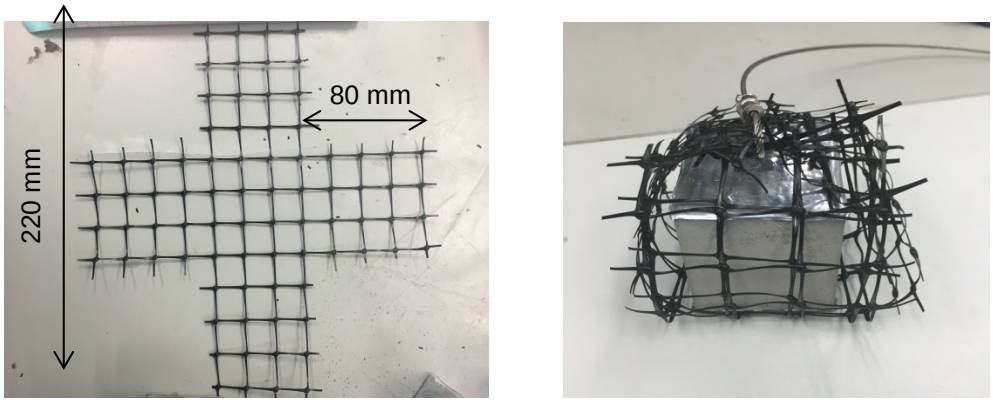

(a) Net used for holding the specimen with dimensions.

(b) After placing the specimen inside the net for hanging.

Figure 115. Specimen with the net assembly for hanging.

(a) Top Swage.

(b) Bottom Swage with specimen.

(c) Specimen hanging.

Figure 116. Specimen with the net assembly ready to be placed on site.

Colours we associated with each mortar consisting of FA-GPm, Slag-GPm, SR, CAC and MM for better identification on site. FA-GPm specimen was noted as 'white', Slag-GPm was given 'Black'. Similarly, SR was given 'Red', CAC 'Blue' and MM was noted as 'Yellow'. So, finally coloured tapes were rolled on the top and bottom swage of each specimen for identification with serial number of the specimen written over it.

FA-GPm

Slag-GPm

SR

CAC

MM

Test setup and site location

To study and perform the corrosion of mortar specimens as a result of biogenic activity an actual sewer environment is required that is aggressive to the specimens and at the same time accessible. North Head waste water treatment plant in manly, Australia is selected for running this test for longer duration.

Figure 117 shows an aerial view of the site locations of North head waste water treatment plant (WWTT) run by Sydney Water. The plant is the second largest WWTT in Sydney and runs 24 hours a day, 7 days a week.

In-Situ conditions

There were actually 3 digesters on site as shown in the aerial view. Figure 118 shows the digesters and the small drain where the specimens were placed on site. The specimens were hanged in all three digester drains for the comparative study. The atmospheric concentration of hydrogen sulphide (H_2S) and temperature was also noted for past 2 weeks just to understand the severity of the environment present inside these digesters. Odalog gas logger was used for this purpose and data was saved at a regular interval of 3 min for 13 days. Figure 119 shows the gas monitoring system placed in the sewage drain of digester.

The sewage data for two weeks before the installation of the specimens confirmed that the amount of sewage is continuously running and there are alternative wet and dry seasons of exposure. Further, the data suggests that digester 2 is more aggressive as compared to 1 and 3 in terms of H_2S concentration. Figure 120 shows the graphical representation of maximum and the average of H_2S concentration for all the three digs from 17 of February to 29 February, 2016.

The atmospheric concentration of H_2S in digester 1 (dig 1) ranges from 0 to 19 ppm; the temperature range was 29 to 33°C. However, dig 2 showed much higher concentration of H_2S ranging from 2 to 345 ppm with same temperature range. Further, dig 3 gave slightly lower concentration of H_2S as compared to 1 with maximum concentration of 9 ppm with almost the same temperature range as others.

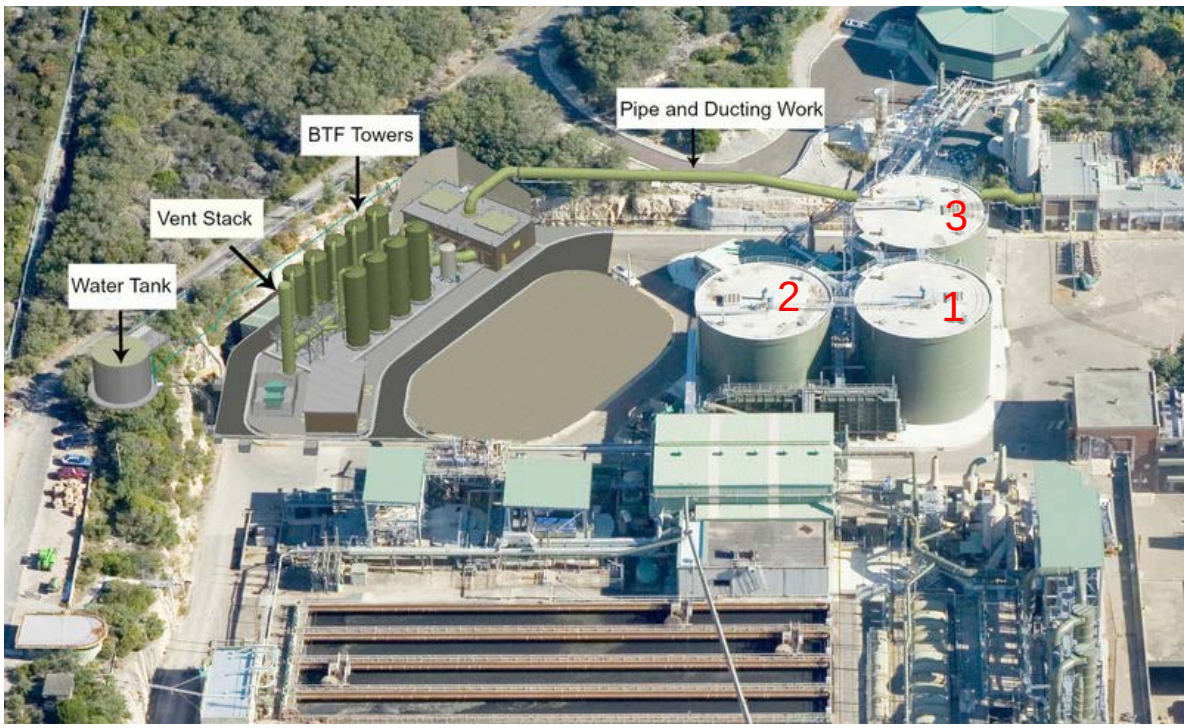

Figure 117. Aerial view of North Head Wastewater Treatment Plant showing digester numbers.

(a) Digesters 1 (left) and 3 (right).

(b) Drain at digester 2 where specimens were placed.

Figure 118. Digesters at site for hanging the specimens.

(a) Odalog Data logger for H_2S and temperature.

(b) Placed inside drain hanging from wire.

Figure 119. Odalog data logger placed inside the drain for measuring the H_2S concentration and temperature.

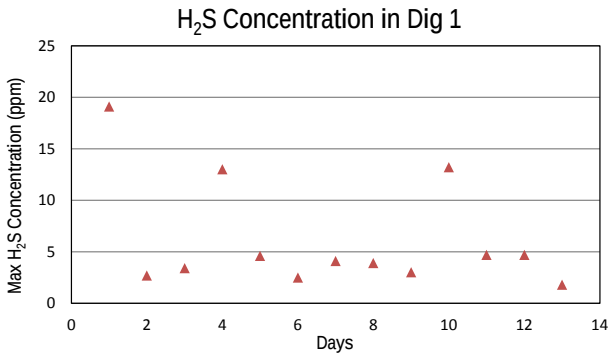

(a) Maximum H_2S concentration in digester 1.

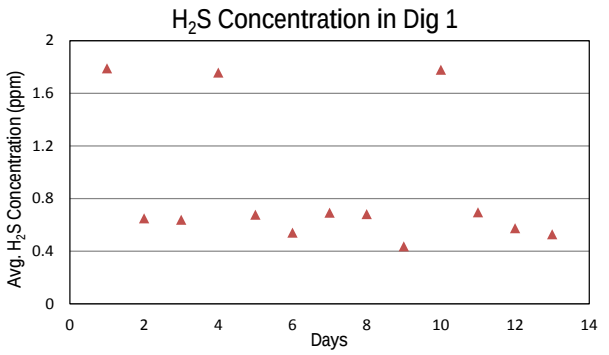

(b) Average H_2S concentration in digester 1.

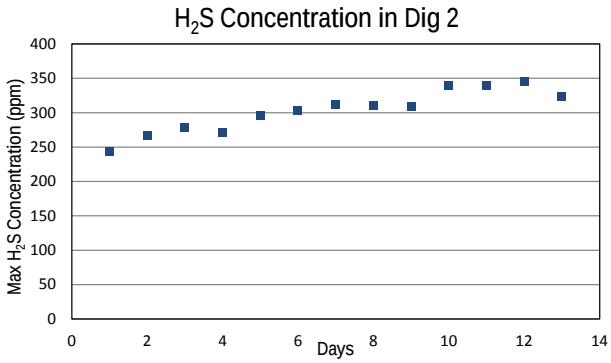

(c) Maximum H_2S concentration in digester 2.

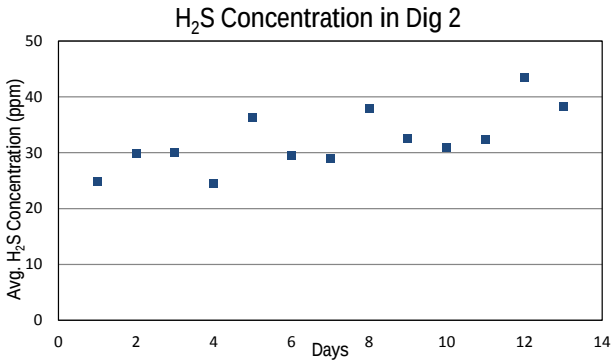

(d) Average H_2S concentration in digester 2.

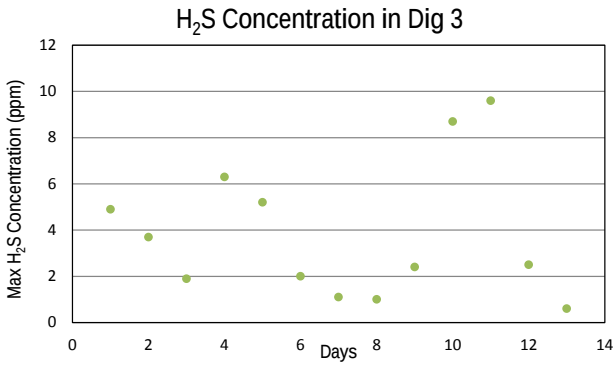

(e) Maximum H_2S concentration in digester 3.

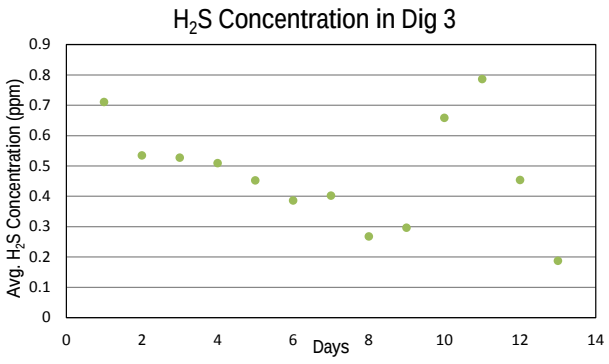

(f) Average H_2S concentration in digester 3.

Figure 120. H_2S Concentration in digester 1, 2 and 3 observed before the start of the experiment.

Specimen assembly and pattern

The specimens were hanged in the drains of digesters 1-3 uniformly in such a way, that in each digester 7 stainless steel wires of 5mm thickness were drilled in the shorter direction of 975 mm within the centre. The distance between each stainless steel wire was kept constant and is equal to 175mm. Similar mortars were placed from left to right in each dig starting from FA-GPm on wire 2, than Slag-GPm, CAC, SR and finally MM on wire 6 towards the right. Similarly, each wire supports only 10 specimens of each type. The digester 1 contains serial # 1 to 10 for each type of mortar specimens, whereas digester 2 contains serial # 11 to 20 and digester 3 contains serial # 21 to 30. Figure 121 shows the hanging pattern of different specimens in digesters 1, 2 and 3.

The coupon samples being tested have been suspended in these tanks where rapid deterioration of the OPC concrete had previously been observed. They are not laboratory conditions.

(a) Specimens Hanging in digester 1.

(b) Specimens hanging in digester 2.

(c) Specimens hanging in digester 3.

Figure 121. Specimens hanging pattern in each digester.

Side observations at the time of specimen assembly and periodic coupon sample removal

The concrete tanks connected to the digesters at North Head, where the specimens were hanged, have H_2S concentrations up to 300 ppm or more. The ordinary concrete had been attacked to a depth of up to approximately 70 mm in a few years according to Sydney Water before being repaired in June 2014 (Figure 122).

Recent inspections of the tanks (taking the coupon samples for periodic testing) showed the Milliken lining was still in good condition with no visible deterioration having been in service for more than 2 years. The performance of the lining compared to the deteriorated OPC concrete substrate is encouraging.

Figure 122. Application of Miliken's mortar (Geospray) to repair the deteriorated surface drain.

Test results and analysis

After timely removal of specimens from the site, initially some visual investigations were performed to observe the degradation of specimen in terms of mass loss and neutralization of depth. Further, penetration of sulphuric acid will be observed using phenolphthalein test. Second phase of testing will include microstructural assessment of mortar specimens using scanning electron microscopy (SEM), energy-dispersive X-Ray spectroscopy (EDX), X-Ray diffraction (XRD), Raman spectroscopy, Fourier transform infrared spectroscopy (FTIR) and nuclear magnetic resonance spectroscopy (NMR) techniques at different penetration depths (Figure 123). These are helpful in assessing the mechanisms underlying the effect of severe environmental conditions on different Geopolymer and cement mortars. Figure 123 represents all the instruments available at the analytical centre, The University of New South Wales which is used for microstructural studies.

This research acts as an optimisation step for laboratory based experimental procedure and provides a comparative study between the in situ experiment and laboratory experimentation.

At 23 August 2016, the first specimen collections were undertaken. At that time the specimens had been exposed under aggressive sewage environment for almost six months. Continuous monitoring of H_2S concentration was carried out to safely remove the specimens. After removing the specimens they were sealed in air tight bags, naming each specimen based on the digester where they were placed, type of the mix and specimen.

After 6 months of exposure, the specimens were almost completely covered in slime and waste water at the time of removal from the digesters. This gives us the first idea that the environment in which they are exposed is environmentally aggressive and suitable for the biogenic corrosion to initiate. Figure 124 shows the specimen condition at time of removal.

The data of long term temperature and H_2S gas measurements showed average concentrations of around 13.7, 20.1 and 10.5 ppm in digesters 1, 2 and 3 respectively, over the period of 6 months. In all 3 digesters, due to wetting and drying cycles of daily maximum H2S concentrations was ranging from 2.2 to 388 ppm, 0 to 477 ppm and 0 to 575 ppm, respectively, as shown in Figure 125. Green stars (A-E) mark important H2S thresholds for human beings, such as odour threshold (A), eye irritation and headache (B), severe damages of eyes and respiratory systems (C), emerging odourless for human beings (D) and possible death (E) [78]. Figure 126, represents the change in average daily temperature throughout 6 months which varies from 33.5 to 12.7°C in all the three digesters. Average daytime H2S concentration varies from time of the day and active digester with maximum of around 54, 102 and 36 ppm reported respectively, which is sufficient to maintain the corrosive environment, far exceeding the concentration (10 ppm) required to sustain sulphuric acid generation.

Attack by biogenic sulphuric acid comprises the dissolution of cementitious phases because of acid–base reaction with H+, and the formation of sulphate-bearing secondary products, ettringite, and/or gypsum. The simplified reaction of portlandite $Ca(OH)_2$ and C-S-H gel with an acid attack in Portland cement matrix is shown below, which results in the dissolution of these main hydrates [79].

$$Ca(OH)_2 + 2H^+ \rightarrow Ca^{2+} + 2H_2O$$

$$3CaO.2SiO_2.3H_2O + 6H^+ \rightarrow 3Ca^{2+} + 2Si(OH)_4 + 2H_2O$$

For OPC pastes, the reaction of portlandite and C-S-H with sulphate forms gypsum ($CaSO_4.2H_2O$). Ettringite

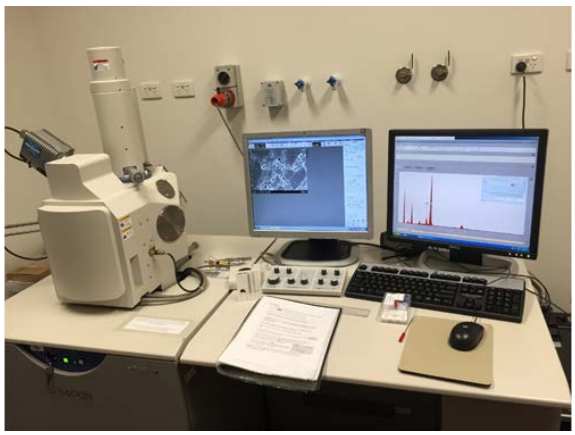

(a) SEM/EDX.

(b) NMR spectroscopy.

(c) Raman spectroscopy.

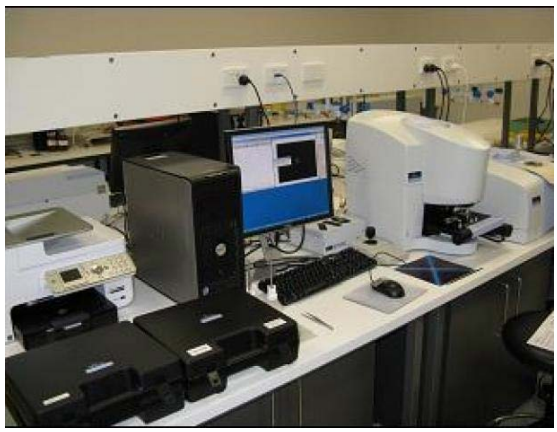

(d) FTIR spectroscopy.

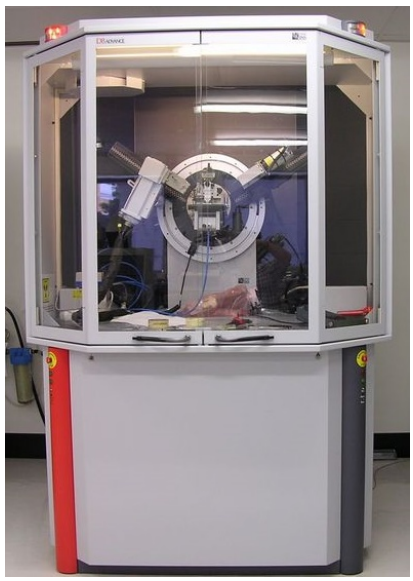

(e) XRD spectroscopy.

Figure 123. Instruments for microstructural assessment of concrete mortars.

Figure 124. Specimens at the time of removal from digesters.

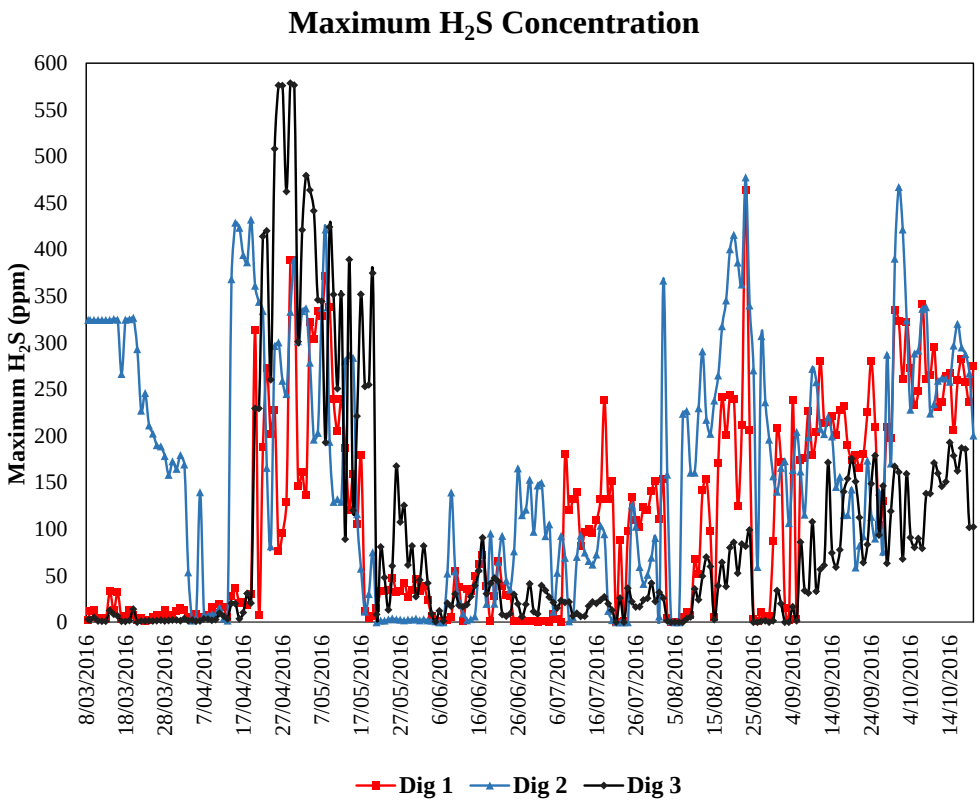

Figure 125. Maximum H_2S concentration in each digester from start of experiment.

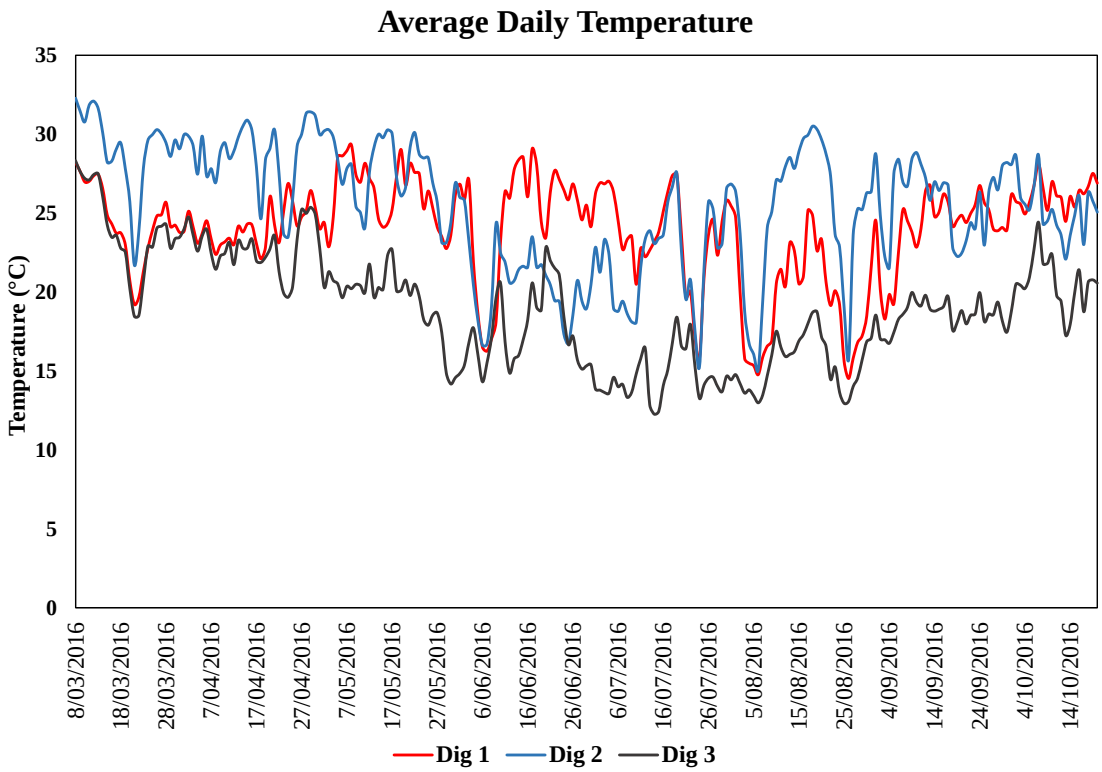

Figure 126. Average daily temperature from start of experiment.

($3CaO.Al_2O_3.3CaSO_4.32H_2O$) is formed through the reaction of gypsum with C_3A or with monosulfoaluminate as shown below:

$$Ca(OH)_2 + SO_4^{2-} + 2H_2O \rightarrow CaSO_4.2H_2O$$
$$3CaO.2SiO_2.3H_2O + 3SO_4^{2-} + 2H_2O \rightarrow CaSO_4.2H_2O + Si(OH)_4$$
$$3CaO.Al_2O_3 + 3CaSO_4.2H_2O + 26H_2O \rightarrow 3CaO.Al_2O_3.3CaSO_4.32H_2O$$
$$3CaO.Al_2O_3.CaSO_4.12H_2O + 2CaSO_4.2H_2O + 16H_2O \rightarrow 3CaO.Al_2O_3.3CaSO_4.32H_2O$$

The mineralogical and chemical changes of CAC-based materials following the attack by sulphuric acid are not very well documented. For CAC-based matrices, the dissolution of calcium aluminate hydrate, C_3AH_6 and C_2AH_8, led to the formation of aluminumhydroxide or gibbsite (AH_3) which dissolves as pH < 4 [80], as shown below:

$$3CaO.Al_2O_3.6H_2O + 6H^+ \rightarrow 3Ca^{2+} + 2Al(OH)_3 + 6H_2O$$
$$2CaO.Al_2O_3.8H_2O + 3SO_4^{2-} \rightarrow 2CaSO_4.2H_2O + 2Al(OH)_3 + H_2O$$
$$3CaO.Al_2O_3.6H_2O + 3CaSO_4 + 26H_2O \rightarrow 3CaO.Al_2O_3.3CaSO_4.32H_2O$$

Visual observations

The visual assessment of all types of mortar from the three digesters included observation of colour changes, cracking and crazing. After six months of exposure most of the specimens presented with white brownish spots on the surface, as shown in Figure 127. To investigate the x-section of 50 mm cube specimens, they were cut from the surface of the exposure till the other end parallel to the coated top and bottom surface. Figure 128 represents cross-section of the digester 1, 2 and 3 mortar specimens, respectively, immediately after splitting the specimens and without applying any phenolphthalein or any other indicator.

No major signs of physical deterioration such as cracks, or spalling were observed on the surface of the samples. However, major colour changes were observed in all specimens except FA based Geopolymer mortar specimens at the exterior exposed surface. As carbonation was the first step in the degradation of concrete when exposed to MICC [81], as a result calcite is formed in those mortars having high percentage of calcium oxide especially at the exposed regions leading to this change in colour.

Similarly, in digesters 2 and 3 all the specimens except FA-GPM showed some colour changes on the exposed surface and owing to the carbonation of these materials, as observed in X-Ray Diffraction (XRD) and pH profile of the specimens. This extent of colour change can also depend upon the atmospheric conditions of the digesters and the location of these materials in each digester. Further, investigations will be reported in section 8.5 in order to determine the origin of colour change.

Change of mass

Specimen weight was measured after drying in an oven for one hour at 50°C. The change in weight was estimated by comparing it with the initial weight of the specimen measured 28 days after casting. Figure 129 (a) to (e) represents the percentage of mass change of all the specimens in digesters 1, 2 and 3. After six months of exposure some of the specimen showed a few per cent of gain in mass. The mass increase is very

variable depending on specimens. For example, slag based GPM gained very little weight, around 0.2%, as compared to MM that gained more than 2.4%. This was most likely due to the uptake of water and organic matter present in sewage which might have penetrated inside the microstructure. An exposure time of six months is too short to observe any significant a difference between the different samples, and the experiment is on-going. SR mortar specimens are the only one showing a mass reduction.

6 months Exposure	FA – GPM	Slag – GPM	CAC	MM	SR
Dig – 1					
Dig – 2					
Dig – 3					

Figure 127. Visual observations of specimens exposed for 6 months to the different digesters.

6 months Exposure	FA-GPM	Slag-GPM	CAC	MM	SR
Dig – 1					
Dig – 2					
Dig – 3					

Figure 128. Cross-Section of specimens exposed for six months to the different digesters.

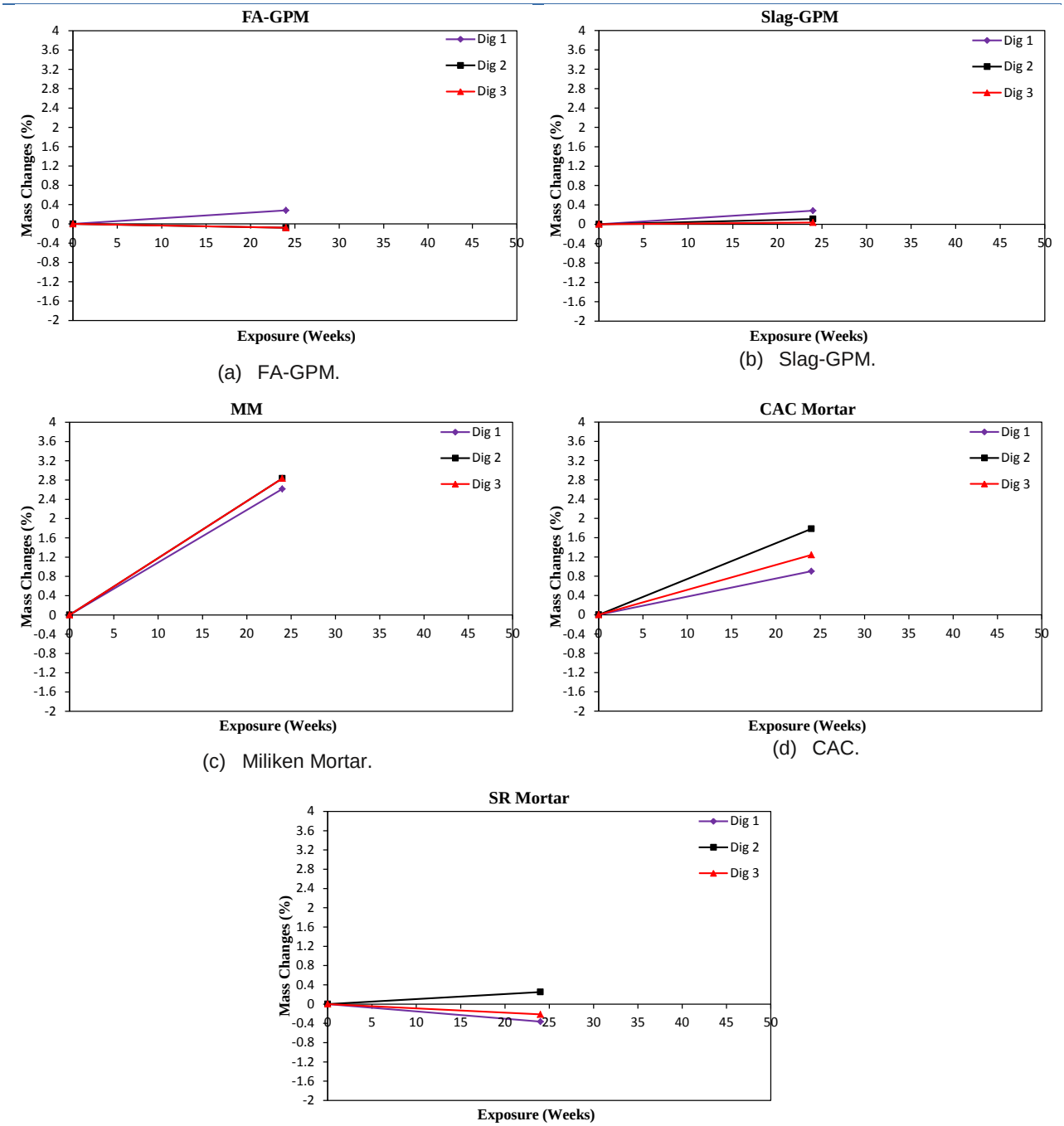

(a) FA-GPM.

(b) Slag-GPM.

(c) Miliken Mortar.

(d) CAC.

(e) SR Mortar.

Figure 129. Mass changes observed after six months of exposure.

Neutralization depth

Phenolphthalein indicator was used to monitor the depth of neutralization of the mortars. The usual method of studying reactions associated with changes in pH is to measure the depth of neutralization as indicated by a 1% phenolphthalein solution, which has been sprayed onto the freshly fractured mortar surface [82, 83]. This indicator shows a magenta coloured region on the concrete where the pH value exceeds about 9.0 and a colourless region at the originally exposed surface where in the result of reaction with acid, the pH was reduced to below 9.0.

Figure 130 shows the coloured, partially coloured and colourless (neutralized) regions after spraying the 1% phenolphthalein solution on the freshly fractured mortar surface of all specimens. OPC concrete usually displays a clear border between the coloured and colourless zone when sprayed with phenolphthalein indicator and a very narrow partially coloured region.

6 months Exposure	Dig – 1	Dig – 2	Dig – 3
FA-GPM			
Slag-GPM	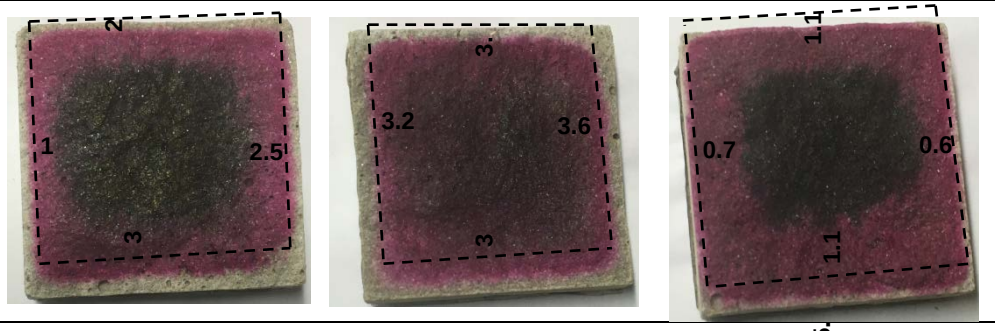		
CAC	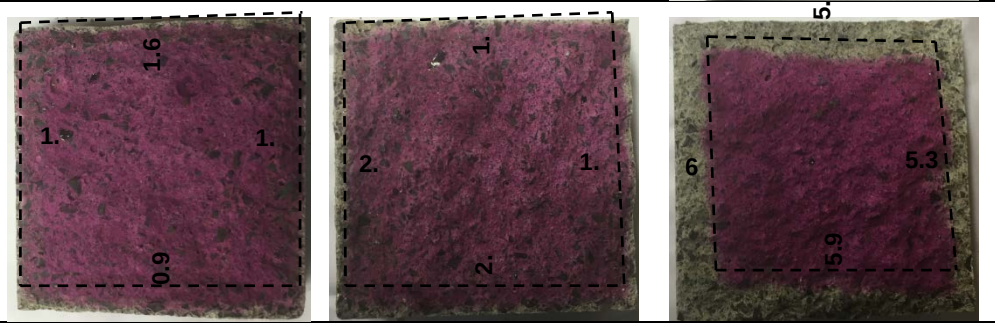		
MM	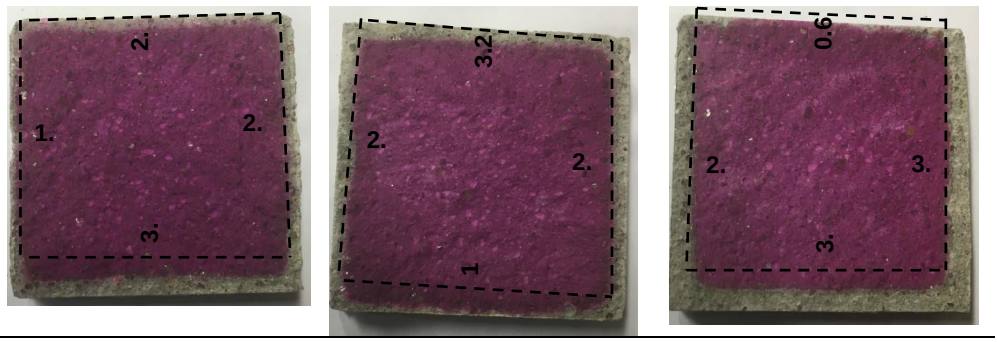		
SR	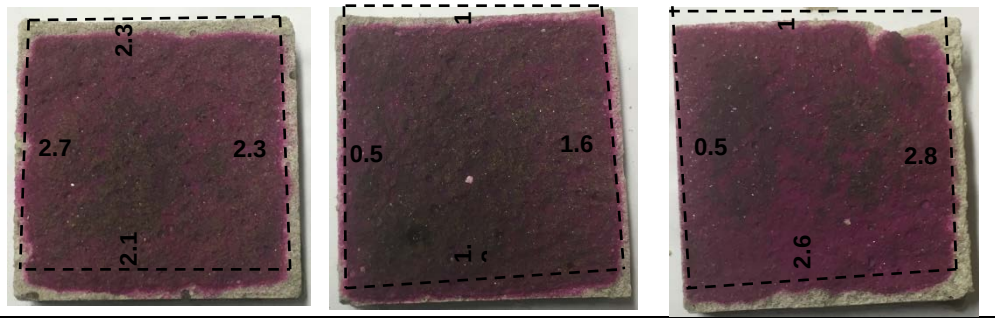		

Figure 130. Neutralization depth after six months of exposure.

In case of FA-GPM, the faded region was scattered through the depth, especially in digester 1 and 3 specimens. The results are further compared with the pH profile confirming that the region is only partially neutralised. The colourless depth was measured at 3 locations and taken as the average value on each face.

pH profiles

As discussed earlier, MICC is a three staged degradation process. Stage 1 of the corrosion process is abiotic lowering of the concrete surface pH. For concrete pipes and tanks, this can occur with the abiotic processes as proposed by Islander et al. [84], including carbonation and exposure to waste water. In general, the carbonation actually occurs on the surface of the concrete lowering the surface pH. Carbonation in this context only needs to occur on the surface of the concrete to initiate the growth of bacteria. The succession of Thiobacillus bacteria species represents stage 2 with or without H2S. The rate of pH reduction during this phase depends upon the concentration of H2S gas in the environment irrespective of the mixed design. After stage 2, the pH of the concrete is reduced to such a level that it becomes susceptible to acid attack. During this stage 3, major corrosion of concrete takes place. Figure 131, represents the loss of pH of Portland cement concrete as a result of different stages of MICC.

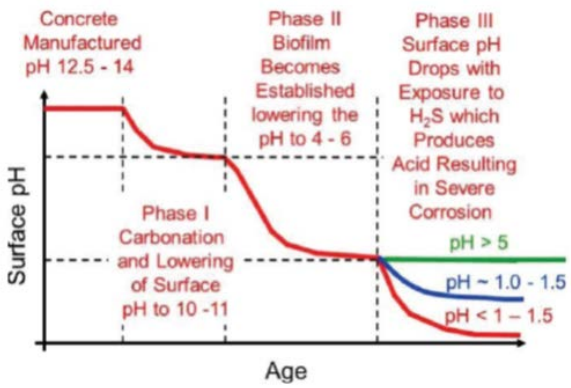

Figure 131. Stages of corrosion in concrete during MICC.

As a result pH of the specimen was investigated by water extraction method [11], concrete powder was sampled after an interval of 2.5 mm using cutter and grinder. The powder was mixed with de-ionized water with the solid to the liquid ratio of 1:1 and the pH of the solution was measured using pH probe. Figure 132, represents the pH values of all five mix designs before they were placed in digesters and pH profiles after six months of exposure. The initial pH values of FA-GPM, Slag-GPM, CAC, MM and SR mortar observed before placing them in digesters were 11.9, 13.1, 11.8, 12.8 and 12.7 respectively.

The pH profile of each mixed design confirms that carbonation is in progress especially on the exterior surface moving towards the centre, as observed in phenolphthalein test. This confirms that all the specimens are under phase I of corrosion i.e. the lowering of the pH to facilitate the growth of Thiobacillus bacteria. However, due to the high concentration of H_2S gas observed in these digesters, sulphide content is abundant, which can trigger and accelerate the corrosion process. Further, due to the high sulphide concentration, the oxidation of which results in the gypsum and ettringite formation in mortars having high calcium (see XRD results). This results in deterioration and cracking especially on the exterior region as observed using SEM.

X-ray diffraction

XRD was conducted on the specimens to identify the products formed after six months exposure to the aggressive sewage environment. Samples were collected from the surface of the cube till the depth of 15 mm at an interval of 2.5 mm for XRD analysis. The mortar samples were ground to powder, and the powders were analysed using a Phillips X'Pert Pro Multipurpose Diffractometer housed at the Mark Wainwright Analytical Centre at the University of New South Wales, Sydney, using Cu–Kα radiation with a wavelength of 0·15418 nm, operated at 45 kV and 40 mA, and with a scan range of 5–70° and 0·026° 2θ step size. The scan results were interpreted using the software package High Score Plus for phase identification, which has a built-in database to match the peak positions and find out the phases and chemical composition of the powders.

Figure 133 (a) to (e) represents the unexposed and exposed XRD pattern of FA-GPM, Slag-GPM, CAC, MM and SR mortar at various depth locations. The FA-GPM was made from 85% Fly Ash blended with 15% Slag activated with sodium silicate and 12 M sodium hydroxide solution after heat curing of 18 hours at 75°C. The main phases observed were amorphous N-(C)-A-S-H indicated by a broad hump between 25-30°, crystalline quartz (Q) and mullite (M). Mullite comes from the residual fly ash used in making the Geopolymer mortar. Natron (N) was also observed in the reference specimen due to some carbonation in the initial specimens which was also observed in the specimen after exposure to sewage environment for six months as observed by Khan et al. [11]. In addition, a very small peak of gypsum was also observed only in Dig-I specimen at 2.5 mm only which suggested that some sulphate has also reacted. Beside that some Feldspar and Albite is also observed after exposure which might be because of the exposed environment. Unlike Portland cement systems, no ettringite and brucite was detected, and this is consistent with the low Ca/Si ratio of these systems.

The Slag-GPM was made from 75% ground granulated blast furnace slag blended with 25% fly ash activated with sodium silicate and 12 molar sodium hydroxide solution cured under ambient conditions of 50% relative humidity and 25°C room temperature for 28 days. The main phases observed were poorly crystalline calcium silicate hydrate (C-S-H), Quartz (Q) and Calcite (C) as a result of carbonation under natural conditions for 6 months. Beside, that some traces of akermanite (Ak) and Gismondine (Gis) are also identified as remnant crystalline phases of slag particles. The formation of these in alkali activated binders is consistent with the literature [85]. However, Gypsum (G) was only observed on the 2.5 mm deep specimen in both digesters 1 and 2.

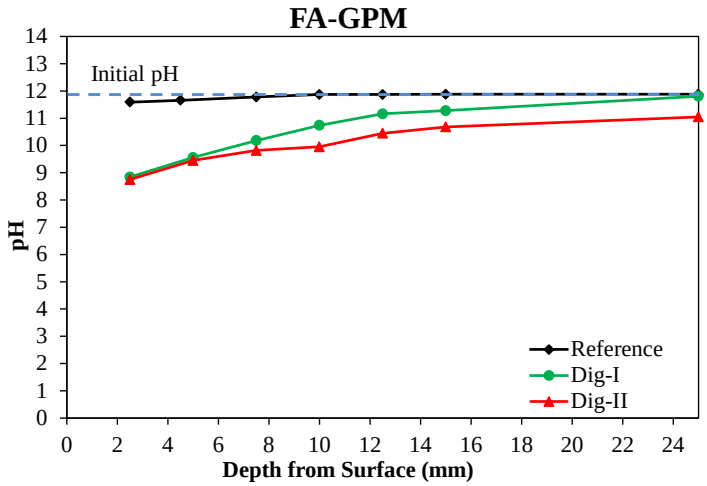

(a) pH profile of FA-GPM.

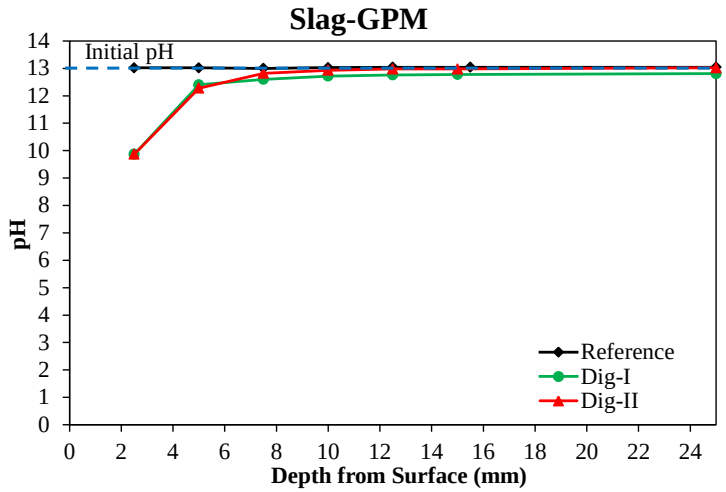

(b) pH profile of Slag-GPM.

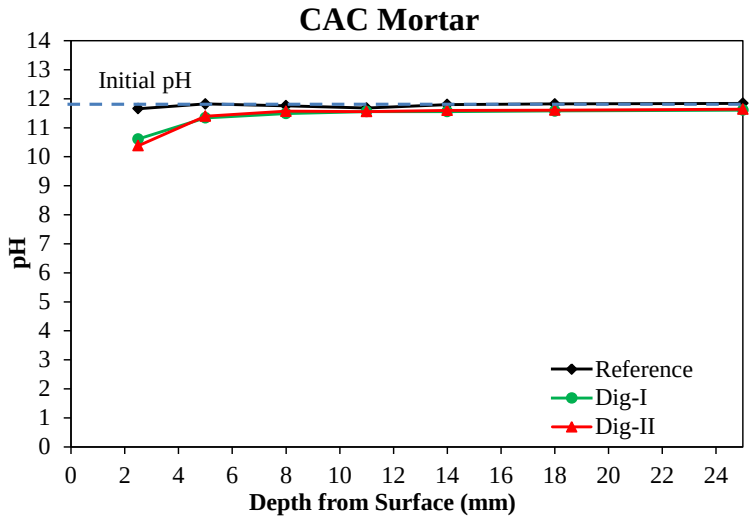

(c)pH profile of CAC.

Figure 132. pH profile after six months of exposure: (a) FA-GPM; (b) Slag-GPM; (c) CAC; (d) MM; and (e) SRM.

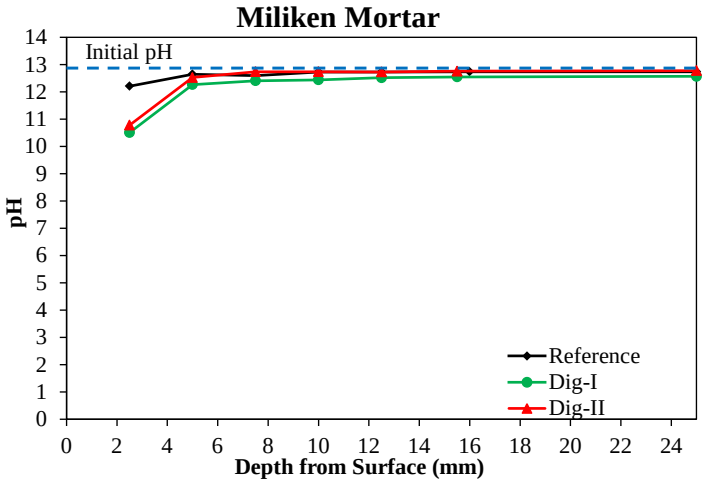

(d) pH profile of MM.

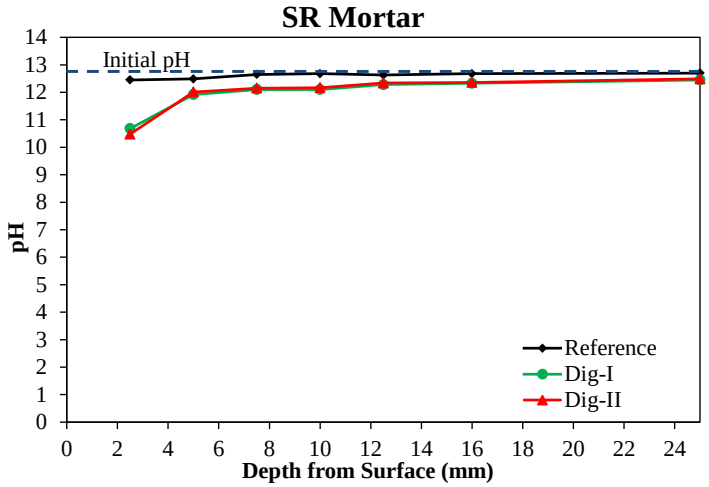

(e)pH profile of SR Mortar.

Figure 132 (continued).

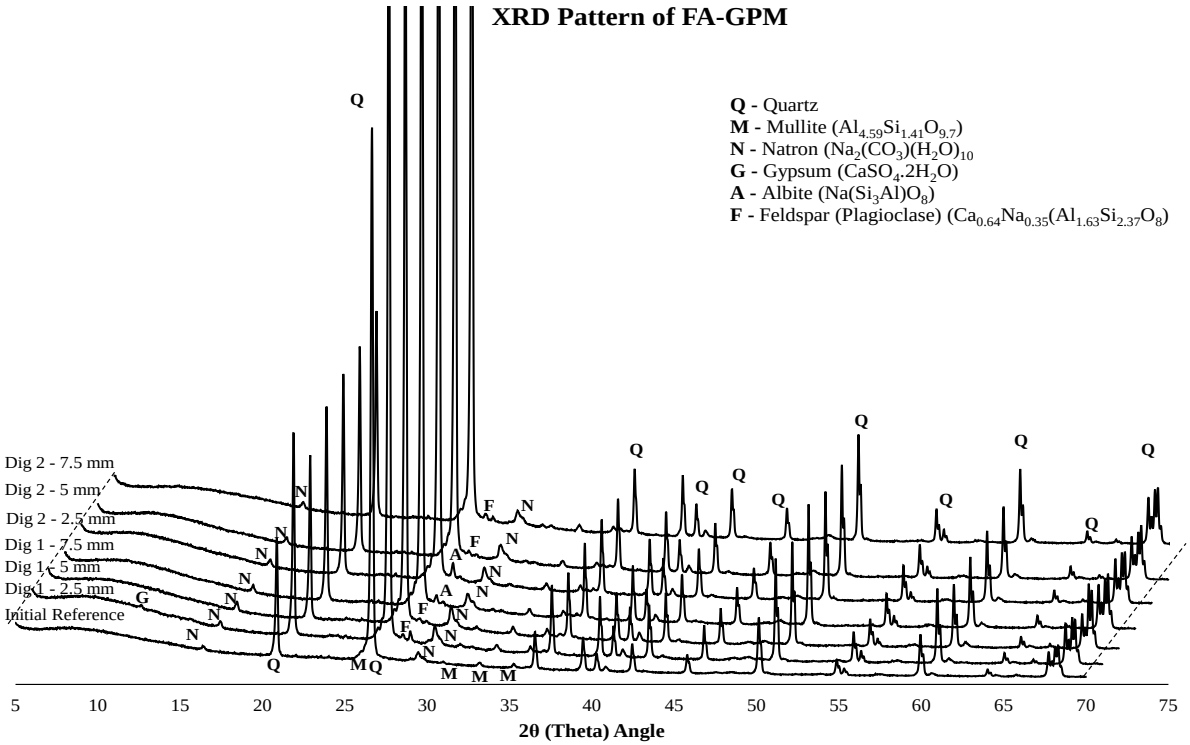

(a) XRD Pattern for FA-GPM.

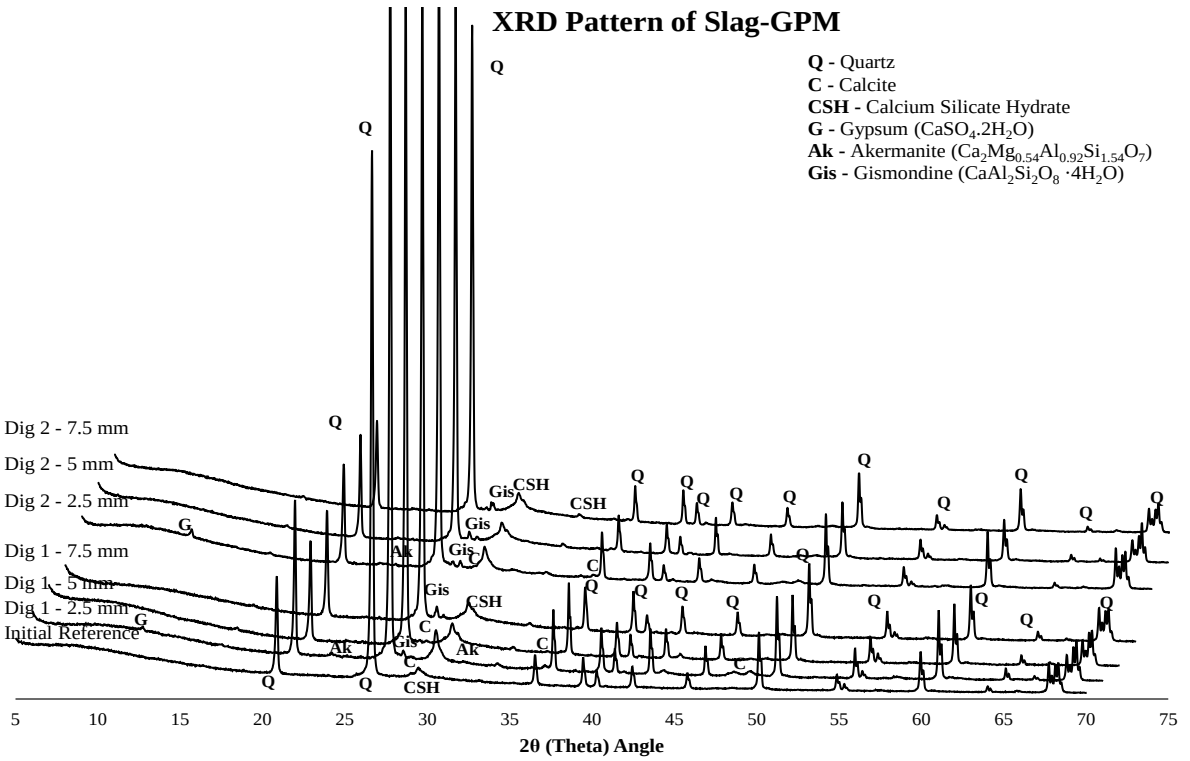

(b) XRD Pattern fornSlag-GPM.

Figure 133. XRD Patterns: (a) FA-GPM; (b)Slag-GPM; (c) CAC; (d) MM; and (e) SR mortar.

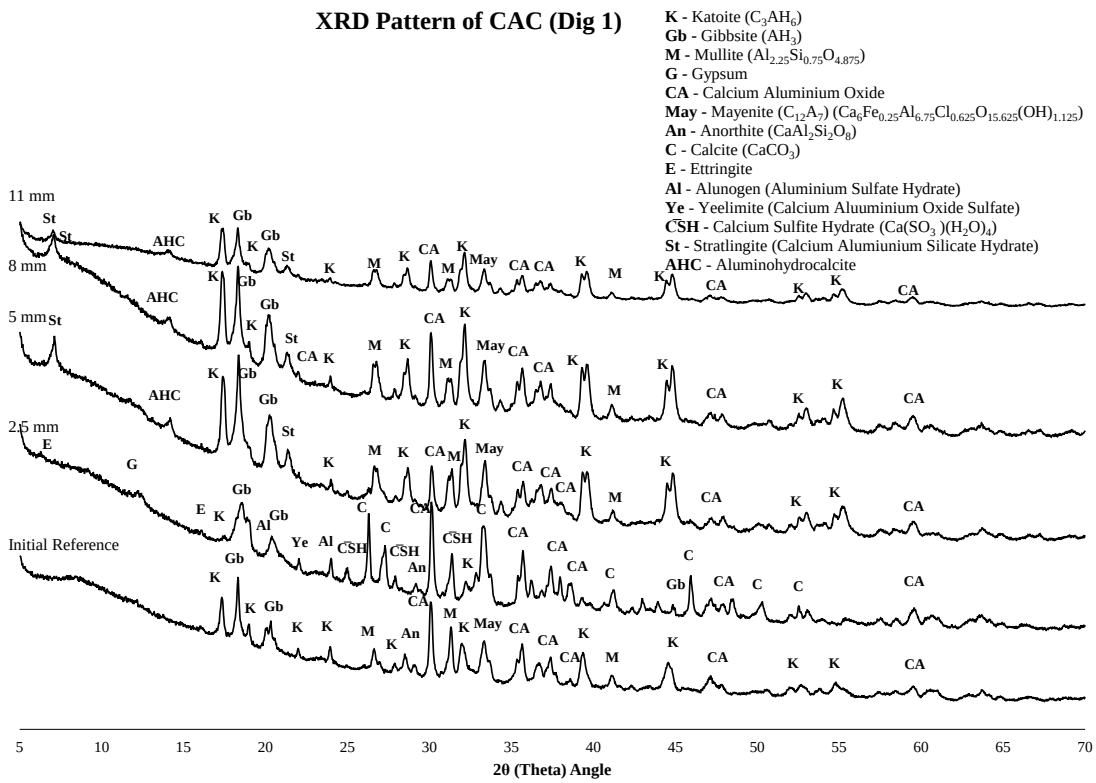

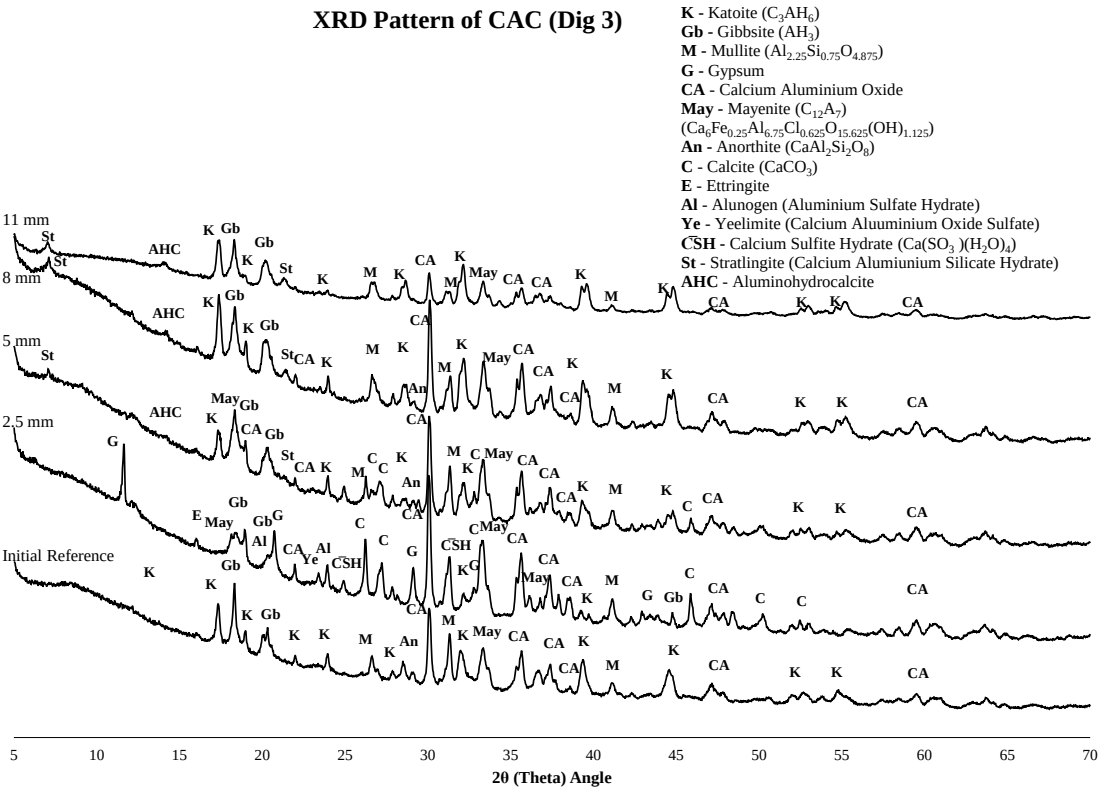

(c) XRD pattern for CAC.

Figure 133 (continued).

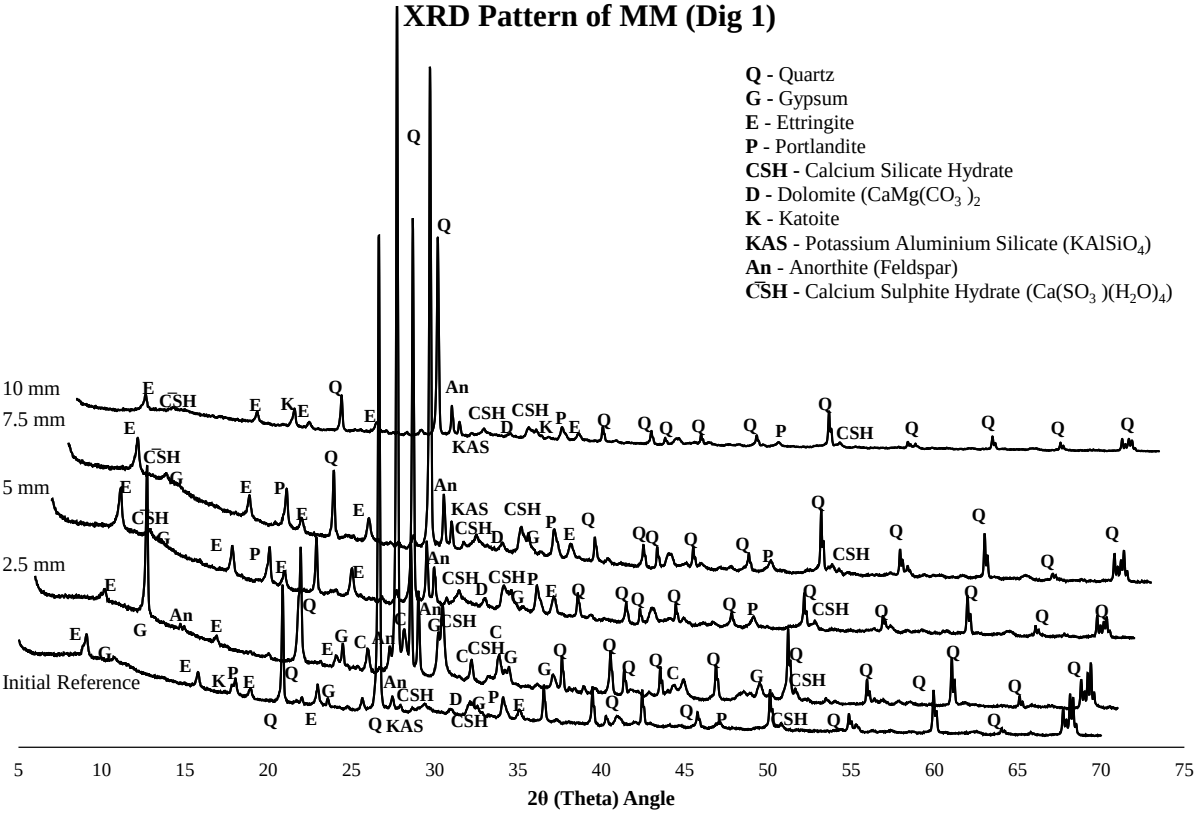

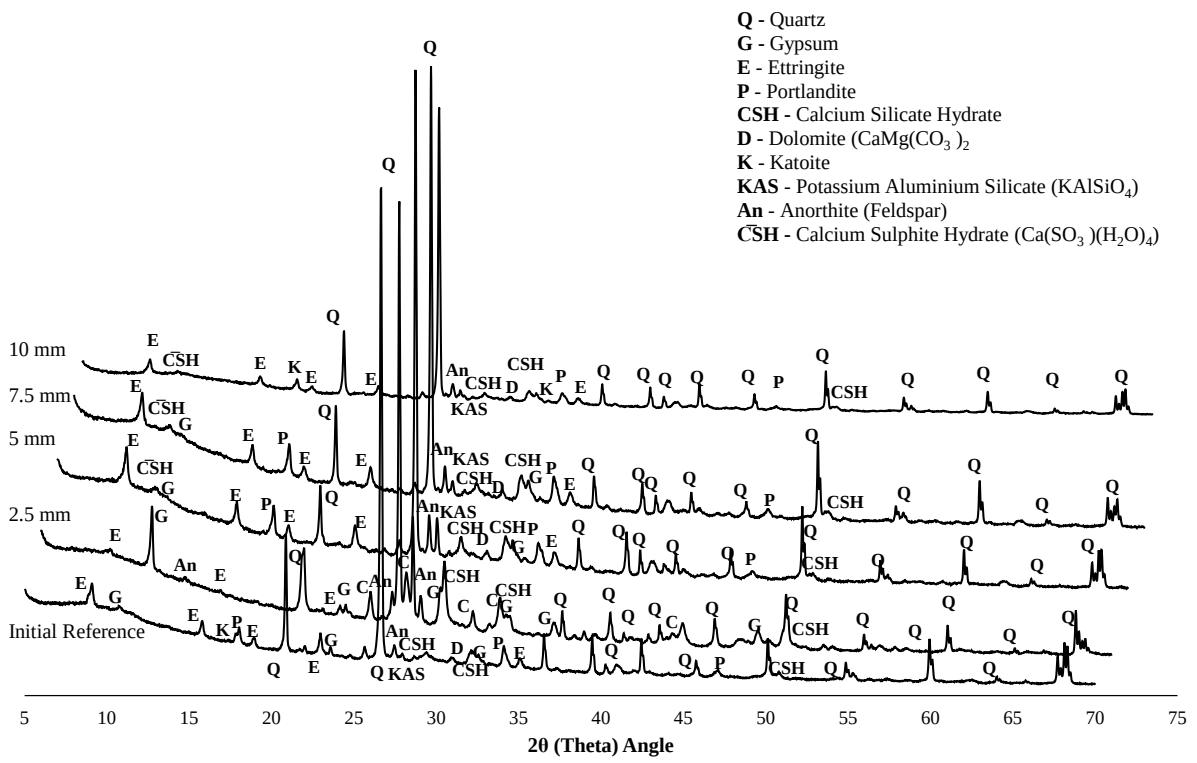

(d) XRD pattern for MM.

Figure 133 (continued).

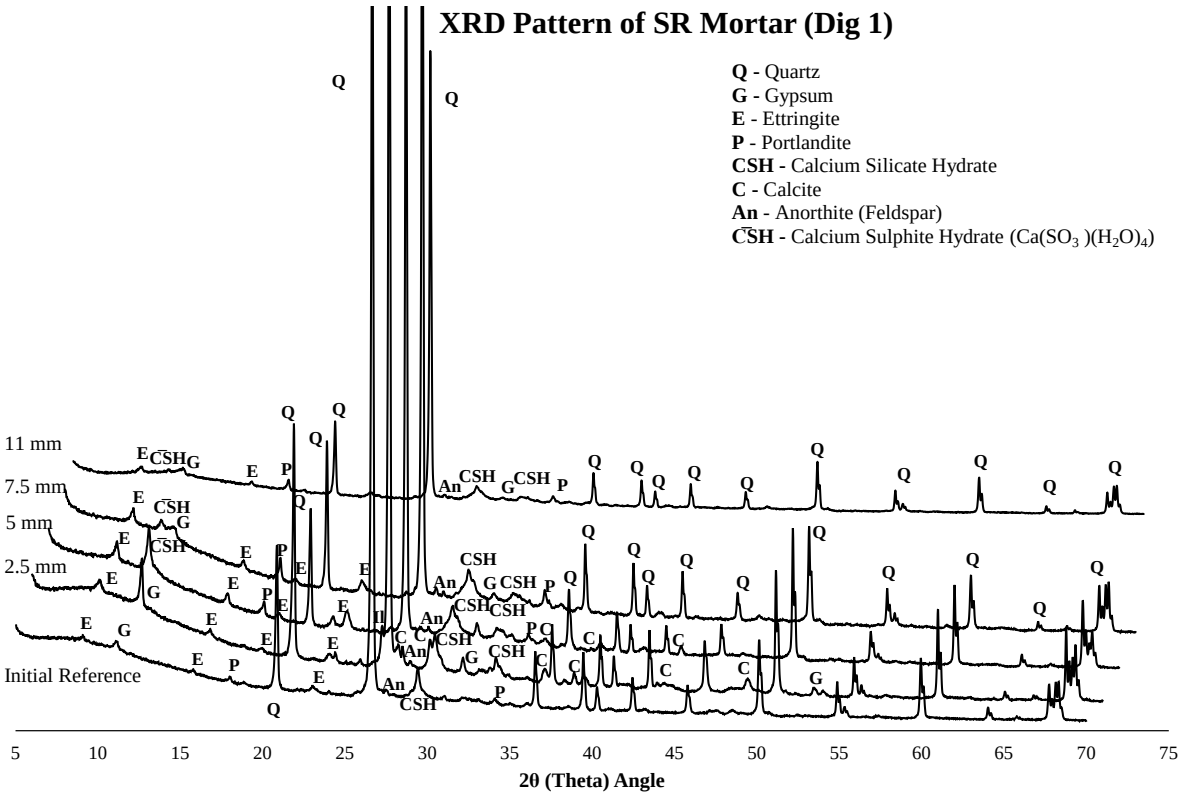

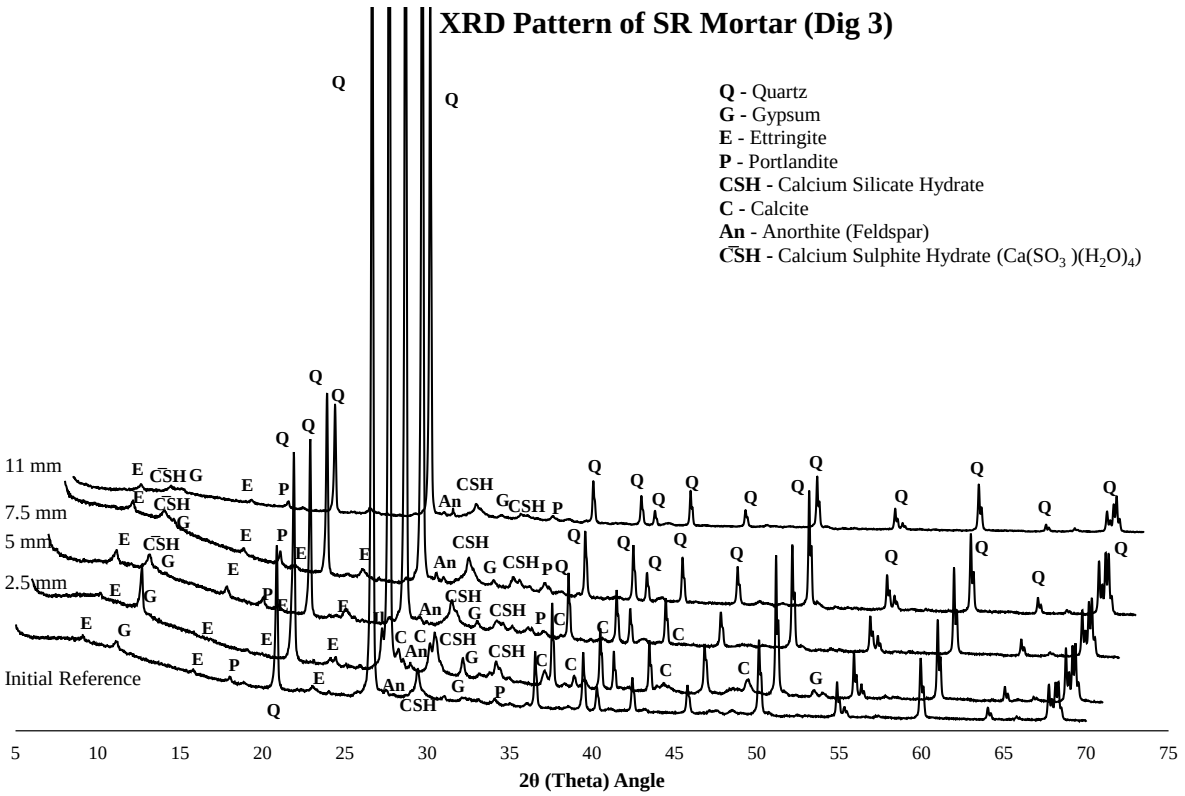

(e) XRD pattern for SR mortar.

Figure 133 (continued).

The main phases observed in CAC before exposure to sewage environment include Aluminium Hydroxide (AH_3) gel also known as gibbsite (Gb), katoite C_3AH_6 (K), Calcium aluminium oxide (CA), mullite (M) and Mayenite $C_{12}A_7$ (May) [79]. However, after exposure to this aggressive environment beside carbonation some sulphate also reacted with the phases observed in the microstructure leading to some Gypsum (G), Ettringite (E), calcium sulphite hydrate ($C\bar{S}H$), Calcite (C), Calcium aluminium oxide sulphate Yeelimite (Ye) and Aluminium Sulphate hydrates (Al) formation. Some traces of other crystalline structures were also observed which include Anorthite (An) and Aluminohydrocalcite (AHC) after the exposure. Instead of ettringite and Gypsum, calcium aluminium silicate hydrate also known as stratlingite (St) was also observed showing maximum peak at 5 mm. In addition, it was observed that katoite was dissociated and consumed on the exterior specimen up to 2.5 mm as a result of gypsum formation in the high sulphate environment. This reaction is more profound in digester 3, as compared to digester 1, which can be observed with the peak of gypsum.

Miliken geospray mortar is a blend of quartz and alkalis and has high calcium content with a very little alumina (Al_2O_3). Figure 133(d), represents different phases formed in it after hydration, and dissociation and consumption of these phases when exposed to this aggressive environment throughout the depth. As discussed above, due to carbonation and sulphate attack the exposed surface up to 2.5 mm depth showed a major peak of gypsum and some ettringite. Initially gypsum was also present in the reference specimen but in a very small amount. The major phase observed include Quartz (Q), poorly crystalline calcium silicate hydrate (C-S-H), calcium hydroxide also known as portlandite (P), katoite (K) and a small peak of Dolomite (D), Anorthite (Feldspar) (An) and Potassium silicate hydrate (KSH). A very high peak of gypsum, on the exposed surface and the loss of Portlandite confirmed that in the presence of high sulphate environment all the portlandite is consumed and reacted with sulphate to form gypsum. This gypsum was the reason for the delayed ettringite formation which leads to the cracking within the microstructure of mortar. A similar trend was also observed in XRD pattern of MM from digester 3 as shown below.

The sulphate resisting cement has a very limited amount of alumina to avoid the formation of ettringite as a result of exposure to the sulphate environment. The main phase observed in this Ordinary Portland Sulphate resistant cement includes Calcium Silicate hydrate (C-S-H), $Ca(OH)_2$ portlandite (P), Quartz (Q) and some gypsum (G). However, when exposed to aggressive sewage environment the main constituents were consumed and Portlandite was depleted as a result of its reaction with sulphate to produce gypsum, as shown in Figure 133(e). In addition, due to carbonation some calcite (C) was also observed but only up to 5 mm depth. In addition, some ettringite (E) and calcium sulphite hydrate ($C\bar{S}H$) can also be observed but in limited amount. In addition some traces of Anorthite (An) feldspar is also observed at all depths.

Optical images

An optical microscope, located in Material Science at UNSW, was used to obtain images to observe the deteriorated surface on the exposed region for all mix designs. Figure 134(a)-(e) represents these images after the exposure of six months. It appears that gypsum was observed in SR and MM specimens on the exposed region. Another noticeable change is the change in colour of the sand. Prior to exposure, the sand appears was either yellowish or grey in all the specimens having sand except CAC. However, the yellowish coloured sand particles diminished in number on the exposed region of MM and SR, which suggest that sand may have reacted with the exposed sewage environment. In addition a crack is also observed in MM very near to the exposed surface, confirming the disintegration of the microstructure – not observed in the other mixed designs. To study the microstructural changes taking place in depth, SEM was used to the resolution as low as 5.0 µm.

Scanning electron microscopy (SEM) & energy-dispersive X-ray (EDX)

Scanning electron microscopy was carried out to observe the microstructure of the mortar specimens. For this purpose, concrete specimens were carbon-coated to make them conductive and to perform EDX analysis. The analysis was carried out at 10 kV using a Hitachi S3400, also located at the UNSW Mark Wainwright Analytical Centre.

The microstructures of the five different mortars were examined in terms of any morphological changes, cracks observed and any mineralogical formations as a result of exposure to aggressive sewage environment. Figure 135, represents the cross sectional SEM images and EDS spectrum after six months exposure for FA-GPM. The only difference that was observed during the investigation is changes near the exposed surface of the mortar. The EDS analyses represent the elemental concentration at different locations as observed in Figure 135(d). Points 2, 4 and 5 showed some presence of sulphur confirming the penetration at the exterior exposed region.

Figure 136, represents the SEM and EDX of Slag based GPM after six months of exposure. The performance of Slag-GPM in terms of microstructure deterioration was equally good as observed in FA-GPM with dense microstructure of N-(C)-A-S-H as binding gel to be confirmed from NMR and FTIR analysis; however, some cracks were observed near the exposed region. In addition, very minor amount of sulphur can be seen in EDX which confirms that the penetration of sulphur is limited.

Figure 137, shows the microstructure of CAC after 6 months of exposure. It is observed that due to the exposure of CAC to sulphur environment some cracks were formed as a result of nucleation of gypsum and ettringite as confirmed from the XRD. However, in spite of micro cracks, overall the microstructure looks dense beside these nucleation sites. So after observing the EDX, it shows that points 4, 5 and 9 is gypsum having high calcium and sulphur content whereas the rest is aluminium based minerals like katoite, gibbsite etc.

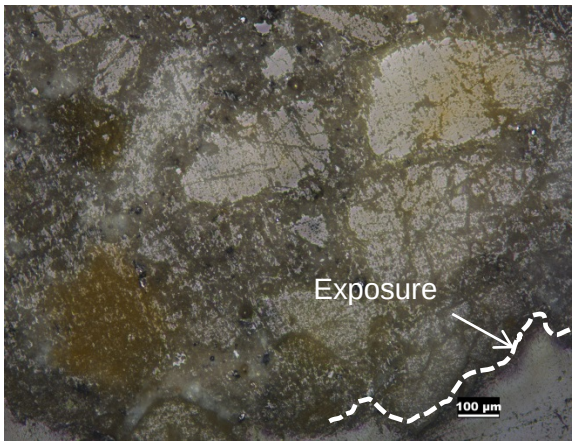

(a) FA-GPM.

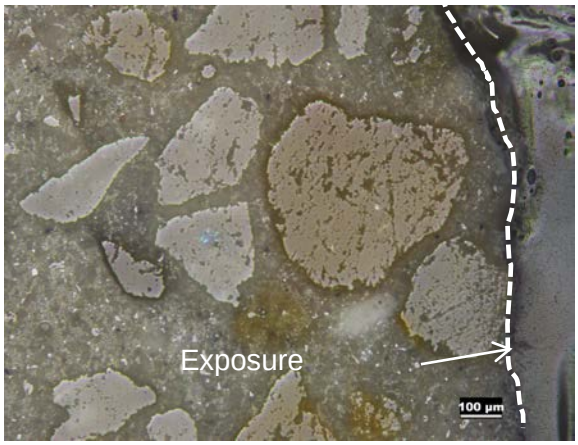

(b) Slag-GPM.

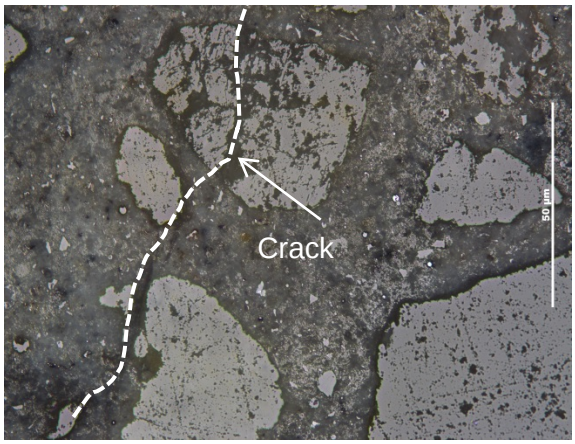

(c) MM.

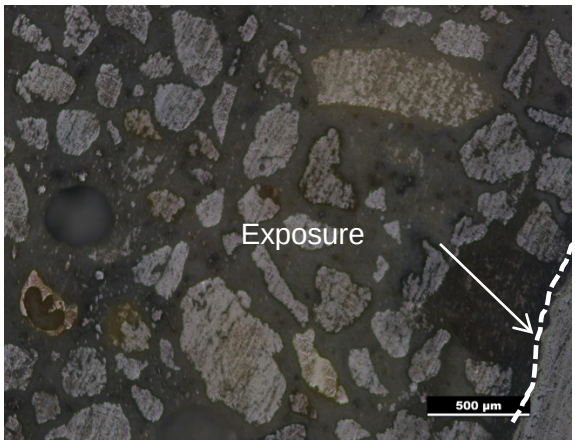

(d) SR Mortar.

(e) CAC.

Figure 134. Optical Images: (a) FA-GPM; (b) Slag-GPM; (c) MM; (d) SR; and (e) CAC after 6 months of exposure.

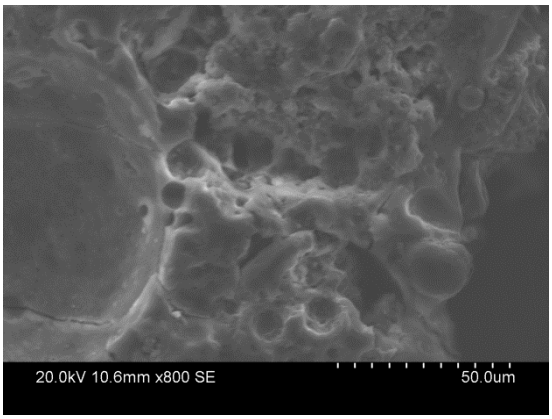

(a) Dense Microstructure

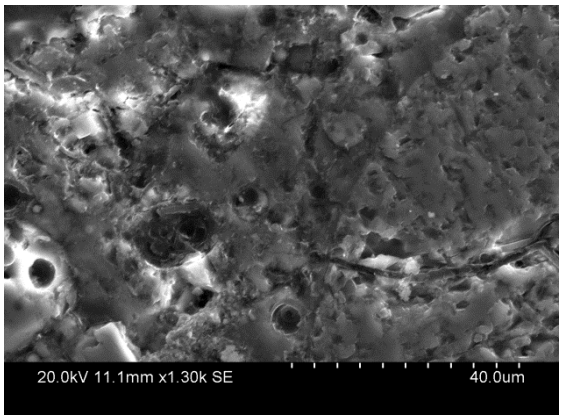

(b) Minor porosity near exposed region

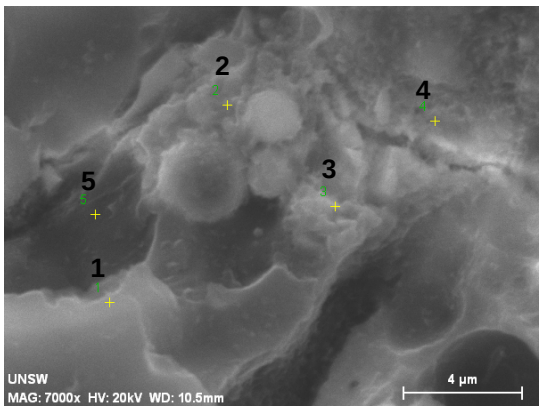

(c) Alumino-Silicate matrix observed using EDX Point Scan

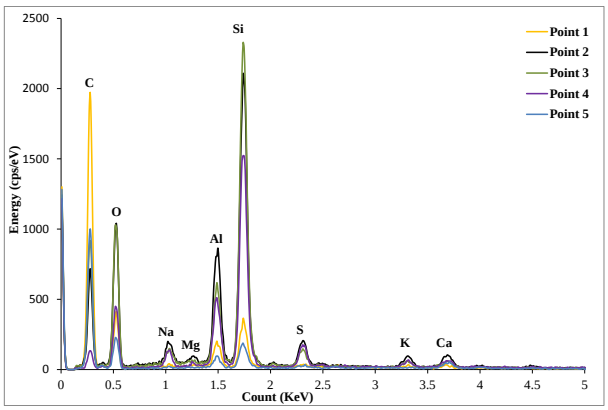

(d) EDX Point Scan of microstructure

Figure 135. SEM and EDX of FA-GPM after 6 months of exposure.

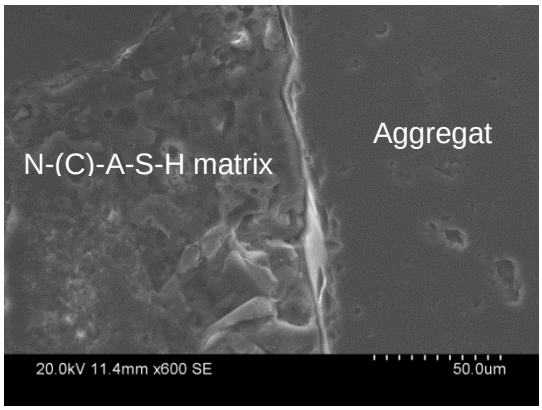

(a) Dense Microstructure at interface with aggregate

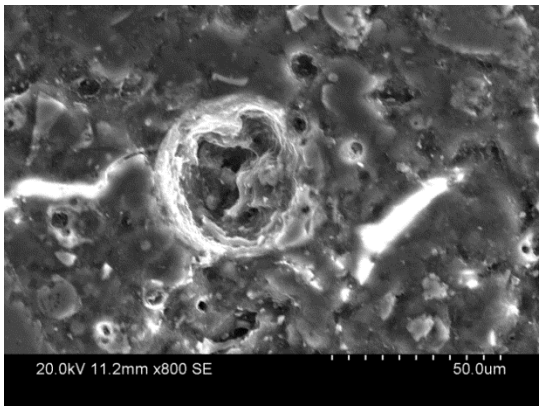

(b) Minor cracks with pores near exposure

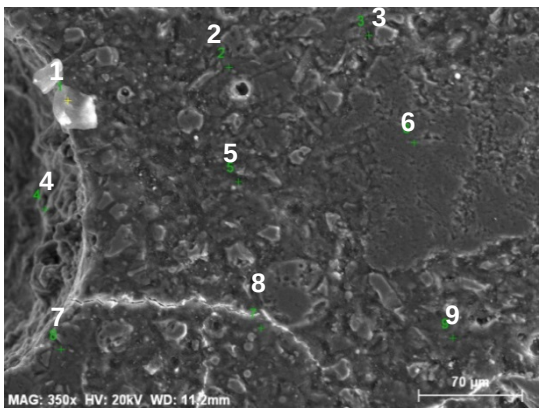

(c) Matrix observed using EDX Scan

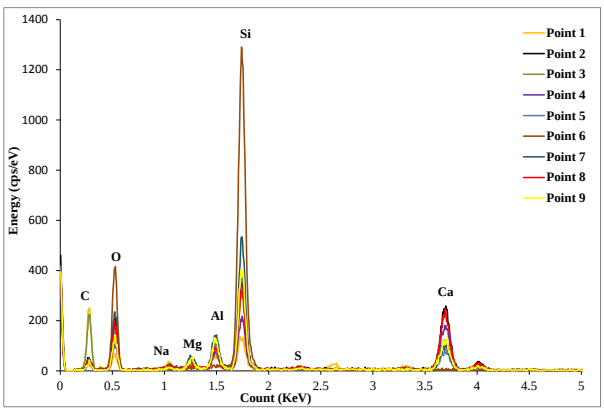

(d) EDX Point Scan of microstructure

Figure 136. SEM and EDX of Slag-GPM after 6 months of exposure.

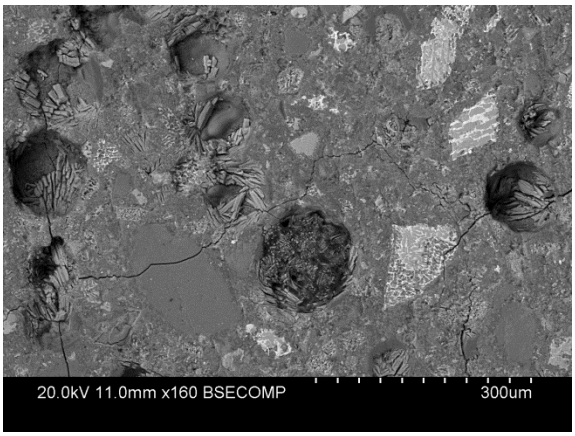

(a) Crack developed right from the exposed region to different nucleation sites.

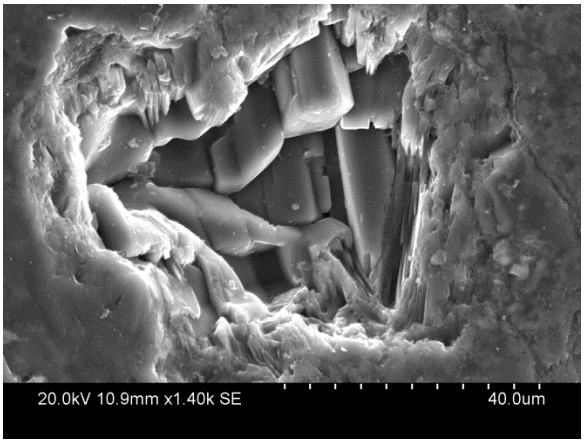

(b) Gypsum crystals observed near the crack zone.

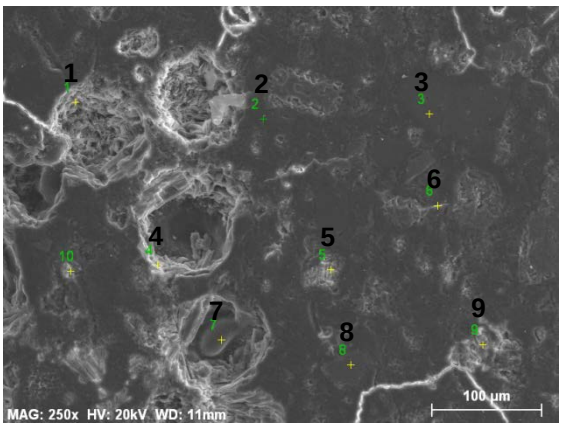

(c) Matrix observed using EDX Scan.

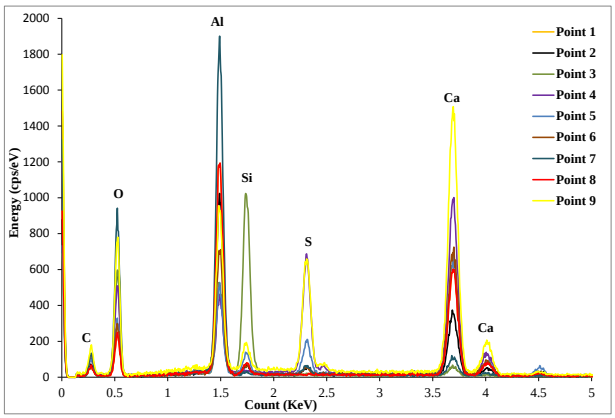

(d) EDX Point Scan of microstructure.

Figure 137 SEM and EDX of CAC after 6 months of exposure

The microstructure of the Miliken geospray mortar after the exposure of six months on aggressive wastewater environment is shown in Figure 138. Major cracks can be seen in the region just beside the exposure with some gypsum formation as shown in the Figure 138 (b). Further, EDX is also performed at different positions to investigate the elements present after exposure. High percentage of sulphur is observed especially at location 3, 5, 6 and 8 in as shown in Figure in 138 (c) and (d). These locations predict the presence of high amount of gypsum as confirmed from the XRD analysis of the exposed region up to 2.5mm, see Figure 133.

Figure 139, represents the SEM images and EDX data at different locations just beside the exposed surface. The microstructural images shows quite large cracks which are developing on the exterior interface. In addition, the microstructure shows some minor C-S-H gel deterioration at the exposed region. Further, EDX analysis was also performed to observe the elements present at different locations. Point 1 represents a silica crystal, whereas point 4, 5 and 9 represents high sulphur content. Almost all the points shows the presence of calcium, however the higher concentration can be seen on the points away from the exposed region.

An elemental mapping technique was used as well to investigate the penetration of sulphur and location of different elements present in the microstructure. Major focus was given to calcium, aluminium, silicon, and sulphur. Figure 140, represents the SEM and EDX mapping of FA-GPM after 6 months of exposure. It can be seen that penetration of sulphur is very limited only on the outer region near the silica crystal particles shown in pink. Further, very limited amount of calcium particles are observed in Figure 140(f). The Al mapping in Figure 140(e), represent the alumino-silicate matrix of Geopolymer within the silica crystals

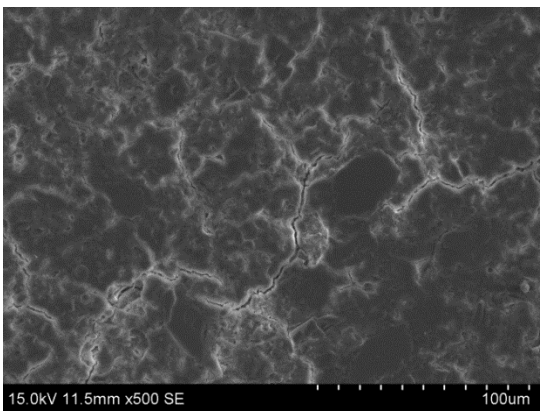

(a) Crack developed right from the exposed region.

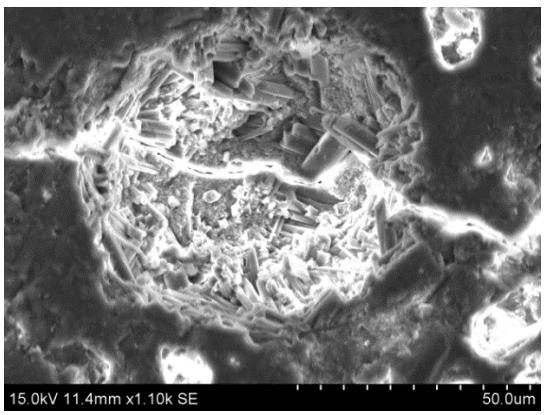

(b) Gypsum crystals observed near the crack zone.

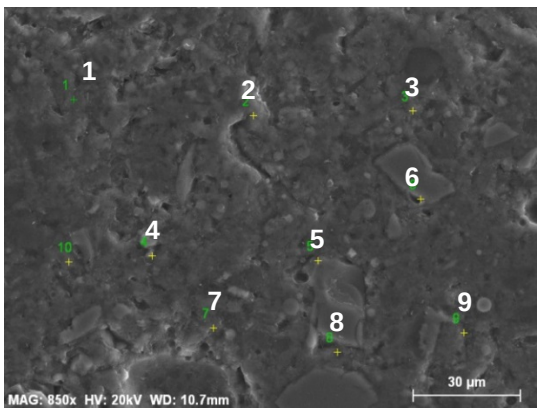

(c) Matrix observed using EDX Scan.

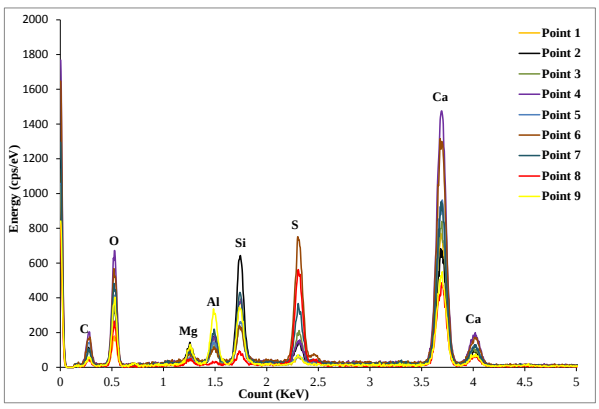

(d) EDX Point Scan of microstructure.

Figure 138. SEM and EDX of MM after 6 months of exposure.

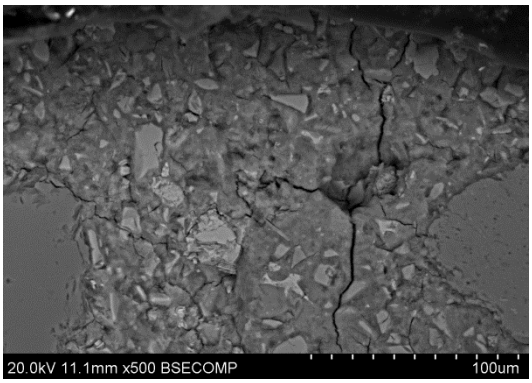

(a) Major crack developed right from the exposed region.

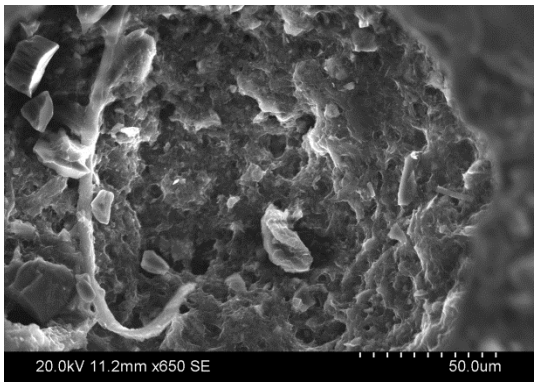

(b) Deteriorated microstructure on the exposed region.

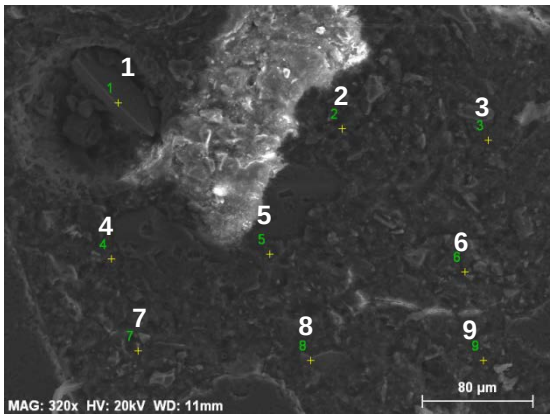

(c) Matrix observed using EDX scan.

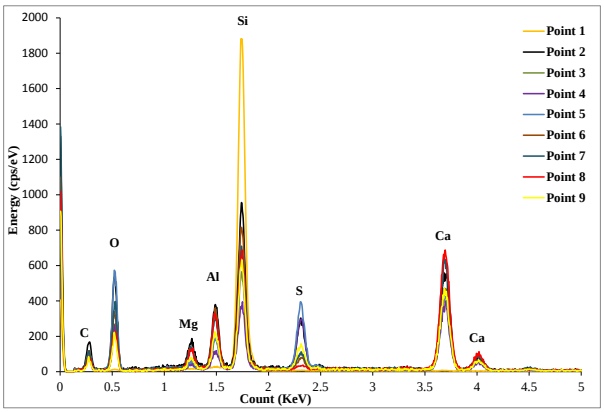

(d) EDX Point Scan of microstructure.

Figure 139 SEM and EDX of SR after 6 months of exposure

Figure 141, represents the mapping of Slag-GPM after six months exposure to aggressive sewage environment. It can be seen in the map that the penetration of sulphur is almost negligible throughout the microstructure with very distant points. This shows the low concentration of Sulphur. Further, high calcium concentration can be seen with some silica particles from sand and N-(C)-A-S-H matrix around them.

The SEM and EDX mapping of CAC is shown in Figure 142. The concentration of sulphur can be seen as in red colour with higher penetration at the location of crack. This confirms that as a result of sulphur penetration some gypsum is formed which results in the degradation of microstructure near the exposed region. Further, very limited silicon concentration is observed throughout the matrix. Higher concentration of Calcium and aluminium can be seen in Figure 142(e) and (f) near exposed surface.

Figure 143, represents the SEM and EDX map of Miliken mortar after six months of exposure at aggressive waste water treatment plant. It can be seen that the penetration of sulphur is very high as compared to other mortar specimens like CAC, FA and Slag-GPM in Figure 143(d). In addition, higher calcium content can be seen in the matrix confirming the C-S-H, CH, gypsum and calcite presence which were observed in XRD. Some silica particles were also observed in the microstructure. Further, some concentration of aluminium can also be seen representing the presence of katoite (C3AH6) within the matrix.

The EDX elemental mapping and SEM images of SR mortar after 6 months of exposure at aggressive waste water treatment plant can be seen in Figure 144(a) to (f). The high concentration of sulphur can be observed on the right hand side of the exposed surface. Further, by considering Figure 144(f), XRD and SEM images of SR mortar this region between the silica particles are covered with C-S-H gel, gypsum and calcium sulphite hydrate ($C\bar{S}H$). In addition, higher concentration of alumina is observed in the matrix relates to ettringite formation and the presence of anorthite ($CaAl_2Si_2O_8$) as observed in XRD.

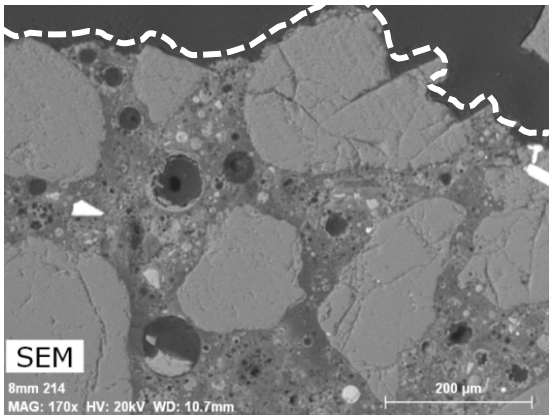

(a) SEM Image after exposure for mapping.

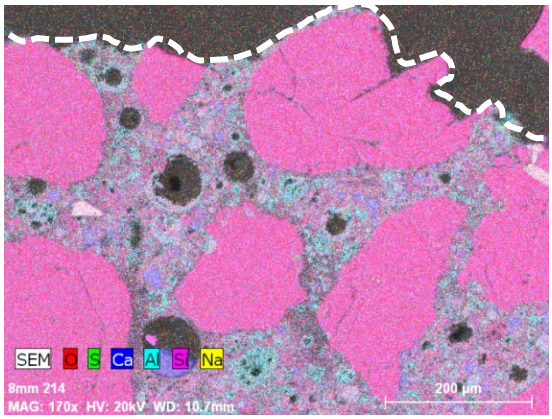

(b) Map of different elements observed.

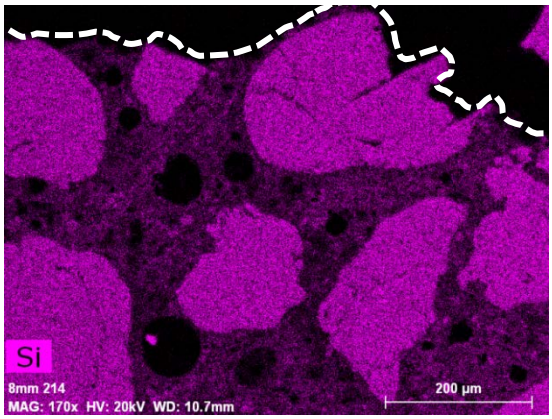

(c) Silicon map.

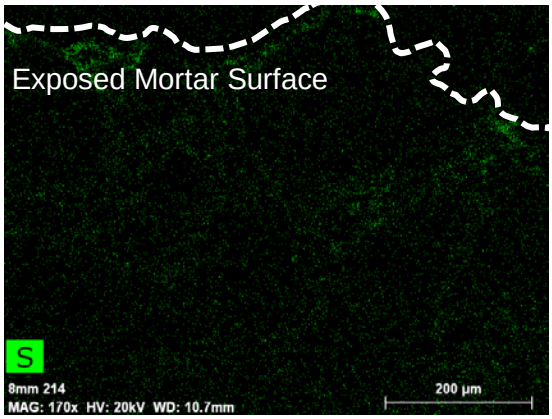

(d) Sulphur map.

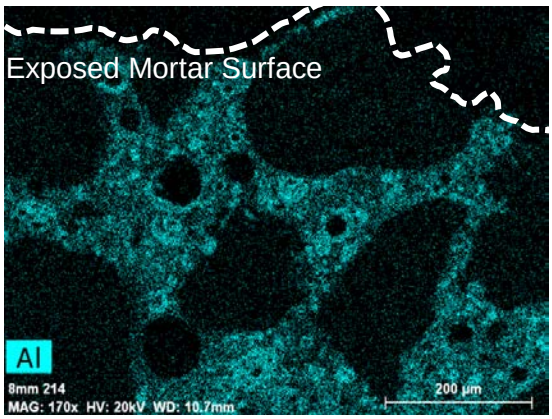

(e) Aluminium map.

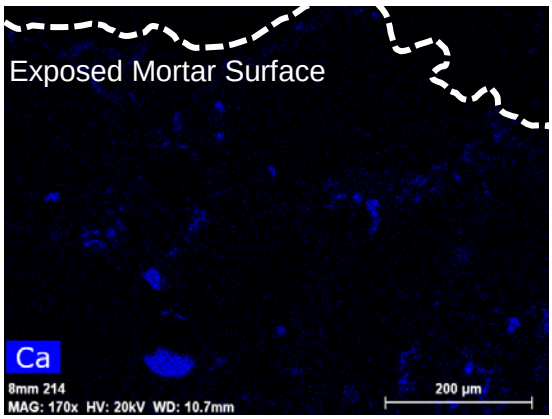

(f) Calcium map.

Figure 140. SEM and EDX mapping of FA-GPM after 6 months of exposure.

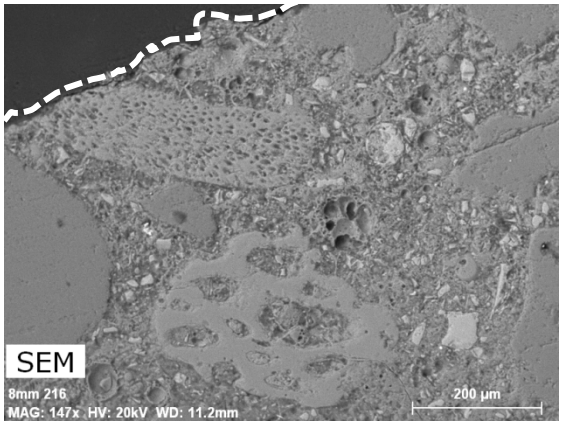

(a) SEM Image after exposure for mapping.

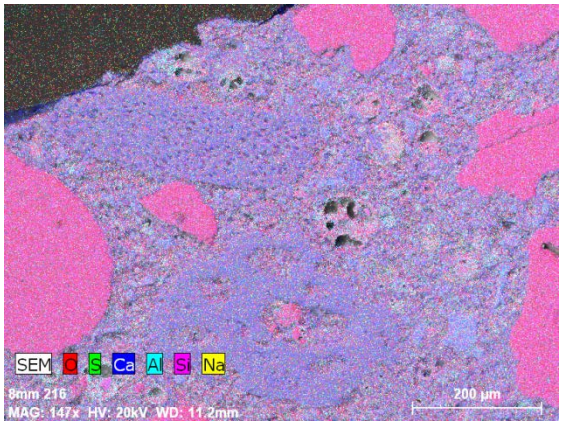

(b) Map of different elements observed.

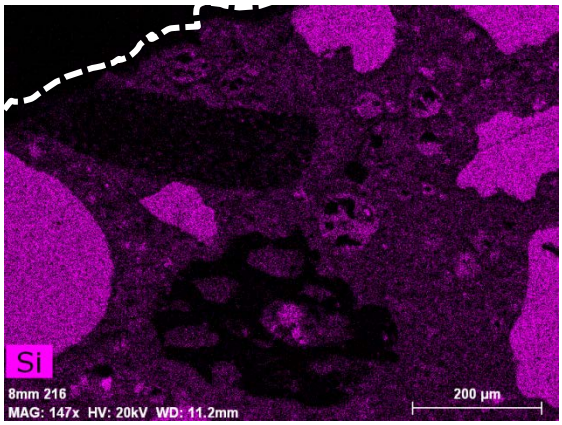

(c) Silicon map.

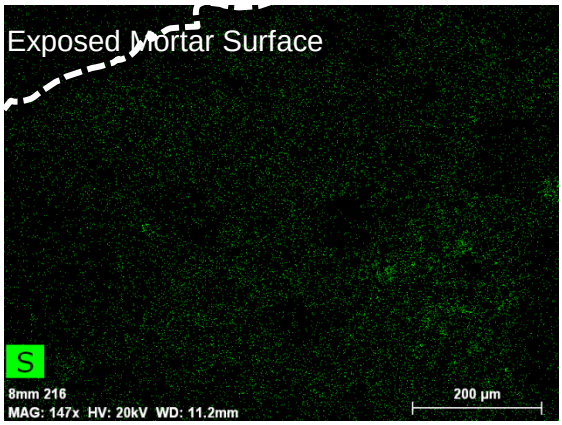

(d) Sulphur map.

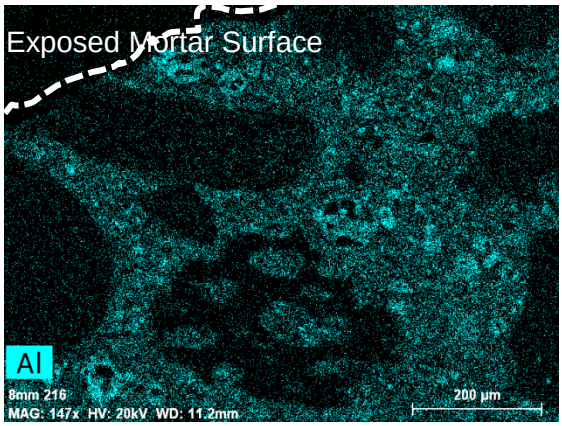

(e) Aluminium map.

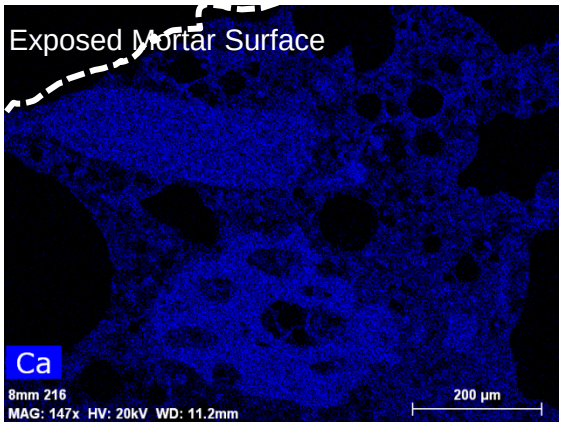

(f) Calcium map.

Figure 141. SEM and EDX mapping of Slag-GPM after 6 months of exposure.

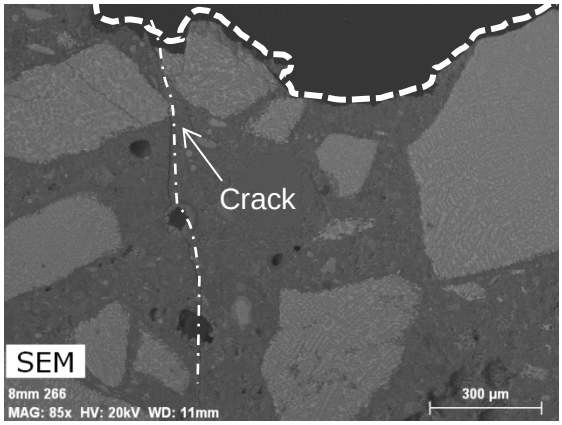

(a) SEM Image after exposure for mapping.

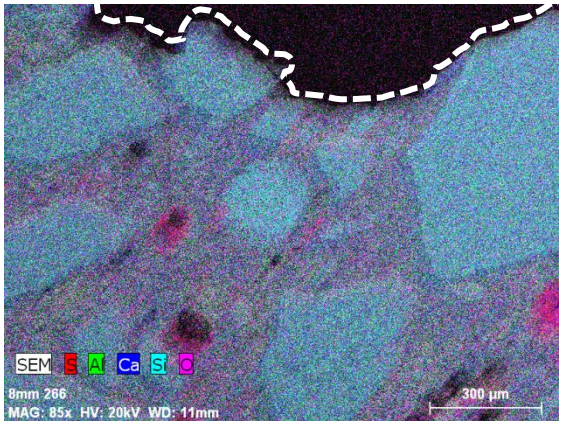

(b) Map of different elements observed.

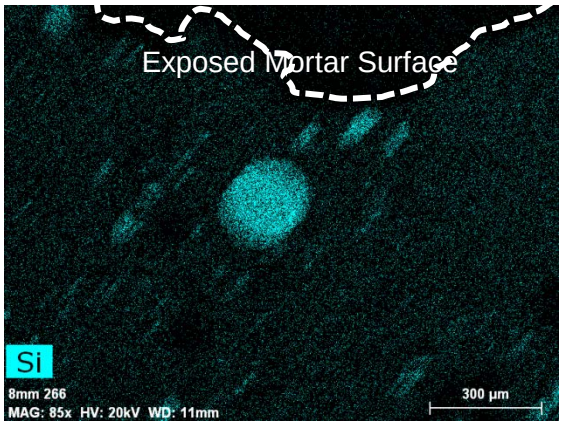

(c) Silicon map.

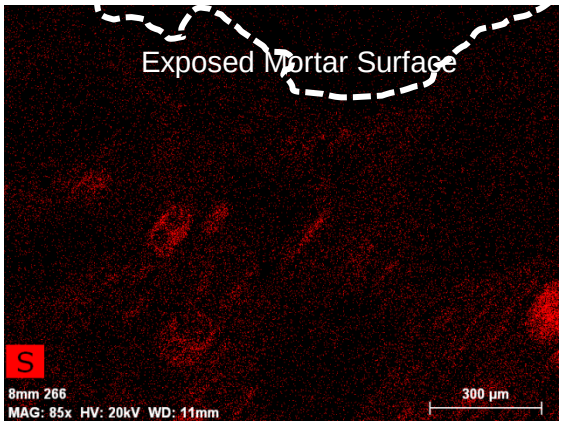

(d) Sulphur map.

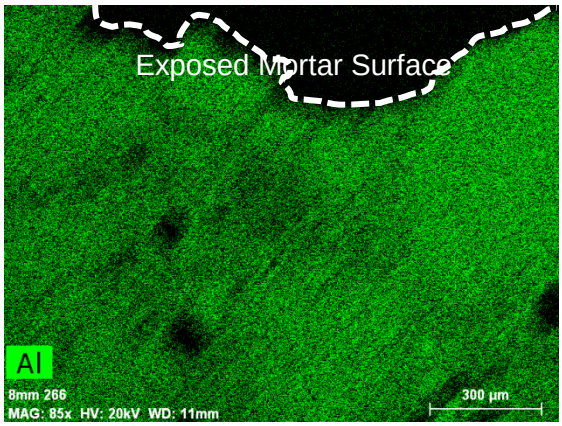

(e) Aluminium map.

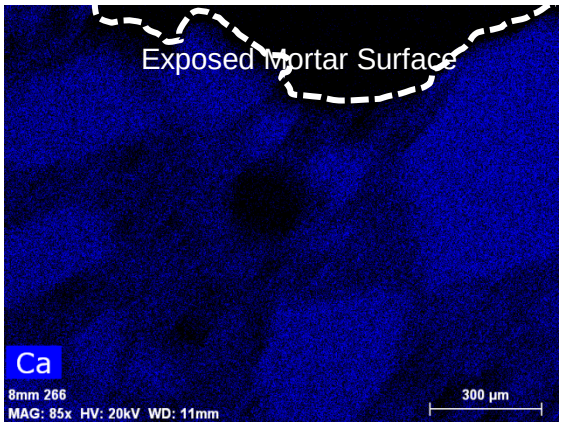

(f) Calcium map.

Figure 142. SEM and EDX mapping of CAC after 6 months of exposure.

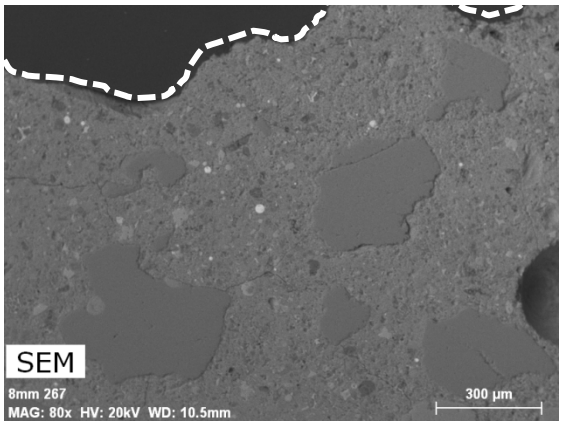

(a) SEM Image after exposure for mapping.

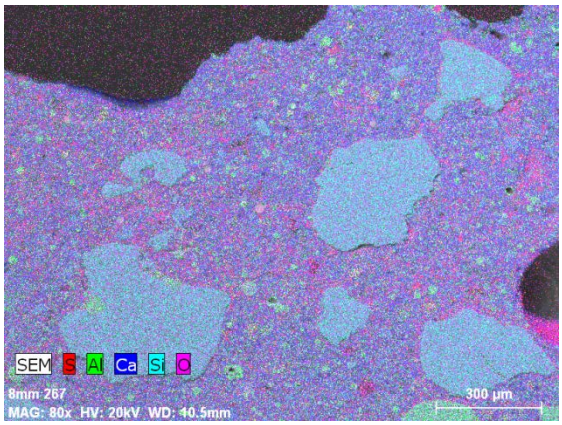

(b) Map of different elements observed.

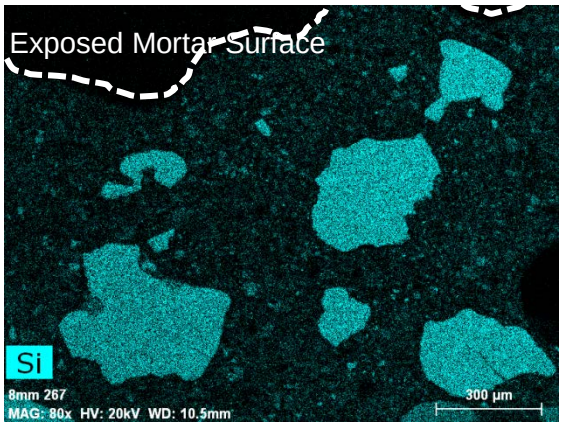

(c) Silicon map.

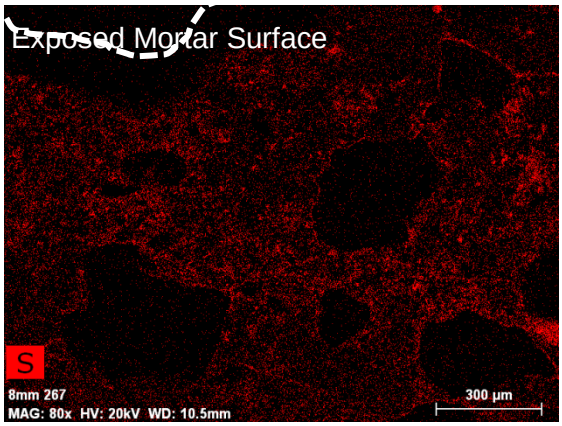

(d) Sulphur map.

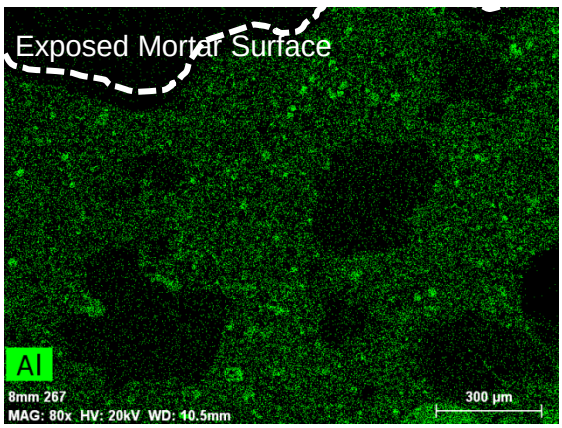

(e) Aluminium map.

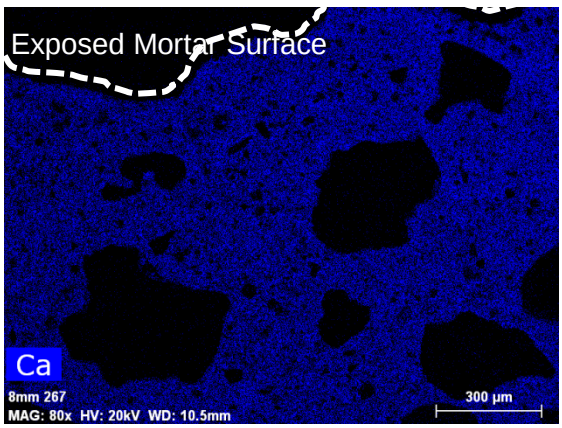

(f) Calcium map.

Figure 143. SEM and EDX mapping of MM after 6 months of exposure.

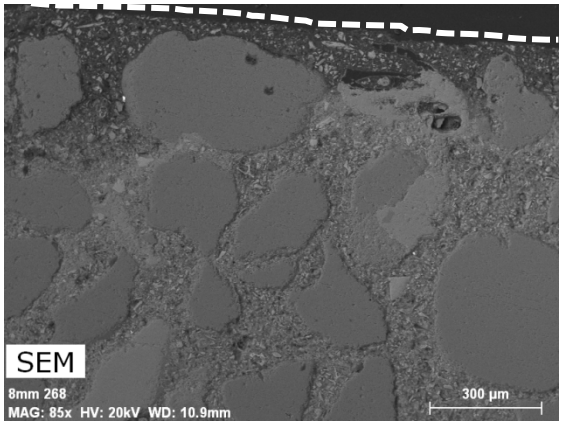

(a) SEM Image after exposure for mapping.

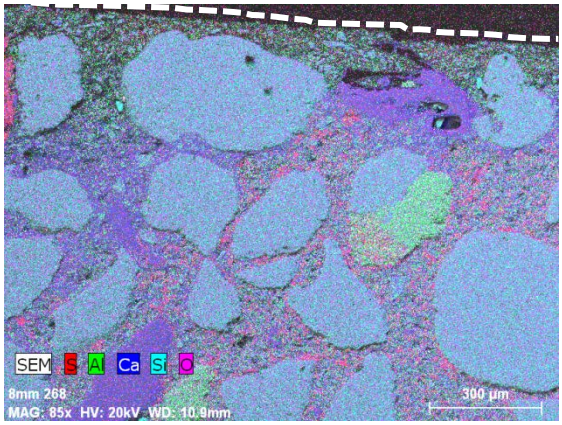

(b) Map of different elements observed.

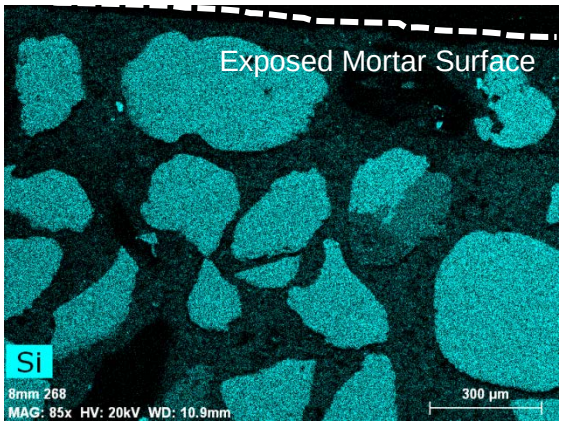

(c) Silicon map.

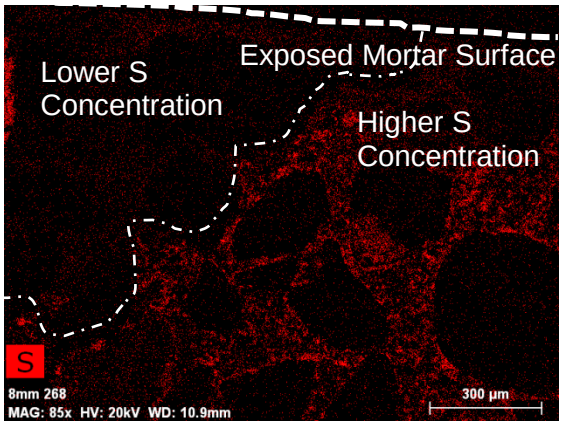

(d) Sulphur map.

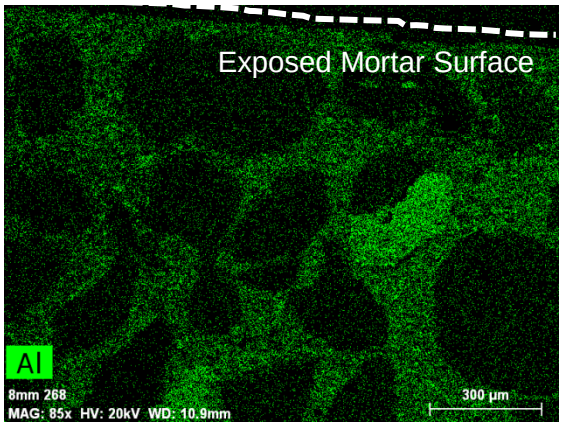

(e) Aluminium map.

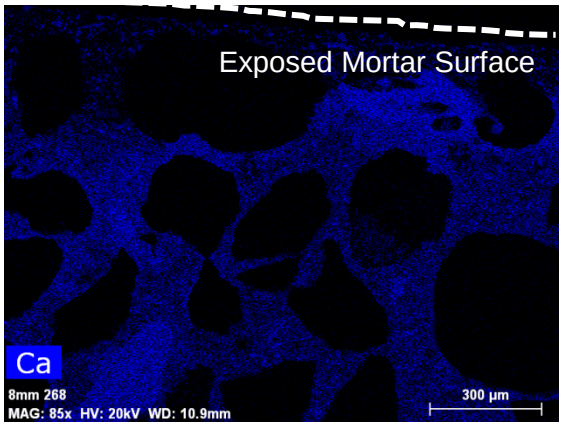

(f) Calcium map.

Figure 144 SEM and EDX mapping of SR Mortar after 6 months of exposure

Conclusions

Test results reported here are limited to six months of exposure. Results already attained highlight some fundamental differences in the degradation processes involved depending on the type of binder considered. For instance, the neutralisation depth and the sulphate ions penetration is much more severe in the fly ash based Geopolymer than in the GGBFS Geopolymer which is in agreement with the results from Lake King site in Western Australia. But, longer term results are required in order to draw reliable conclusions. The long term ageing monitoring of the numerous specimens remaining in the digesters is in progress.

Moreover after a longer period of exposure, to further analyse the microstructure and Geopolymer binder, flourier transform infrared spectroscopy (FTIR) and nuclear magnetic resonance spectroscopy (NMR) techniques in addition to SEM/EDX and XRD will be performed at different penetration depths of paste specimens. These techniques will be helpful in observing the structural degradation of Geopolymer matrix at molecular level. Further, to observe the amount of different structural analogies of alumina-silicate matrix i.e. monomer, dimers, trimers, di(sialate-siloxo) poly(sialate-siloxo), described by Qn(mAl), where m represents the number of Al atoms surrounding and n represents the Si centres, 29Si and 27Al MAS-NMR spectroscopy will be performed. This technique will provide a better understanding of the molecular framework of Geopolymer matrix after the reference exposed period.

Summary and Conclusions

Field testing results of Geopolymer concrete structures are reported. Field trails have been undertaken to determine the behaviour of Geopolymer in different service environments at different levels of severity:

- Campbellfield site, Perth site, Toowoomba tanks site and Wellcamp Business Park Bridge are located away from any severe chemical exposure. AS3600 exposure classification is 3(a) Surfaces of members in above-ground exterior environments in areas that are Inland (>50 km from coastline) and non-industrial.
- Portland Site, Westport Boat Ramp Project at Port Macquarie NSW and Rocky Point boat ramp QLD are all structures in marine environment exposed to chloride contamination and risk of steel reinforcement corrosion. AS3600 exposure classification is 5(b and c) – in spray zone and tidal/splash zone.
- Lake King site is a severe environment combining chloride, acid and sulphate attacks. AS3600 exposure classification is U.
- North Head Wastewater Treatment Plant at Manly, NSW is an example of a very severe environment. At this site Geopolymer mortar coupons are exposed to biogenic corrosion. AS3600 exposure classification is U.

Field experimentation carried out on Wellcamp Business Park bridge aimed at assess the serviceability of a Geopolymer concrete bridge deck top-slab under normal service conditions in the exposure classification mentioned above. The response of the bridge to mechanical loading as well as daily and seasonal temperature variations was investigated. Overall, the Geopolymer concrete slab performs as expected under the daily and seasonal temperature variations and without any significant change in the structural integrity. The response of the bridge to truck loading in terms of deflection was correctly predicted by the finite element modelling and in agreement with Australian Standards dictated serviceability requirements.

Concrete carbonation was the main potential deterioration for the Campbellfield site, Perth, and the Toowoomba water tanks site located in AS3600 3(a) exposure classification. Overall results are showing that the performance of Geopolymer concrete is variable and depends significantly on the mix design parameters. The Campbellfield results showed that two Geopolymer concretes with very similar precursors (70-75% fly ash/25-30% GGBFS) but with slightly different activator compositions could perform quite differently; one performing well and the other poorly.

The Toowoomba water tanks site results showed that carbonation front penetration in high GGBFS based Geopolymer was significantly faster than in the reference OPC concrete. Therefore, prescriptive approach based on compressive strength and mix design parameters appears not to be appropriate to control the risk of carbonation induced steel reinforcement corrosion in Geopolymer concrete. A performance based approach is recommended instead.

Regarding marine exposure, results obtained at Portland site were in total contradiction with results obtained at Rocky Point. For both Portland and Rocky Point, GGBFS based Geopolymer concrete were used. The performance of the Geopolymer concrete at Portland site was poor with a chloride diffusion coefficient much higher than that of a reference OPC concrete. In contrast, the performance of the Geopolymer EFC concrete at Rocky Point boat ramp was outstanding with a low chloride diffusion coefficient. At Lake King site, fly ash based Geopolymer was used. In this case the resistance to chloride penetration was low. As mentioned, for carbonation, performance of Geopolymer concrete in a chloride environment is variable depending on the mix design parameters, even using the same type of precursor materials, activators and admixtures.

Both the Lake King and the North Head Wastewater Treatment Plant investigations showed that fly ash based Geopolymer concrete does not perform well against aggressive species such as chloride or sulphate penetration. GGBFS based Geopolymer concrete seems to perform better but longer term investigation, particularly at the North Head Wastewater Treatment Plant and the Westport boat ramp is required to draw reliable conclusions. Monitoring is on-going at these sites.

Importantly, Toowoomba tanks site showed that geopolymers after cracking experience efficient self-healing similarly to OPC concrete. Self-healing capability of concrete is an important aspect of structural durability.

Overall, this field testing campaign carried out as part of RP1020 project, and funded by the CRC-LCL, confirms the necessity of developing performance based specifications for Geopolymer concretes. For all exposure classifications, suitable testing methods are required to assess the performance of concrete in order to assist engineers to specify Geopolymer concrete conservatively and in confidence. The Handbook being developed as part of the RP1020 project aims to address the durability issue highlighted in this report, as well as mechanics needed for design.

References

[1] J. Davidovits. Global warming impact on the cement and aggregate industries. World Resource Review. 1994; 6 (2): 263-278.

[2] J. Davidovits. Geopolymers and geopolymeric materials. Journal of Thermal Analysis. 1989; 35: 429-441.

[3] M. Olivia and H. Nikraz. Properties of fly ash Geopolymer concrete designed by Taguchi method. Materials and Design. 2012; 36: 191-198.

[4] A. Castel, R. François and G. Arliguie. Effect of loading on carbonation penetration in reinforced concrete elements. Cement and Concrete Research. 1999; 29: 561-565.

[5] D.W.S. Ho and R.K. Lewis. Carbonation of concrete and its prediction. Cement and Concrete Research. 1987; 17: 489-504.

[6] S.A. Bernal, J.L. Provis, B. Walkley, R.S. Nicolas, J.D. Gehman, D.G. Brice, A.R. Kilcullen, P. Duxson and J.S.J.v. Deventer. Gel nanostructure in alkali-activated binders based on slag and fly ash, and effects of accelerated carbonation. Cement and Concrete Research. 2013; 53: 127-144.

[7] S.A. Bernal, R.S. Nicolas, J.L. Provis, R.M.a.d. Gutie´rrez and J.S.J.v. Deventer. Natural carbonation of aged alkali-activated slag concretes. Materials and Structures. 2014; 47: 693-707.

[8] A.A. Adam. Strength and durability properties of alkali activated slag and fly ash-based Geopolymer concrete. 2009; RMIT University, Melbourne, Australia.

[9] M.S. Badar, K. Kupwade-Patil, S.A. Bernal, J.L. Provis and E.N. Allouche. Corrosion of steel bars induced by accelerated carbonation in low and high calcium fly ash Geopolymer concretes. Construction and Building Materials. 2014; 61: 79-89.

[10] D.W. Law, A.A. Adam, T.K. Molyneaux, I. Patnaikuni and A. Wardhono. Long term durability properties of class F fly ash Geopolymer concrete. Materials and Structures. 2014; 48: 721-731.

[11] M.S.H. Khan, A. Castel and A. Noushini. Carbonation of a low-calcium fly ash Geopolymer concrete. Magazine of Concrete Research. 2016; 69 (1): 24-34.

[12] D. Jeon, Y. Jun, Y. Jeong and J.E. Oh. Microstructural and strength improvements through the use of Na2CO3 in a cementless Ca(OH)2 -activated Class F fly ash system. Cement and Concrete Research. 2015; 67: 215-225.

[13] H. El-Didamony, A.A. Amer and H.A. Ela-ziz. Properties and durability of alkali-activated slag pastes immersed in sea water. Ceramics International. 2012; 38: 3773-3780.

[14] M.W. Hussin, M.A.R. Bhutta, M. Azreen, P.J. Ramadhansyah and J. Mirza. Performance of blended ash Geopolymer concrete at elevated temperatures. Materials and Structures. 2015; 48 (3): 709-720.

[15] A.M. Rashad and S.R. Zeedan. The effect of activator concentration on the residual strength of alkali-activated fly ash pastes subjected to thermal load. Construction and Building Materials. 2011; 25: 3098-3107.

[16] E.U. Haq, S.K. Padmanabhan and A. Licciulli. Synthesis and characteristics of fly ash and bottom ash based geopolymers–A comparative study. Ceramics International. 2014; 40: 2965-2971.

[17] K. Wang, S.P. Shah and A. Mishulovich. Effects of curing temperature and NaOH addition on hydration and strength development of clinker-free CKD-fly ash binders. Cement and Concrete Research. 2004; 34: 299-309.

[18] M. Heikal, M.Y. Nassar, G. El-Sayed and S.M. Ibrahim. Physico-chemical, mechanical, microstructure and durability characteristics of alkali activated Egyptian slag. Construction and Building Materials. 2014; 69: 60-72.
[19] L. Alarcon-Ruiz, G. Platret, E. Massieu and A. Ehrlacher. The use of thermal analysis in assessing the effect of temperature on a cement paste. Cement and Concrete Research. 2005; 35: 609-613.
[20] I. Ismail, S.A. Bernal, J.L. Provis, R.S. Nicolas, S. Hamdan and J.S.v. Deventer. Modification of phase evolution in alkali-activated blast furnace slag by the incorporation of fly ash. Cement & Concrete Composites. 2014; 45: 125-135.
[21] J. Dong, L. Wang and T. Zhang. Study on the strength development, hydration process and carbonation process of NaOH-activated Pisha Sandstone. Construction and Building Materials. 2014; 66: 154-162.
[22] M.-H. ZHANG and H. Li. Pore structure and chloride permeability of concrete containing nano-particles for pavement. Construction and Building Materials. 2011; 25 (2): 608-616.
[23] D.S. Cheema. Low calcium fly ash based Geopolymer concrete: Long term durability properties. 2014; Curtin University, Perth, Australia.
[24] E. Menéndez, T. Matschei and F.P. Glasser. Sulfate attack of concrete, in Performance of cement-based materials in aggressive aqueous environments. 2013; Springer. 7-74.
[25] W.G. Hime, R.A. Martinek, L.A. Backus and S.L. Marusin. Salt hydration distress. Concrete International. 2001; 23 (10): 43-50.
[26] L. Bertolini, B. Elsener, P. Pedeferri, E. Redaelli and R.B. Polder. Corrosion of steel in concrete: Prevention, diagnosis, repair. 2013; John Wiley & Sons.
[27] K. Pasupathy, M. Berndt, J. Sanjayan, P. Rajeev and D.S. Cheema. Durability performance of precast fly ash based Geopolymer concrete under atmospheric exposure conditions. Submitted to Materials and Structures.
[28] V.F. Barbosa, K.J. MacKenzie and C. Thaumaturgo. Synthesis and characterisation of materials based on inorganic polymers of alumina and silica: sodium polysialate polymers. International Journal of Inorganic Materials 2000; 2 (4): 309-317.
[29] S.A. Bernal, J.L. Provis, D.G. Brice, A. Kilcullen, P. Duxson and J.S.J.v. Deventer. Accelerated carbonation testing of alkali-activated binders significantly underestimates service life: The role of pore solution chemistry. Cement and Concrete Research. 2012; 42: 1317-1326.
[30] A.M. Neville. Concrete: Neville's insights and issues. 2006; Thomas Telford.
[31] G. Villain, M. Thiery and G. Platret. Measurement methods of carbonation profiles in concrete: Thermogravimetry, chemical analysis and gammadensimetry. Cement and Concrete Research. 2007; 37 (8): 1182-1192.
[32] S. Barnett, D. Macphee, E. Lachowski and N. Crammond. XRD, EDX and IR analysis of solid solutions between thaumasite and ettringite. Cement and Concrete Research. 2002; 32 (5): 719-730.
[33] I. Ismail, S.A. Bernal, J.L. Provis, R.S. Nicolas, D.G. Brice, A.R. Kilcullen, S. Hamdan and J.S.v. Deventer. Influence of fly ash on the water and chloride permeability of alkali-activated slag mortars and concretes. Construction and Building Materials. 2013; 48: 1187-1201.
[34] J.S.J.v. Deventer, J.L. Provis, P. Duxson and D.G. Brice. Chemical research and climate change as drivers in the commercial adoption of alkali activated materials. Waste and Biomass Valorization. 2010; 1 (1): 145-155.
[35] M. Collepardi, A. Marcialis and R. Turrizian. Penetration of chloride ions into cement pastes and concretes Journal of American Ceramic Society - Discussion and Notes. 1992; 55 (10): 534-535.

[36] H.-W. Song, C.-H. Lee and K.Y. Ann. Factors influencing chloride transport in concrete structures exposed to marine environments. Cement & Concrete Composites. 2008; 30 (2): 113-121.
[37] R.J. Detwiler, K.O. Kjellsen and O.E. Gjorv. Resistance to chloride intrusion of concrete cured at different temperatures. ACI Materials Journal. 1991; 88 (1): 19-24.
[38] K. Kupwade-Patil and E.N. Allouche. Examination of chloride-induced corrosion in reinforced Geopolymer concretes. Journal of Materials in Civil Engineering. 2013; 25 (10): 1465-1476.
[39] F.U. Shaikh. Effects of alkali solutions on corrosion durability of Geopolymer concrete. Advances in Concrete Construction. 2014; 2 (2): 109-123.
[40] A. Neville. Chloride attack of reinforced concrete: An overview. Materials and Structures. 1995; 28 (2): 63-70.
[41] M. Olivia and H. Nikraz. Durability of fly ash Geopolymer concrete in a seawater environment. in Concrete. 2011; 25th Biennial Conference of Concrete Institute of Australia.
[42] C. Monticelli, M.E. Natali, A. Balbo, C. Chiavari, F. Zanotto, S. Manzi and M.C. Bignozzi. A study on the corrosion of reinforcing bars in alkali-activated fly ash mortars under wet and dry exposures to chloride solutions. Cement and Concrete Research. 2016; 87: 53-63.
[43] K. Kupwade-Patil and E.N. Allouche. Examination of chloride-induced corrosion in reinforced Geopolymer concretes. Journal of Materials in Civil Engineering 2013; 25 (10): 1465-1476.
[44] P. Sulapha, S.F. Wong, T.H. Wee and S. Swaddiwudhipong. Carbonation of concrete containing mineral admixtures. Journal of Materials in Civil Engineering. 2003; 15 (2): 134-143.
[45] P. Castro, M.A. Sanjuán and J. Genescá. Carbonation of concretes in the Mexican Gulf. Building and Environment. 2000; 35 (2): 145-149.
[46] J. Khunthongkeaw, S. Tangtermsirikul and T. Leelawat. A study on carbonation depth prediction for fly ash concrete. Construction and Building Materials. 2006; 20: 744-753.
[47] Y. Lo and H.M. Lee. Curing e!ects on carbonation of concrete using a phenolphthalein indicator and Fourier-transform infrared spectroscopy. Building and Environment. 2002; 37: 507-514.
[48] C-F. Chang and J.-W. Chen. The experimental investigation of concrete carbonation depth. Cement and Concrete Research. 2006; 36: 1760-1767.
[49] M. Criado, A. Palomo and A. Ferna´ndez-Jime´nez. Alkali activation of fly ashes. Part 1: Effect of curing conditions on the carbonation of the reaction products. Fuel. 2005; 84: 2048-2054.
[50] J. Davidovits. Geopolymer, green chemistry and sustainable development solutions: Proceedings of the World Congress Geopolymer. 2005; Geopolymer Institute.
[51] M. Babaee and A. Castel. Chloride-induced corrosion of reinforcement in low-calcium fly ash-based Geopolymer concrete. Cement and Concrete Research. 2016; 88: 96-107.
[52] Vicroads, Test Methods for the Assessment of Durability of Concrete. Technical Note. 2007; 89: 4.
[53] W.P.S. Dias. Reduction of concrete sorptivity with age through carbonation. Cement and Concrete Research. 2000; 30 (8): 1255-1261.
[54] I. Ismail, S.A. Bernal, J.L. Provis, R. San Nicolas, D.G. Brice, A.R. Kilcullen, S. Hamdan and J.S.J. van Deventer. Influence of fly ash on the water and chloride permeability of alkali-activated slag mortars and concretes. Construction and Building Materials. 2013; 48 (0): 1187-1201.

[55] C. Jiang, K. Fan, F. Wu and D. Chen. Experimental study on the mechanical properties and microstructure of chopped basalt fibre reinforced concrete. Materials and Design. 2014; 58: 187-193.
[56] K. Pasupathy, M. Berndt, A. Castel, J. Sanjayan and R. Pathmanathan. Carbonation of a blended slag-fly ash Geopolymer concrete in field conditions after 8 years. Construction and Building Materials. 2016; 125: 661-669.
[57] A. Costa and J. Appleton. Concrete carbonation and chloride penetration in a marine environment. Concrete Science and Engineering. 2001; 3 (12): 242-249.
[58] T. Bakharev, J.G. Sanjayan and Y.-B. Cheng. Resistance of alkali-activated slag concrete to carbonation. Cement and Concrete Research. 2001; 31: 1277-1283.
[59] J. Lizarazo-Marriaga and P. Claisse. Determination of the concrete chloride diffusion coefficient based on an electrochemical test and an optimization model. Materials Chemistry and Physics. 2009; 117: 536-543.
[60] W. Chalee and C. Jaturapitakkul. Effects of W/B ratios and fly ash finenesses on chloride diffusion coefficient of concrete in marine environment. Materials and structures. 2009; 42 (4): 505-514.
[61] S.A. Bernal, J.L. Provis, A. Fernández-Jiménez, P.V. Krivenko, E. Kavalerova, M. Palacios and C. Shi. Binder chemistry–high-calcium alkali-activated materials, in Alkali Activated Materials. 2014; Springer. 59-91.
[62] I. Ismail, S.A. Bernal, J.L. Provis, R. San Nicolas, D.G. Brice, A.R. Kilcullen, S. Hamdan and J.S.J. van Deventer. Influence of fly ash on the water and chloride permeability of alkali-activated slag mortars and concretes. Construction and Building Materials. 2013; 48: 1187-1201.
[63] T. Cheewaket, C. Jaturapitakkul and W. Chalee. Long term performance of chloride binding capacity in fly ash concrete in a marine environment. Construction and Building Materials. 2010; 24 (8): 1352-1357.
[64] H. Hirao, K. Yamada, H. Takahashi and H. Zibara. Chloride binding of cement estimated by binding isotherms of hydrates. Journal of Advanced Concrete Technology. 2010; 3 (1): 77-84.
[65] T. Cheewaket, C. Jaturapitakkul and W. Chalee. Long term performance of chloride binding capacity in fly ash concrete in a marine environment. Construction and Building Materials. 2010; 24: 1352-1357.
[66] R. Demirbog and R. Gul. The effects of expanded perlite aggregate, silica fume and fly ash on the thermal conductivity of lightweight concrete. Cement and Concrete Research. 2003; 33: 723-727.
[67] K.-H. Kim, S.-E. Jeon, J.-K. Kim and S. Yang. An experimental study on thermal conductivity of concrete. Cement and Concrete Research. 2003; 33: 363-371.
[68] P. Duxson, G.C. Lukey and J.S.J.v. Deventer. Thermal conductivity of metakaolin geopolymers used as a first approximation for determining gel interconnectivity. Industrial & Engineering Chemistry Research. 2006; 45 (23): 7781-7788.
[69] A.V. Riessen. Thermo-mechanical and microstructural characterisation of sodium-poly(sialate-siloxo) (Na-PSS) geopolymers. Journal of Material Science. 2007; 42: 3117-3123.
[70] H. Uysal, R. Demirbog˘a, R. Sahin and R.s. Gu¨l. The effects of different cement dosages, slumps, and pumice aggregate ratios on the thermal conductivity and density of concrete. Cement and Concrete Research. 2004; 34: 845-848.
[71] K.G. Wakili, E. Hugi, L. Karvonen, P. Schnewlin and F. Winnefeld. Thermal behaviour of autoclaved aerated concrete exposed to fire. Cement & Concrete Composites. 2015; 62: 52-58.

[72] Y. XU and D. CHUNG. Cement of high specific heat and high thermal conductivity, obtained by using silane and silica fume as admixtures. Cement and Concrete Research. 2000; 30: 1175-1178.
[73] H.T. Yu and L. Khazanovich. Effects of construction curling on concrete pavement behavior. Seventh International Conference on Concrete Pavements: The Use of Concrete in Developing Long-Lasting Pavement Solutions for the 21st Century. 2001: Orlando, Florida.
[74] L. Dahmani and M. Kouane. Thermal cracking respone of reinforced concrete beam to gradient temperature. International Journal of Civil, Environmental, Structural, Construction and Architectural Engineering. 2012; 6: 1014-1018.
[75] H.S. Jensen. Hydrogen sulfide induced concrete corrosion of sewer networks. 2009; Aalborg University, Denmark.
[76] E. Vincke, E.V. Wanseele, J. Monteny, A. Beeldens, N.D. Belie, L. Taerwe, D.V. Gemert and W. Verstraete. Inuence of polymer addition on biogenic sulfuric acid attack of concrete. International Biodeterioration & Biodegradation. 2002; 49 283 – 292.
[77] A. Noushini, M. Babaee and A. Castel. Suitability of heat-cured low-calcium fly ash-based Geopolymer concrete for precast applications. Magazine of Concrete Research. 2015; 68 (4): 163-177.
[78] C. Grengg, F. Mittermayr, A. Baldermann, M.E. Böttcher, A. Leis, G. Koraimann, P. Grunert and M. Dietzel. Microbiologically induced concrete corrosion: A case study from a combined sewer network. Cement and Concrete Research. 2015; 77: 16-25.
[79] M.P. Lavigne, A. Bertron, C. Botanch, L. Auer, G. Hernandez-Raquet, A. Cockx, J.-N. Foussard, G. Escadeillas and E. Paul. Innovative approach to simulating the biodeterioration of industrial cementitious products in sewer environment. Part II: Validation on CAC and BFSC linings. Cement and Concrete Research. 2016; 79: 409-418.
[80] J. Herisson, M. Gue´guen-Minerbe, E.D.v. Hullebusch and T. Chaussadent. Influence of the binder on the behaviour of mortars exposed to H2S in sewer networks: a long-term durability study. Materials and Structures 2017; 50 (8): 1-18.
[81] M.W. House and W.J. Weiss. Review of microbially induced corrosion and comments on needs related to testing procedures. 4th International Conference on the Durability of Concrete Structures. 24–26 July 2014; Purdue University, IN, USA.
[82] X.J. Songa, M. Marosszekya, M. Brungsb and R. Munn. Durability of fly ash based Geopolymer concrete against sulphuric acid attack. 10DBMC International Conference On Durability of Building Materials and Components. 17-20 April 2005; Lyon, France.
[83] F. Rendell and R. Jauberthie. The deterioration of mortar in sulphate environments. Construction and Building Materials. 1999; 13 (6): 321–327.
[84] R.L. Islander, J.S. Devinny, A. Member, F. Mansfeld, A. Postyn and H. Shih. Microbial ecology of crown corrosion in sewers. Journal of Environmental Engineering. 1991; 117 (6): 751-770.
[85] S.A. Bernal, R.M.d. Gutiérrez and J.L. Provis. Engineering and durability properties of concretes based on alkali-activated granulated blast furnace slag/metakaolin blends. Construction and Building Materials. 2012; 33: 99-108.